May 2021

An Observational Investigation of Mid-Latitude Thermospheric Temperatures and High-Latitude E-Region Neutral Wind Structures

Rafael Luiz Araujo de Mesquita
Clemson University, rafaelluizmesquita@gmail.com

An observational investigation of mid-latitude thermospheric temperatures and high-latitude E-region neutral wind structures

---

A Dissertation
Presented to
the Graduate School of
Clemson University

In Partial Fulfillment
of the Requirements for the Degree
Doctor of Philosophy
Physics and Astronomy

---

by
Rafael Luiz Araújo de Mesquita
May 2021

Accepted by:
Dr. Stephen Kaeppler, Committee Chair
Dr. Miguel Larsen
Dr. Jens Oberheide
Dr. Chad Sosolik

Abstract

The Earth's atmosphere is a complicated environment. Different physical processes affect it depending on the altitude and latitude, among other factors. Three different aspects of the Earth's upper atmosphere are investigated here, using two different techniques. These investigations are: the mid-latitude midnight temperature maximum (MTM), the mesosphere and low-thermosphere Kelvin-Helmholtz instability (KHI), and the advective acceleration in the E-region. All of these studies occur in the Earth's thermosphere and expand our understanding of these phenomena that represent different ways in which energy is transferred throughout the Earth's atmosphere. Observing and characterizing these energy transfer pathways is crucial to further our knowledge of these geophysical processes.

The MTM is typically understood as an equatorial phenomenon that has a characteristic temperature increase around midnight due to the constructive interference between tidal components. While this phenomenon has been studied thoroughly in latitudes $< \pm 20°$ and modeled to reach $\sim 60°$; previous observations of temperature and winds had not confirmed its occurrence in latitudes $> 20°$ N. In Mesquita et al. (2018) and Chapter 2 the following scientific question is addressed: What are the characteristics of the mid-latitude MTM? To answer it, a technique was developed to observe the phenomenon and estimate its amplitude between 32° N and 42° N. This investigation used the North American Thermosphere Ionosphere Observing Network (NATION) containing 5 Fabry-Perot interferometers (FPI). Its data set includes a total of 846 nights of observations over a period of approximately 5 years. The new approach for calculating the MTM amplitude was developed by using a series of fits to determine the tidal background. Removing this background from the temperatures and applying an inversion algorithm allowed for the construction of two-dimensional temperature and wind maps, which illustrated the effects of the MTM on the wind field. A statistical analysis of the feature proved that both MTM peaks oscillate with semi-annual and annual periods.

The KHI has been observed and characterized in the mesosphere (statically unstable region). However, the few observations of this phenomena in the low thermosphere (statically stable region) were not detailed and did not show evidence of turbulence above the mesopause. The following scientific questions were still unanswered: What is the triggering mechanism of KHIs in statically stable regions and how does it evolve? These questions are addressed by Mesquita et al. (2020) and in Chapter 3. The triangulation of vapor traces from sounding rockets showed the KHI in great detail above 100 km. Characterizing the KHI development in three dimensions revealed wavelength, eddy diameter, and vertical length scale of 9.8, 5.2, and 3.8 km, respectively, centered at 102 km altitude. Further analysis of dimensionless numbers – such as Richardson, Reynolds, and Froude numbers – illustrated that the presence of strong and sustained shears was the mechanism involved in generating KHIs in the thermosphere.

Advection has been modeled to be an important acceleration in high-latitude. However, observations of this forcing mechanism have been scarce. Moreover, previous studies investigated the effects of the Hall drag on the Coriolis parameter without including the centrifugal force in the analysis. Chapter 4 addresses the following scientific question: How does geomagnetic activity affect the vertical distribution of forces (including advection) and the modified Coriolis parameter in the E-region? Triangulation of vapor traces released from sounding rockets was used to calculate the meridional advective acceleration. The observations took place during 5 different geomagnetic conditions for the JOULE II, HEX II, MIST, Auroral Jets, and Super Soaker launches. The instantaneous Lorentz acceleration, which is often considered a dominant force in high-latitude active conditions, was calculated by using the Poker Flat Incoherent Scatter Radar (PFISR) data. These calculations showed that advection can become a dominant term depending on the geomagnetic activity level. The analysis of modified Coriolis parameter Φ, which includes the centrifugal acceleration, revealed that in strong geomagnetic activity an air parcel tends to remain in the auroral oval (channel of enhanced Lorentz acceleration) for an extended period of time. This potentially provides an explanation for why winds are enhanced in the low thermosphere above 115 km during strong geomagnetic activity.

Dedication

I dedicate this work to my supportive family and all of my teachers.

To Frankie O. Felder, former Graduate School Dean, who introduced me to the true spirit of the Clemson Family.

Acknowledgments

First and foremost I would like to thank my advisors: Dr. John Meriwether, Dr. Miguel Larsen, and Dr. Stephen Kaeppler. I would also like to express sincere thanks to my committee members: Dr. Jens Oberheide and Dr. Chad Sosolik.

Undeniably, I would not have started this project without the incredible teachers I met throughout my education. Thank you to Tia Celia and Tia Cleide, my first and forever teachers. I would also like to thank my undergraduate professors Dr. Ricardo Buriti, Dr. Fabio Dahia, and the late Dr. Jürgen W. Precker, who all guided me towards an unrelenting passion for Physics.

My genuine thanks to the outstanding Physics and Astronomy department staff for your support during my most difficult times. Barrett Barker, Celesté Hackett, Debra Helvie, Jonathan Simpson, Lamar Durham, Lori Rholetter, Michael Denz, and Patti Larsen were all there for me when I needed them the most. My deepest gratitude to Amanda Ellenburg and Dr. Sean Brittain. I could not have done it without you.

Additionally, I would like to thank my family and friends for their support throughout this process. Felipe and Higor, I hope I made you proud. Mom, thank you for keeping me alive, prioritizing my education, and for being there for me through thick and thin. My Lisossomos family, especially Bruno, Igor, Lucas, Tia Mônica, and Nícolas, all believed in me when nobody else did and I will carry the solace our friendship wherever I go. I am grateful to Gibran, Tim, Omar, Ivan, and Taylor, and to my paddling partners Jim and Jill for all the lessons and good memories.

Simply put, I would have never survived the last five years without the the unconditional love and support of the Dalhouse family, who chose to make me one of their own. I learned more from Ms. Debbie in the last few months than anyone has ever had the patience to teach me. I will be forever in debt to you. Lastly, thank you to Rebecca, my love and best teacher.

Table of Contents

List of Tables

List of Figures

Chapter 1

Introduction

1.1 Introduction

The studies included in this dissertation focus on three atmospheric phenomena that occur in the Earth's thermosphere and expand our understanding of energy transfer mechanisms. Observing and characterizing these energy transfer pathways is crucial to further our knowledge of these geophysical processes. This dissertation addresses the following scientific questions:

1. What are the characteristics of the mid-latitude midnight temperature maximum (MTM)?

2. What is the triggering mechanism of Kelvin-Helmholtz instability (KHI) in statically stable regions and how does it evolve?

3. How does geomagnetic activity affect the vertical distribution of forces (including advection) and the modified Coriolis parameter in the E-region?

Chapter 2 presents a full discussion of the mid-latitude MTM (Mesquita et al., 2018). This study observed and characterized the MTM farther north than previous studies had showed. Chapter 3 discusses KHI observations made during the Super Soaker campaign. The KHI was observed in a statically stable region of the atmosphere, which led to the conclusion that the development of the KHI was associated with a different triggering mechanism than was previously observed in different atmospheric regions (Mesquita et al., 2020). Lastly, Chapter 4 presents the first results of advective acceleration in the E-region. This forcing is examined along with instantaneous Lorentz, Coriolis, and centrifugal accelerations. The behavior of the modified Coriolis parameter, including the Hall drag and the centrifugal parameter, is studied in different geomagnetic activity levels.

1.2 The Earth's Atmosphere

The Earth's atmosphere is a stratified fluid whose layers are identified by various geophysical attributes. The neutral atmosphere is categorized by temperature profile. Figure 1.1 shows typical daytime and nighttime temperatures at the equator. As expected, mid- and high-latitude temperature profiles differ from what is shown in this figure. However, the equatorial temperature profiles depicted here represent the characteristics that identify the transitional region between neutral atmospheric layers.

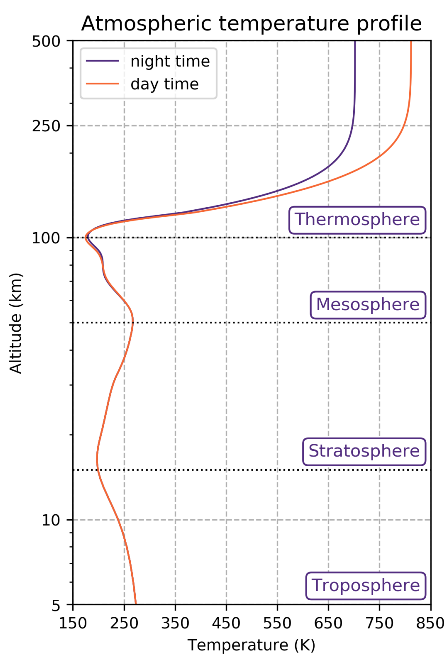

Figure 1.1: Day (orange) and night (purple) atmospheric temperature profiles (from NRLMSISE/00 by Picone et al., 2002). The dotted lines represent the transition between the respective atmospheric layers from a temperature standpoint.

Figure 1.1 shows the troposphere, stratosphere, mesosphere, and thermosphere. While atmospheric pressure and atmospheric density decrease with altitude due to gravity, the temperature profile is more intricate. The rate of increase or decrease of temperature with altitude, known as lapse rate (or $-dT/dz$, where T is the temperature and z is the altitude), is used to determine the boundaries of each layer. These boundaries, which mark the change in sign of the lapse rate, are highlighted in Figure 1.1 with dotted lines. The boundaries are the tropopause (convention for naming the transitional altitudes between layers) at 15km, stratopause at 50km, and mesopause at 100km (often interchangeable with turbopause or region where turbulent mixing is no longer dominant).

Each of the atmospheric layers has identifying characteristics due to the physical processes that take place in its altitude range. These layers were introduced by Chapman (1950). The lowest layer in the altitude range below 15 km, the troposphere, has a decreasing temperature with altitude (positive lapse rate profile) and is the layer that contains most of the atmospheric mass (approximately 90%). The second layer is the stratosphere, from 15 km to 50 km, which has a negative lapse rate. The increase in temperature in this layer is caused by UV radiation absorption by ozone (Forbes, 1995). The third layer is the mesosphere, from 50 km to 100 km. This layer has the lowest temperatures on Earth with a positive lapse rate and exhibits the airglow, a natural light caused by excitation of molecules during the day and remitted during the day and night. The components of this layer are well mixed, much like the troposphere, due to the highly unstable nature of its dynamics. The instabilities, which produce turbulence and mixing, are related to the positive lapse rate of the mesosphere and will be discussed in more detail in section 1.4. The fourth layer is the thermosphere, above 100 km, that has the highest temperatures in Earth's atmosphere.

The chemical composition of the atmospheric layers is also characterized by geophysical processes. The troposphere is dominated by N_2 and O_2, in an approximate ratio of 4:1 up to 100 km, as shown in Figure 1.2. This figure was generated using the the Naval Research Laboratory Mass Spectrometer Incoherent Scatter Radar model (NRLMSISE/00 by Picone et al., 2002) and the International Reference Ionosphere model (IRI by Bilitza, 2018). The concentration of atomic oxygen increases in the mesosphere due to solar UV radiation and dissociative recombination processes, surpassing the O_2 and N_2 at approximately 120 km and 180 km, respectively. This figure also compares the concentration of neutrals and plasma. On average, the neutral density is considerably larger than the plasma density in the atmosphere. The ratio between neutral and plasma is approximately 10^7 and 10^4 at 100 km and 200 km, respectively. These ratios are estimated with NRLMSISE/00 and IRI models change based on latitude, local time, season, and solar cycle.

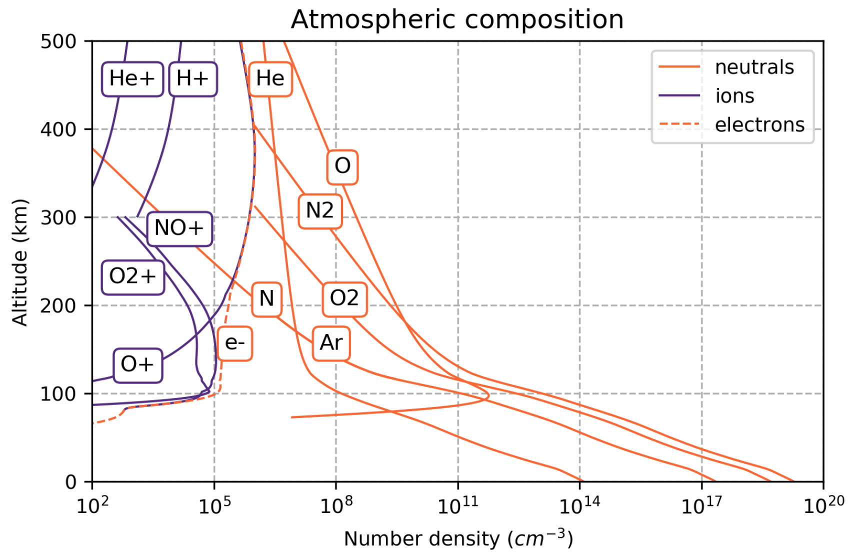

Figure 1.2: Atmospheric constitution in the equatorial region (high-latitude in the presence of aurora will change the distribution). Orange solid lines represent the neutral constituents (from NRLMSISE/00 model by Picone et al., 2002), purple solid lines represent the ionized constituents, and the orange dashed line represents electron density (both from the International Reference Ionosphere model by Bilitza, 2018).

1.2.1 Ionosphere

Incident electromagnetic radiation and high-energy particles ionize the neutral atmosphere, creating plasma above 50 km. This atmospheric layer is called the ionosphere as it contains a higher density of ionized atoms and molecules. Figure 1.2 shows results of the IRI model for the density of several ionized molecule species in daytime. The typical daytime to nighttime variation is displayed in Figure 1.3. This figure also shows the various regions of the ionosphere. The D-region (approximately 50 to 100 km altitude) is the lowest ionospheric layer. This region is highly dynamic with frequent wave breaking, atmospheric instabilities, and turbulence (Lindzen, 1981; Hecht et al., 2021). The D-region carries the lowest plasma density of the ionospheric layers. However, the plasma density increases by almost 5 orders of magnitude across its altitude range. This region fades rapidly at sunset, due to the lack of direct UV sunlight and the fast recombination of free electrons and ionized atoms and molecules. It is also the region of the lowest naturally occurring temperatures on Earth, observed between 90 and 100 km on average (Kelley, 2009).

The ionospheric E-region is located at 100 km to 150 km altitude, depending on a number of factors. The turbopause, or mesopause, approximately separates the E-region from the D-region.

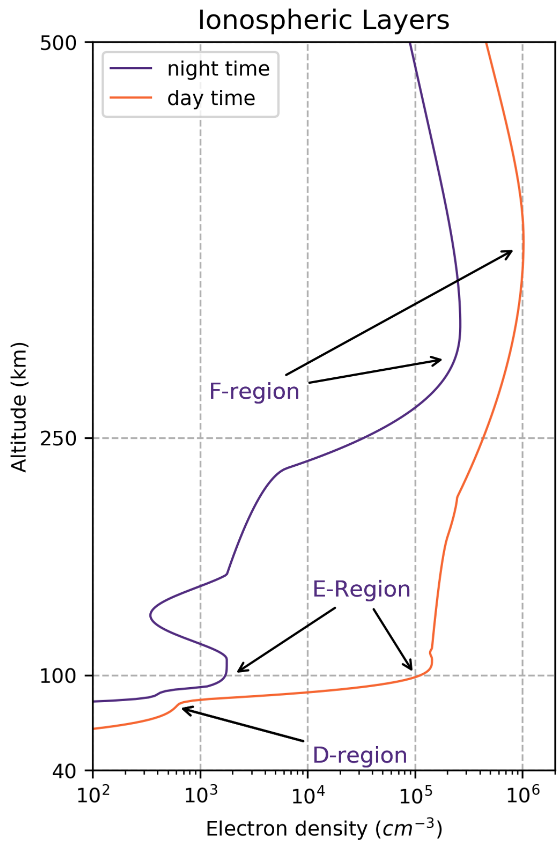

Figure 1.3: Day (orange) and night (purple) atmospheric electron density profiles (from IRI). The peak of each atmospheric layer is indicated by an arrow and the respective layer name.

The E-region was discovered during the advent of radio science, when its high electron density was found to reflect electromagnetic waves back to Earth (Appleton and Green, 1930). The electron density profile in this region is approximately $10^5 cm^{-3}$ (or $10^{11} m^{-3}$) in daytime, which is several orders of magnitude higher than the D-region, as shown in Figure 1.3. It has a complex set of forcing mechanisms, especially in the high-latitude regions where the aurora phenomenon occurs. This region is where the demagnetization of ions occurs, i.e., the ions are highly coupled with the motion of neutrals in the lower E-region and transition to an $\vec{E} \times \vec{B}$ dominated bulk ion drift with increasing altitude (Sangalli et al., 2009), where $\vec{E}$ and $\vec{B}$ are the electric and magnetic fields.

The F-region, above 150 km depending on a number of geophysical factors, has the highest plasma density in the Earth's ionosphere. Its peak electron density is typically $\sim 10^6 cm^{-3}$ (or $\sim 10^{12} m^{-3}$) in daytime as shown in the IRI model in Figure 1.3. Plasma density in the F-region remains on the same order of magnitude overnight due to the consistent input of solar electromagnetic radiation that generates plasma.

Another important aspect of the Earth's ionosphere is the occurrence of optical phenomena such as airglow and aurorae. The airglow is a global process and is generated by photoexcitation of neutral atoms or molecules. Airglow was first documented in 1869 by Ångström (1869). Photoexcitation takes place through various chemical reactions that ionize atoms and molecules (see e.g., Hays et al., 1973). Two of these processes are the 557.7 nm and 630.0 nm atomic oxygen (OI) emissions. These emissions correspond to the O(1S) $\rightarrow$ O(1D) + $h\nu_{\lambda=557.7\text{ nm}}$ and O(1D) $\rightarrow$ O + $h\nu_{\lambda=630.0\text{ nm}}$ (Hays et al., 1973). The 557.7 nm and 630.0 nm are known as the oxygen green and red lines, and peak in the low E- and F-regions, respectively. This causes the oxygen to emit the same wavelengths of light as the airglow, but with more intensity in the high-latitude sector, creating the aurorae. The first scientific description of this phenomenon was done in the late 1500's (Kázmér and Timár, 2016).

The typical behavior of the winds at ionospheric altitudes depends on the geographic location and altitude range. Figure 1.4 shows the behavior of winds in low and high latitudes from the Horizontal Wind Model (HWM/14 Drob et al., 2015) and sounding rocket profiles presented in Larsen (2002), which is updated in Chapter 4 to include wind profiles measured after 2007. The winds below 110 km are similar for both low- and high-latitude ranges. However, the winds above 120 km in high latitudes are faster on average than in low latitudes due to ionosphere coupling with the thermosphere.

1.3 The Ionospheric Neutral Momentum Equation

The motion of the neutral atmosphere is described by the neutral momentum equation (Rishbeth and Garriott, 1969; Kelley, 2009). This equation is derived from Newton's Second Law and is often referred to as the Navier-Stokes momentum equation. The neutral momentum equation 1.1, in the rotating frame of reference, that describes the key driving terms in the upper atmosphere can be written as

$$\underbrace{\frac{d\vec{U}}{dt}}_{\text{A}} + \underbrace{2\vec{\Omega} \times \vec{U}}_{\text{B}} = \underbrace{\vec{g}}_{\text{C}} \underbrace{- \frac{1}{\rho}\vec{\nabla}p}_{\text{D}} + \underbrace{\frac{\mu}{\rho}\nabla^2\vec{U}}_{\text{E}} - \underbrace{\frac{\vec{J} \times \vec{B}}{\rho}}_{\text{F}} - \underbrace{\vec{\Omega} \times \left(\vec{\Omega} \times \vec{r}\right)}_{\text{G}}, \tag{1.1}$$

where $\vec{U}$ is the vector neutral wind velocity and the terms relative to:

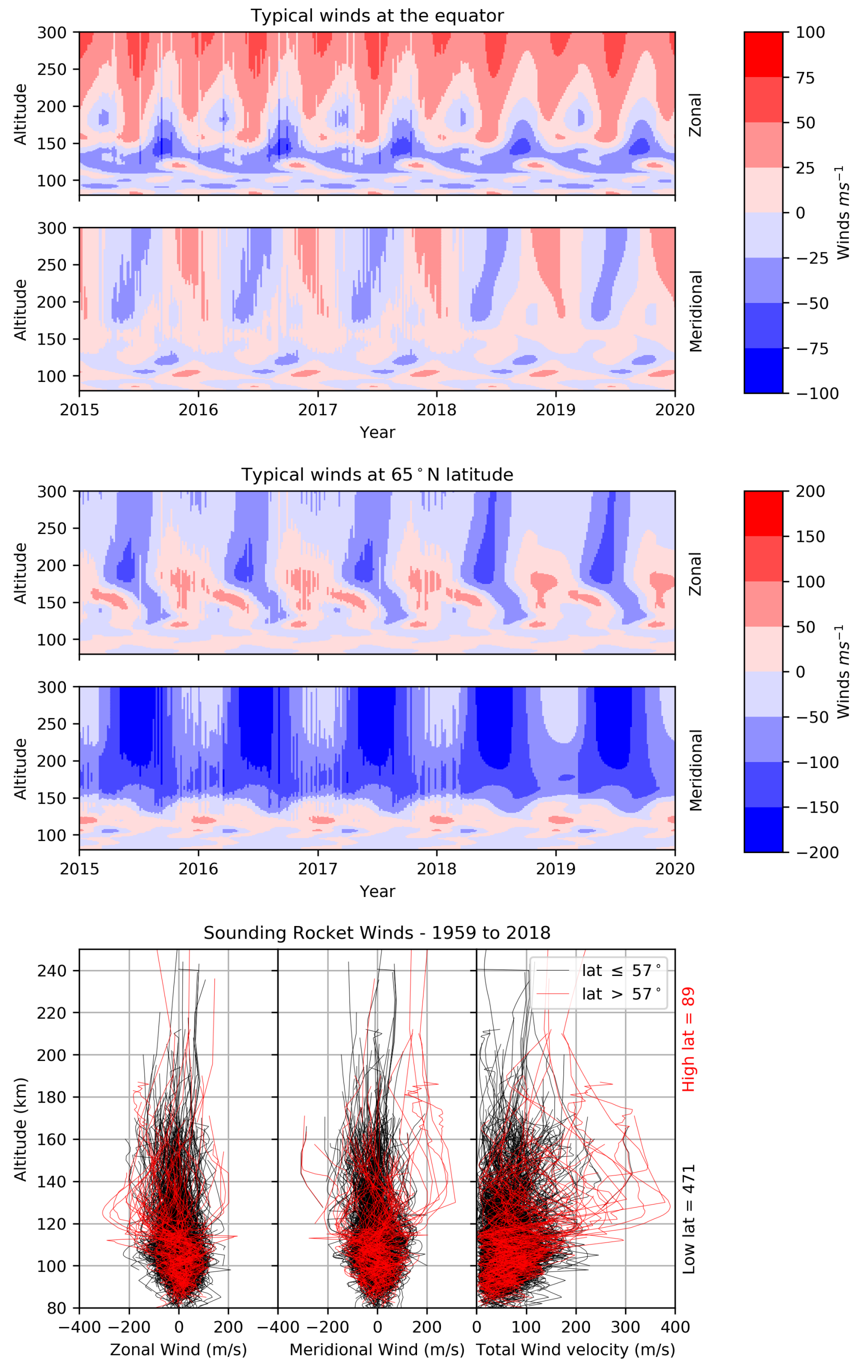

Figure 1.4: Typical behavior of the winds at equatorial (top panel) and high-latitude (middle panel) regions, and a collection of neutral wind profiles (bottom panel) (Larsen, 2002).

(A) Neutral wind acceleration

(B) Coriolis effect (where Ω is the Earth's angular velocity in the direction of its axis)

(C) Gravity

(D) Pressure gradient (where p is the pressure)

(E) Viscosity

(F) Lorentz force [1]

(G) Centrifugal force.

The neutral wind in equation 1.1 is three-dimensional and here is represented as $\vec{U} = [u\hat{x}, v\hat{y}, w\hat{z}]$, where u, v and w are the neutral wind components in the zonal, meridional, and vertical directions. The material derivative in term (A) breaks down into

$$\frac{d}{dt} = \frac{\partial}{\partial t} + \left(\vec{U} \cdot \vec{\nabla}\right), \tag{1.2}$$

where the partial time derivative corresponds to the change with time and the second term $(\vec{U} \cdot \vec{\nabla})$ corresponds to the advection. The advection term represents the transport of a certain quantity by the flow. That operator breaks down further into

$$\left(\vec{U} \cdot \vec{\nabla}\right) = u\frac{\partial}{\partial x} + v\frac{\partial}{\partial y} + w\frac{\partial}{\partial z}. \tag{1.3}$$

This operator is the advecting agent, as both the wind and its gradients play a role in the transport of a certain quantity. When applied to the winds, advection is understood as the acceleration of the airflow by the transport of wind gradients in the direction of the wind vector.

The Coriolis forcing term (B) represents the effects of Earth's rotation in equation 1.1. This term is found by considering the Earth's rotational frame of reference. This forcing term is responsible for a deflection to the right in the wind vector if viewing from above in the northern hemisphere.

The Earth's gravitational acceleration is represented by the term (C). This term is affected by the centrifugal force (G), which also results from the rotational frame of reference calculation. The small acceleration affecting $\vec{g}$ originates from $\vec{\Omega} \times (\vec{\Omega} \times \vec{r})$, where $\vec{r}$ is the Earth's radius plus the altitude of the flow (Chapter 4 of Scorer, 1997). The centrifugal force also has a meridional component in the equatorward direction.

[1] Can be rewritten as $\vec{J} = \sigma(\vec{E} + \vec{U} \times \vec{B})$, σ is the conductivity tensor and $\vec{E}$ is the electric field.

The pressure gradient term is shown in equation 1.1 term (D). This term is responsible for the motion of air masses from high- to low-pressure regions. This term is usually associated with solar heating and accelerates the winds in a direction perpendicular to isobars.

The molecular viscosity (μ in term (E) in equation 1.1) is represented in the viscosity acceleration term. This acceleration acts as a flow dampening mechanism. The molecular viscosity is a function of temperature and the density of the gas (U.S. Standard Atmosphere, 1976).

The final term (F) in equation 1.1 is the Lorentz forcing. This term is the manifestation of the collision between ions and neutrals, and can be re-written as

$$\frac{\vec{J} \times \vec{B}}{\rho} = \frac{\sigma}{\rho}(\vec{E} + \vec{U} \times \vec{B}) \times \vec{B} = \frac{\sigma}{\rho}(\vec{E} \times \vec{B}) + (\vec{U} \times \vec{B}) \times \vec{B}, \tag{1.4}$$

but with

$$(\vec{U} \times \vec{B}) \times \vec{B} = \vec{B}(\vec{U} \cdot \vec{B}) - |\vec{B}|^2\vec{U} = -|\vec{B}|^2\vec{U} \tag{1.5}$$

given that in high-latitude, the wind ($\vec{U}$) and magnetic field ($\vec{B}$) vectors are mostly perpendicular, therefore the first term is negligible ($\vec{U} \cdot \vec{B} \sim 0$). Applying $\times\vec{B}$ to the Lorentz force with constant plasma velocity $\left[q\left(\vec{E} + \vec{V} \times \vec{B}\right) = 0\right]$, where $\vec{V}$ is the plasma velocity, resulting in

$$\vec{E} \times \vec{B} = \vec{V}|\vec{B}|^2, \tag{1.6}$$

we have

$$\frac{\vec{J} \times \vec{B}}{\rho} = \frac{\sigma}{\rho}\left[\vec{V}|\vec{B}|^2 - |\vec{B}|^2\vec{U}\right] = \frac{\sigma B^2}{\rho}\left(\vec{V} - \vec{U}\right) = \nu_{ni}\left(\vec{V} - \vec{U}\right). \tag{1.7}$$

Equation 1.7 is the simplified version of the Lorentz forcing for the sake of argument. The complete version of this equation requires the use of the conductivity tensor $\overleftrightarrow{\sigma}$ written as:

$$\sigma = \begin{bmatrix} \sigma_P & -\sigma_H & 0 \\ \sigma_H & \sigma_P & 0 \\ 0 & 0 & \sigma_0 \end{bmatrix},$$

where σ_P is the Pedersen conductivity $\left(\perp\vec{B}, \parallel \vec{E}\right)$, σ_H is the Hall conductivity $\left(\perp\vec{B}, \perp\vec{E}\right)$ and σ_0

is the direct conductivity $\left(\parallel \vec{B}\right)$. The conductivity tensor, among other factors, is highly dependent on the plasma density of the media. In high-latitude, where a two-cell convection pattern develops, this term can become a dominant source of momentum on the generation of neutral winds above 115 km. This means that the neutral convection pattern is similar to the ion convection pattern, which is due to the neutral-ion collision. The neutral convection pattern has a time delay of approximately the inverse of the ion-neutral collision frequency. The term $\sigma_X B^2/\rho$ with unit $\left[s^{-1}\right]$ is often referred to as the neutral-ion collision frequency ($\sigma_P B^2/\rho = \nu_{ni}$) because it is responsible for the momentum transfer between ions and neutrals. The Hall drag $\sigma_H B^2/\rho$, also with unit $\left[s^{-1}\right]$, is responsible for a deflection to the left (opposite to the Coriolis acceleration). Its effect on the high-latitude E-region is discussed by Larsen and Walterscheid (1995), where this term disturbs the balance between Coriolis acceleration and pressure gradient, creating what the authors referred to as a modified geostrophy. The Hall conductivity is dominant until approximately 125 km while the Pedersen conductivity is dominant above that altitude. A typical profile for σ_P and σ_H can be found in the text by Kelley (2009) (Figure 2.6).

1.4 Studied Mid- and High-latitude Dynamical Phenomena

The physical processes that characterize the dynamical phenomena in the upper atmosphere depend, among other factors, on the latitude range of their occurrence. Although not exclusively, the two main forms of energy input in our atmosphere are solar radiation (light) and particle precipitation. The former strongly affects the low- and mid-latitude regions, while the latter has a strong effect in the high-latitude region. Figure 1.5 shows a diagram of the highly coupled Ionosphere-Thermosphere-Magnetosphere (ITM) system with emphasis on the phenomena studied in this dissertation (highlighted in red). These phenomena will be described in detail in the following subsections, including gaps in the community knowledge to be addressed by the studies in Chapters 2-4 of this dissertation.

While lunar gravitational forces create some tidal effects in the atmosphere, atmospheric tides are more often caused by absorption of solar radiation (water vapor in the troposphere and ozone in the stratosphere), latent heat release (tropospheric deep convective clouds), and UV radiation absorption by atomic oxygen and molecular nitrogen in the thermosphere. These tides are a global-scale oscillatory phenomenon that can be seen in the winds and temperatures in every altitude

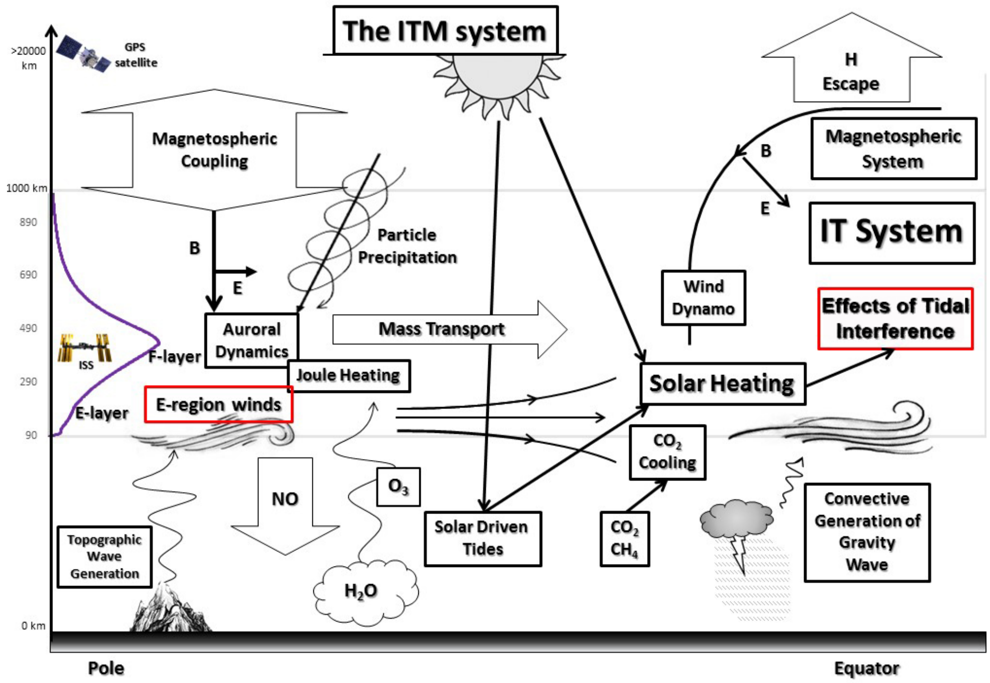

Figure 1.5: Diagram of phenomena present in the ITM system. Red boxes highlight the phenomena addressed in this dissertation.

range of the atmosphere. The period of these oscillations is 24 hours and their harmonics (e.g., 12 and 8 hours) are associated with the apparent motion of the Sun relative to the Earth's surface. These atmospheric tides are responsible for the modulation of the equatorial electrojet (Lühr et al., 2008) and generate thermospheric warming in the middle of the night (Akmaev et al., 2009).

In the high-latitude region, particle precipitation deposits a significant amount of energy that manifests as the aurora phenomenon. In that region, the dynamics of the ionospheric plasma is driven primarily by the solar wind electric field that maps down geomagnetic field lines. Geomagnetic substorms occur when the interplanetary magnetic field (IMF) turns southward, thereby allowing the particle-rich solar wind to reconnect with the Earth's magnetic field. During these substorms, the neutral winds can accelerate to hundreds of meters per second (Cai et al., 2019; Billett et al., 2020) because the plasma density is enhanced by the excitation of molecules and the plasma velocity is enhanced by the solar-wind-driven electric fields.

One important mechanism of energy transfer in the atmosphere is the presence of instabilities. Instabilities occur when the flow becomes unstable and is no longer laminar (Section 8.1 of Scorer, 1997). These instabilities play an important role in mixing between atmospheric layers, as well as redistributing energy and momentum. A fluid is said to be statically stable if its flow tends to be laminar. Atmospheric instabilities are more commonly found in statically unstable regions (troposphere and mesosphere), where the temperature profile has a negative slope (Figure 1.1).

1.4.1 MTM's Origin and Effects on the Upper Atmosphere

It is easy to assume that the atmospheric temperature rises during the day and falls during the night. However, in the thermosphere a temperature increase of ~50-200 K appears around midnight before it falls to its lowest value. This phenomenon is known as the Midnight Temperature Maximum (MTM) and was first observed in the equatorial region in the 1960s (Greenspan, 1966). Enhanced pressure and densities also occur with the MTM. The ionospheric photochemistry is affected as a result of these enhancements in temperature, density, and pressure (Colerico et al., 2006). Therefore, it is important to understand the general behavior of the MTM, and how to properly estimate its amplitude, time, and latitudinal range of occurrence.

The MTM development is caused by upward propagating and in-situ-generated tidal waves. A number of modeling studies show that the MTM is a natural consequence of tidal oscillations in the atmosphere (e.g., Mayr et al., 1979; Herrero and Spencer, 1982). Colerico and Mendillo (2002) showed in their study with the Thermosphere-Ionosphere-Electrodynamical General Circulation Model (TIEGCM) that the MTM depends on diurnal, semidiurnal, and terdiurnal, as well as higher order, tidal oscillations. Akmaev et al. (2009) used the Whole Atmosphere Model (WAM) to present the first simulation that internally reproduced the MTM. They discussed the wake-like behavior of the MTM, where the feature appears at the equator around 21 local time (LT) and travels toward the poles within the latitudinal range of $\pm 60°$ degrees. The authors also predicted the presence of a secondary peak, occurring approximately 4 hours before the main MTM peak.

Various studies to measure the occurrence of the MTM peak have been conducted in the last 60 years. Ground-based optical, radar, and in-situ measurements showed the MTM peak in airglow intensity, neutral density, electron temperature, and neutral temperature (e.g., Nelson and Cogger, 1971; Behnke and Harper, 1973; Arduini et al., 1997; Colerico and Mendillo, 2002; Meriwether et al., 2008; Gong et al., 2016; Figueiredo et al., 2017). Spencer et al. (1979) used the Neutral Atmosphere Temperature Instrument (NATE) on the Atmosphere Explorer-E (AE-E) satellite to measure the MTM at 275 km (Figure 1.6), while Bamgboye and McClure (1982) showed the MTM in the electron temperature, using Jicamarca Radio Observatory data. Remote (ground-based) optical instrumentation was more widely employed to investigate the MTM due to its wider availability. Colerico et al. (2006) showed the relationship between the MTM and the midnight brightness wave over the South American sector using 630 nm all-sky imagers. The secondary peak of the MTM was observed in the study by Faivre et al. (2006). The authors used the NRLMSISE/00 as the thermal background without the MTM to show that the main and secondary MTM peaks had values of 150-200 K and 50-70 K, respectively.

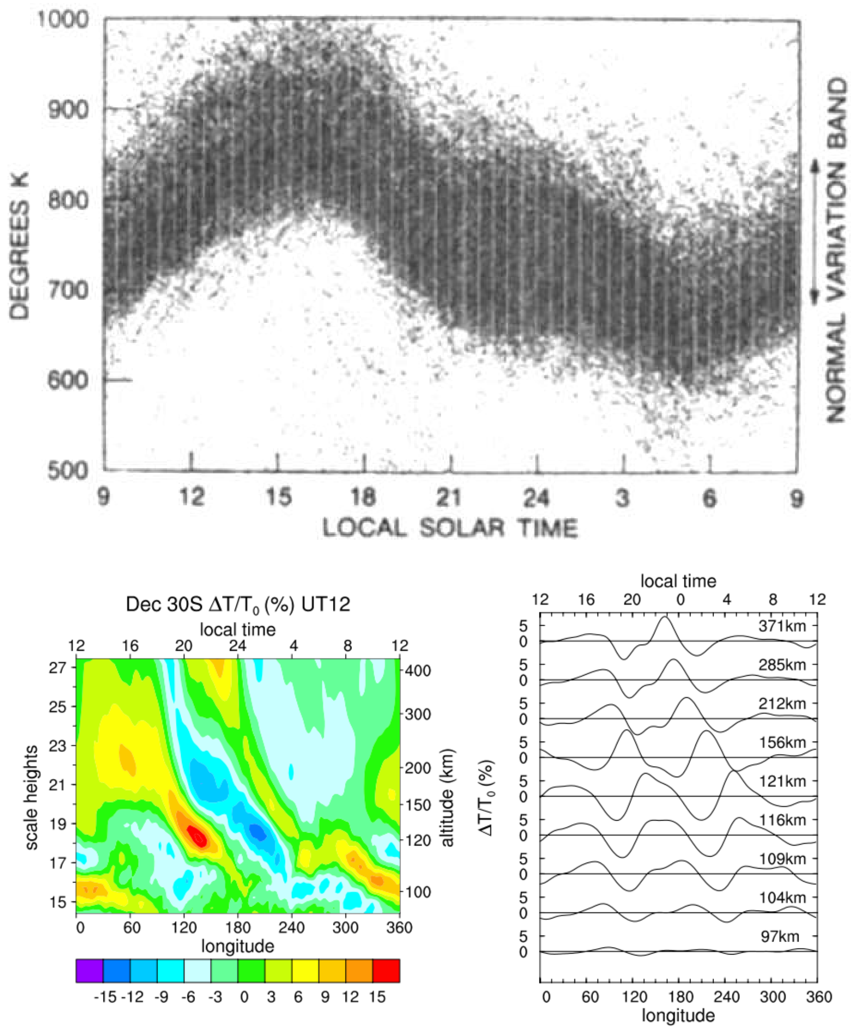

Figure 1.6: Top: Collection of temperature profiles at 275 km from the NATE instrument on board the AE-E satellite (Spencer et al., 1979). The MTM can be seen at 24 local solar time. Bottom: WAM results by Akmaev et al. (2009). Double peak MTM structure is evident in the thermosphere, with maxima separated by approximately 4 hours.

While the studies mentioned above shed light on the MTM phenomenon, there are still unanswered questions about its latitudinal range of propagation and the seasonal variation of both its peaks. These earlier observational studies were confined to $\pm 20°$ degrees latitude range, which represents one limiting factor. In addition, it was difficult for those authors to observe the secondary MTM peak using optical instrumentation because this peak usually originates before the evening twilight in that latitude range. The question to be addressed in this dissertation is: What are the characteristics of the mid-latitude MTM? In Chapter 2, it is shown that both primary and secondary peaks of the MTM extend as far north as 42° N in the mid-latitude F-region. The timing of the temperature peaks oscillates with annual and semi-annual periods.

1.4.2 Kelvin-Helmholtz Instability

One of the main mechanisms of mixing and redistributing energy and momentum is dynamical instabilities, which are often observed in the troposphere and mesosphere. The negative lapse rate of these layers lowers the mean static stability, allowing the development of instabilities. Among others, the Kelvin-Helmholtz instability (KHI) is commonly observed in regions of lowered static stability and is one of the paths between laminar and turbulent flows. The KHI is often referred to as shear instability due to its triggering mechanism. In it, a wind shear causes the fluid to swirl onto itself as described in Figure 1.7 adapted from Barbulescu and Erdélyi (2018). This figure also depicts the characteristic appearance of a fully developed KHI in panel (d), which is often called a *cat-eye structure* or simply an *eddy*.

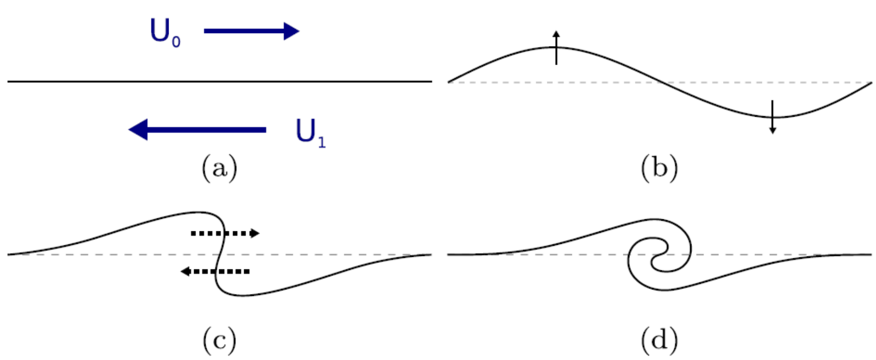

Figure 1.7: Kelvin-Helmholtz instability diagram showing its triggering mechanism (adapted from Barbulescu and Erdélyi, 2018).

While wind shears are required to trigger the KHI, the static stability of the media plays a large role in determining the triggering mechanism of this phenomenon. The mesospheric KHI is triggered by the shears associated with gravity wave-breaking or the superposition of gravity waves. These shears tend to be short-lived (<15 minutes) and small in magnitude (<25 ms^{-2}). However, a small shear is enough to develop the KHI in the reduced static stability of that region. The KHI phenomenon and its triggering mechanism in the mesosphere has been widely reported, primarily through radar and optical measurement techniques (e.g., Bishop et al., 2004; Pfrommer et al., 2009; Baumgarten and Fritts, 2014; Chau et al., 2020).

In the thermosphere, where the temperature profile is nearly isothermal or with positive lapse rate, the conditions are more stable. However, the KHI phenomenon has been observed above the mesopause a number of times (e.g., Hysell et al., 2012; Larsen et al., 2005). In this region, a much larger and longer-lasting shear is necessary to generate a KHI. Larsen (2002) showed that the low thermosphere (between 100 and 110 km) often features large shears that meet the criteria for KHI development (Richardson number smaller than 0.25). However, observations of the KHI in this altitude range are sparse because it is significantly harder to measure its structure. The altitude range above 100 km is outside the range of most lidar instruments and only a few radars can measure the electron density in fine enough resolution to serve as proxy for the KHI (Hysell et al., 2012).

Sounding rocket experiments are another source of KHI observation in the region above the mesopause. Larsen et al. (2005) generated observational images of the KHI between 100 and 115 km altitude. Although these KHI observations represent relevant evidence of its occurrence and characteristics, the evolution of the KHI features and breakdown into turbulence in the thermosphere were not discussed.

1.4.3 High-latitude forcing and advective acceleration

The region of enhanced acceleration due to Lorentz forcing (electric field-dependent, term F in equation 1.1) is the auroral oval. Within this region, the solar-wind-driven electric fields cause the ion motion in the convection pattern to dominate the motion of neutrals above approximately 120 km altitude in the thermosphere. Winds within this acceleration channel are typically faster in the presence of substorms (Larsen et al., 1997). The effect of this acceleration (and others such as Coriolis, centrifugal, advection, and pressure gradient) in the high-latitude neutral winds has been investigated experimentally and thoroughly characterized through modeling (e.g., Mikkelsen et al., 1981; Mikkelsen et al., 1981; Killeen and Roble, 1984; Larsen et al., 1997; Kwak and Richmond, 2007; Fuller-Rowell, 2013).

In the boundary of the region of enhanced Lorentz acceleration, a strong wind gradient causes the advective acceleration to become a significant source of forcing. This non-linear acceleration is the manifestation of the bulk transport of the geophysical quantities in the direction of the wind vector. Measuring this acceleration in the E-region is challenging because one must measure both winds and wind gradients simultaneously over a specified scale. This acceleration has been investigated through modeling and revealed that advection can become a dominant term in the neutral momentum equation (Mikkelsen et al., 1981; Killeen and Roble, 1984; Fuller-Rowell and Rees, 1984; Kwak and Richmond, 2007). At the time of this dissertation, no reports were found that included estimations of the advection from observations. Estimations of the wind gradients, necessary to calculate this acceleration, have been sparse in the thermosphere (Anderson et al., 2012; Aruliah and Griffin, 2001, and references therein). However, from the modeling studies it is clear that this acceleration can be important during active geomagnetic conditions. Therefore, understanding advective acceleration behavior is crucial to determine the effects of auroral activity on the neutral winds.

Other accelerations such as Coriolis and centrifugal are also important in the high-latitude sector. The Coriolis force creates a tendency for an air parcel to turn to the right. This causes a westward moving air parcel to turn poleward. The centrifugal force always points equatorward, which balances to a high degree the meridional component of the Coriolis force in the thermosphere Mikkelsen et al. (1981). The Hall ion drag is another acceleration that causes winds to change direction. Larsen and Walterscheid (1995) discussed the turning tendency of flows in the thermosphere by introducing the modified Coriolis parameter in the modified geostrophy study. They found that Hall drag causes a reduction of the Coriolis parameter, which lessens the poleward turning tendency discussed above.

Accelerations such as the Coriolis and centrifugal do not require the measurements of gradients and therefore are simple to observe. However, the overall behavior of these accelerations in different geomagnetic conditions and the interactions among Hall drag, Coriolis, and centrifugal accelerations are still unknown. To address this issue the meridional neutral momentum equation can be rewritten as

$$\frac{\partial v}{\partial t} = F_y + \frac{\sigma_H B^2}{\rho} u - fu - \frac{u^2}{R} \tan\theta, \tag{1.8}$$

where $f = 2\Omega \sin\theta$ is the standard Coriolis parameter, R is the radius of the Earth plus the altitude of measurements, and θ is the latitude of measurements. The term F_y represents all the forcing terms that cause a change in momentum (push or pull), while the explicitly written terms cause a change in direction (turn). Focusing only on the turning terms by making the rest of the forces $F_y = 0$, we have

$$\frac{\partial v}{\partial t} = -\left(f + \frac{u}{R}\tan\theta - \frac{\sigma_H B^2}{\rho}\right)u, \tag{1.9}$$

where $u/R\tan\theta$ is the centrifugal parameter and $\sigma_H B^2/\rho$ is the Hall drag. We can then define a modified Coriolis parameter (similar to Larsen and Walterscheid, 1995, but further modified by the centrifugal parameter) as

$$\Psi = f + u\frac{\tan\theta}{R} - \frac{\sigma_H B^2}{\rho}. \tag{1.10}$$

The investigation of the modified Coriolis parameter Ψ is important because it defines the behavior of an air parcel with zonal wind u, in the meridional direction. For example, winds tend to strongly accelerate westward in the pre-magnetic midnight sector due to ion drag Conde et al. (2001). The region of enhanced ion drag is the auroral oval and is here referred to as the acceleration channel. The longer an air parcel stays in the acceleration channel, the faster it becomes. For $\Psi = 0$, there will not be a turn in the meridional direction, keeping the air parcel in the acceleration channel for a longer period of time and allowing it to accelerate to higher speeds (assuming the oval mainly extends in the zonal direction). Therefore, understanding this quantity is crucial to determine the reason for the acceleration of fast winds in the lower E-region.

1.5 Experimental Methods

Various instruments were used to measure the neutral winds and temperatures in the upper atmosphere in the three studies discussed in Chapters 2-4 of this dissertation. The Fabry-Perot interferometer (FPI) network was used in the MTM paper (Chapter 2) and the sounding rocket technique was used in the KHI and advection papers (Chapters 3 and 4). The details of each measurement technique are discussed, including the advantages and disadvantages of each. Basic characteristics of the Poker Flat Incoherent Scatter Radar (PFISR) used in the advection paper will also be introduced.

1.5.1 Instruments Supporting the MTM Paper (Mesquita et al., 2018)

The instrument used to measure the temperatures in the F-region for the MTM paper (Chapter 2) was the network of Fabry-Perot interferometers in the North American Thermosphere Ionosphere Observing Network (NATION). The Fabry-Perot interferometer (FPI) measures the wavelength of optical emissions. In the case of the measurements presented in this dissertation, Doppler shift and broadening of the O(1D) atomic oxygen emission were used to estimate winds and temperatures at 250 km.

In its simplest form, the FPI consists of two semi-reflective parallel plates separated by a gap called the etalon. Constructive or destructive interference of the light passing through these plates creates an interference pattern, displayed in one dimension in Figure 1.8.

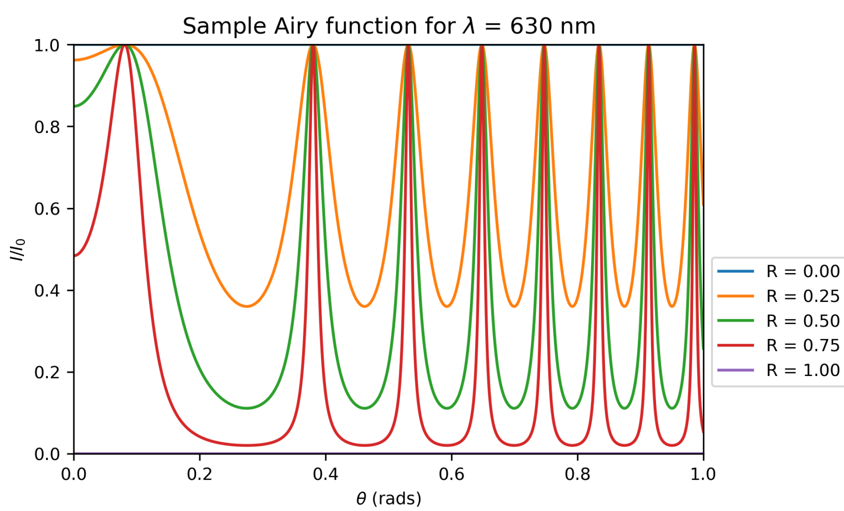

Figure 1.8: One-dimensional Airy function pattern for 630 nm wavelength, varying the reflectance.

The Airy pattern is shown in Figure 1.8. The function that describes this pattern is described by equation 1.11 (chapter 3.1.1 of Fisher, 2013),

$$I = \frac{I_0}{\left(1 + \frac{4R}{(1-R)^2}\sin\left(\frac{2\pi n t \cos(\theta)}{\lambda}\right)\right)} \tag{1.11}$$

,

where $I = |E_{\text{trans}}|^2$ and $I_0 = |E_{\text{inc}}|^2$ are the intensity of the transmitted and incident light. The quantities R, n, t, λ, and θ are reflectivity of the etalon plates, index of refraction between the plates, distance between the plates, wavelength of incident light, and incident angle.

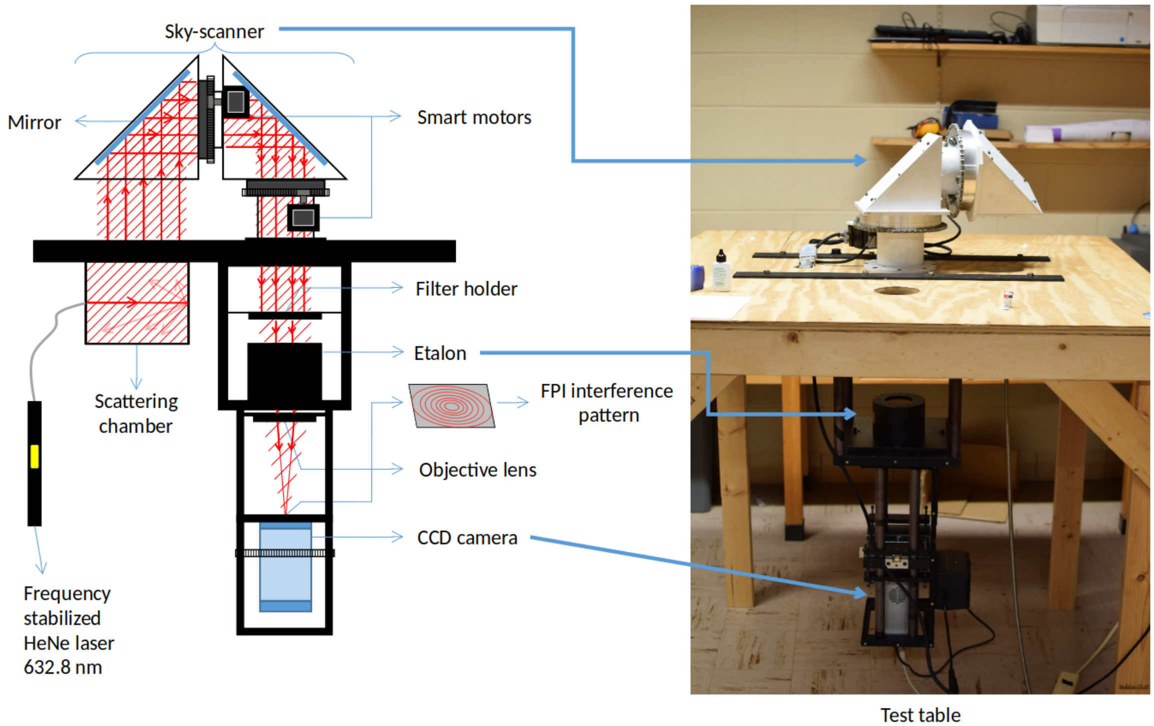

Figure 1.9: FPI schematics in laser calibration mode. Picture on the right shows the FPI on the test table.

In reality, the FPI instrument is a much more complex instrument than a simple etalon. A semi-complete system is displayed in Figure 1.9 in calibration mode. The installation and day-to-day operation are described in the internal manual by Mesquita (2015). The FPI contains a HeNe laser with stable emission wavelength of 632.8 nm that serves as a reference for the instrument, a scattering chamber, a periscope-like device called a sky-scanner that can be used to adjust the pointing angles of the FPI, a 630 nm narrow-band optical filter, an etalon, an objective lens, and a charge-coupled device (CCD) camera. The measured intensity of the frequency-stabilized HeNe laser and the oxygen 630 nm emissions (in photon counts), captured with a charge-coupled device (CCD), are shown in Figure 1.10. The calibration mode displayed in Figure 1.9 differs from the airglow measurement only by the pointing angles of the sky-scanner, which can be aimed in various directions of interest.

The Doppler shift and broadening of the 630 nm atomic oxygen emission are used to estimate

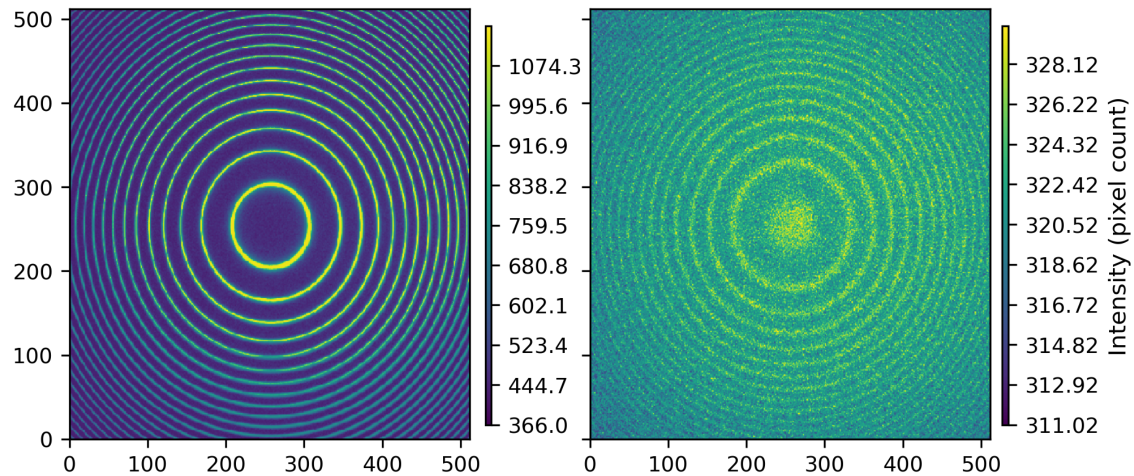

Figure 1.10: FPI interferometric pattern. Left panel represents a filtered HeNe laser pattern that is used as a reference for fluctuations in the instrument itself. Right panel represents the airglow measurement.

the winds and temperatures. Figure 1.10 shows the interferometric pattern from an FPI in the calibration (laser) and airglow (sky) measurements. A single fringe holds all the information about the Doppler shift and broadening. Using a single laser fringe, and assuming this fringe to be Gaussian, the temperature of the emission can be estimated by calculating the full width at half maximum (σ_{FWHM}) of the emission and applying equation 1.12.

$$T_n = \frac{\sigma^2_{\mathrm{FWHM}} m}{2k_B}, \tag{1.12}$$

where k_B is the Boltzmann's constant and m is the mass of the oxygen. Similarly, equation 1.13 is used to determine the line-of-sight (LOS) winds.

$$U_{\mathrm{LOS}} = \left(\frac{\lambda_{630} - \lambda}{\lambda_{630}}\right) c, \tag{1.13}$$

where λ_{630} is the theoretical wavelength of the emission, measured using the laser calibration, and λ is the wavelength of the emission measured by pointing the sky-scanner to the portion of the sky to be measured. Further details on the data processing technique, in which every fringe of laser and sky is fitted to determine LOS winds and temperatures, are described by Harding et al. (2014). The authors note that this procedure yields winds and temperatures with errors of approximately 2 ms^{-1}

and 6.5 K, given a signal-to-noise ratio (SNR) of 5. Another strategy to maintain a good cadence versus the measurement error is the dynamic integration, where the error is estimated image-to-image and the integration time is adjusted accordingly. This observation technique was discussed in detail by Mesquita et al. (2018).

The directions in which measurements of temperature and LOS winds are taken largely determine the geometry of the measurements. The most commonly used configuration of viewing angles in this dissertation are zenith (sky-scanner pointing up) and the cardinal directions by varying the azimuth angle (ϕ) with a 45-degree elevation angle ($\alpha = 45$). This configuration is known as the Cardinal Mode and yields winds and temperatures in five directions (north, south, east, west, and vertical) through the rotation in equation 1.14.

$$U_{\mathrm{LOS}} = w\sin(\alpha) + [vcos(\phi) + u\sin(\phi)]\cos(\alpha) + \gamma \tag{1.14}$$

Here we write u, v, and w as the horizontal winds in zonal and meridional directions, and the vertical wind. The angles α and ϕ in equation 1.14 represent the elevation and azimuth angles. The γ is the zero-Doppler offset. The laser calibration is used to determine changes in the instrument-related parameters, such as the reflectivity of the etalon plates, the etalon gap, and the falloff of intensity from the center of the image to the edges. The winds measured in the vertical direction are usually the zero-Doppler reference. This wind is historically assumed to be zero, since the F-region is assumed to be in hydrostatic equilibrium. That is generally a good assumption, since previous measurements show that vertical winds are more than an order of magnitude smaller than horizontal winds. Even though the vertical winds can be large in the F-region (Larsen and Meriwether, 2012), the estimation of horizontal neutral winds is usually discarded in the case of large vertical wind measurements. Measurements with viewing angles that coincide with the sky position of the Sun or the Moon and data with a high likelihood of cloud coverage (assessed by employing a Boltwood cloud sensor as discussed by Thompson, 2005) are also discarded.

The experimental errors are associated with both the instrument and with geophysical conditions. One clear source of error is cloud coverage and atmospheric scattering. While the measurements used in this dissertation were filtered from any cloud-contaminated data, Harding et al. (2017) discussed the effects of atmospheric scattering on ground-based FPIs. They discussed that tropospheric molecules and aerosols may scatter the horizontal motion of the 630 nm layer into the sky-scanner while it measures the vertical wind. The authors argued that this effect is stronger during active geomagnetic periods in the higher latitude regions where the aurora imposes a large latitudinal gradient in the 630 nm emission. An example of error associated with the instrument is large temperature fluctuations in the building where the instrument is installed. The etalon gap (distance between the etalon plates) can vary through the night as a results of the fluctuations. To mitigate this source of error one must track the gap through the night using the procedure described by Harding et al. (2014).

While equation 1.14 is used to solve for the horizontal winds, there are a few disadvantages to using a single FPI to measure the F-region winds. First, one cannot produce simultaneous observations of vertical winds and LOS winds. When estimating the LOS winds with the sky-scanner pointing at a 45-degree elevation angle in the northward azimuthal direction ($\phi = 0$), equation 1.14 gives the meridional wind. However, assuming that the altitude of the 630 nm emission is 250 km, the horizontal distance between the vertical winds measurement and the LOS winds is 250 km at an angle of 45 degrees. The peak 630 nm emission is broad in altitude, but temperature and winds are fairly uniform in this region making this a generally good assumption. Second, also based on equation 1.14, one can only estimate the zonal or meridional wind by pointing the sky-scanner in the north/south direction for the meridional wind, or east/west direction for the zonal wind. Lastly, the spatial range of operation for most narrow-field FPIs is rather restrictive. For example, a viewing angle of 45 degrees elevation yields approximately a 250 km radius of observation. Decreasing the elevation angle would likely amplify scattering effects from the lower atmosphere and light contamination from ground sources (Harding, 2017).

The disadvantages discussed above can be addressed by using a network of FPIs such as NATION. The use of networked-FPIs enables the bi-static and tri-static measurements in which two or three FPIs observe the same common volume of the atmosphere, resulting in simultaneous two- and three-dimensional measurements of the winds. The observation of larger scale phenomena is also possible through the use of a network of FPIs. In the case of the results presented in this dissertation (Mesquita et al., 2018), the NATION network covers an area approximately 1200x1300 km in the eastern US. The work presented by Mesquita et al. (2018) and in chapter 2 relies heavily on the larger area covered by the NATION network to investigate the behavior of the MTM, which is a large scale global phenomenon.

1.5.2 Instruments Supporting the KHI and the Advection Papers (Mesquita et al., 2020, and Chapter 4)

The KHI and advection papers in Chapters 3 and 4 use triangulation of vapor tracers released from sounding rockets to measure the neutral winds in the E-region. This technique has been one of the preeminent methods to determine the neutral winds in the mesosphere and thermosphere since the early 1950s (Bates, 1950). Figure 1.11 shows the suborbital sounding rocket vehicles at NASA's disposal, each with a different operational range and purpose.

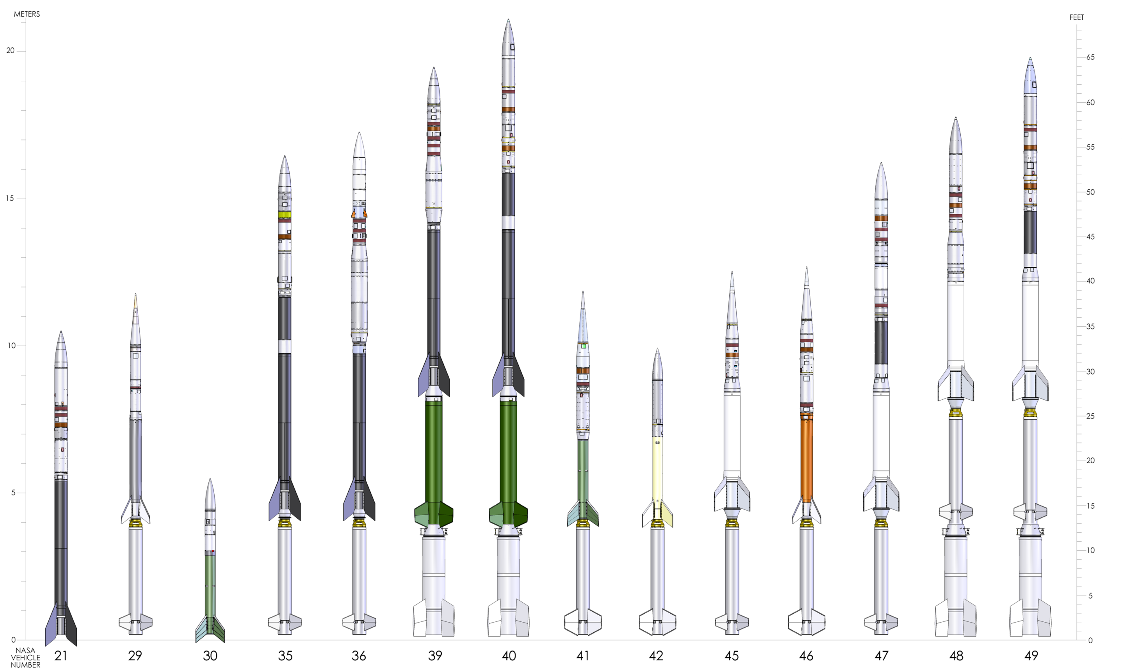

Figure 1.11: NASA suborbital sounding rocket vehicles. Rockets are usually identified by the vehicle number and the number of times they have been used. For example, the Super Soaker campaign launched two rockets carrying vapor tracers, which were 41.119 and 41.120 meaning the 119$^{\text{th}}$ and 120$^{\text{th}}$ times the vehicle number 41 was launched.

The technique requires launching a rocket equipped with a chemical tracer that is released in the altitude range and region to be studied. Larsen (2013) discusses in detail the payload and the TMA release canister. The tracer drifts with the neutral winds for a neutral tracer or with the $\vec{E} \times \vec{B}$ drift for an ionized tracer. The most widely used vapor tracer is trimethylaluminium (TMA); but other chemicals can also be used, such as sodium, barium, strontium, or lithium. These tracers produce light through chemiluminescence or through solar photoexcitation. TMA is a pyrophoric liquid that burns intensely in the presence of oxygen. As it burns, TMA emits a white light that is visible from the ground at night. In daylight, TMA produces a blue emission, which is common in the higher altitude releases in the F-region or at twilight.

As the rocket reaches the altitude range of interest, it begins to release the TMA. This creates a distinct narrow trail along the rocket trajectory, which quickly assumes the horizontal motion of the atmosphere, drifting with the neutral winds. The trail is then photographed from several camera sites that could be ground-based or airborne. The photographs are used to track the motion of the trail over time. The TMA trails are triangulated in a semi-automatic process developed by Ingersoll (2008). The different perspectives from which the TMA trails are photographed are used to triangulate the trail and determine its position at any particular time-step. A basic diagram of triangulation is presented in Figure 1.12.

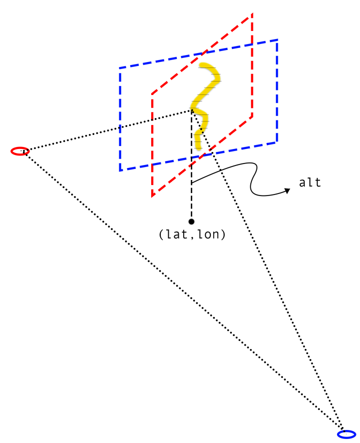

Figure 1.12: Diagram of the triangulation technique.

Figure 1.13 shows the morphology of the triangulation. Manually inputted pixels along the TMA trail are transformed in the right ascension and declination, a process that is repeated for both images. Camera locations are then used to determine the position of the trail with a high degree of accuracy (usually on the order of $\lesssim$ 100 m). After recording a time-series of the TMA trail positions, the velocity of the profile can be determined by a simple linear fit. The TMA moves linearly with the neutral winds, which makes this a valid model to estimate the neutral winds within the time-scale in which the TMA profiles are visible from the ground (between 5 and 20 minutes).

Determining the wind profiles using the time evolution of the TMA profile requires a number of assumptions. The main assumption is that the vertical winds must be much smaller than the

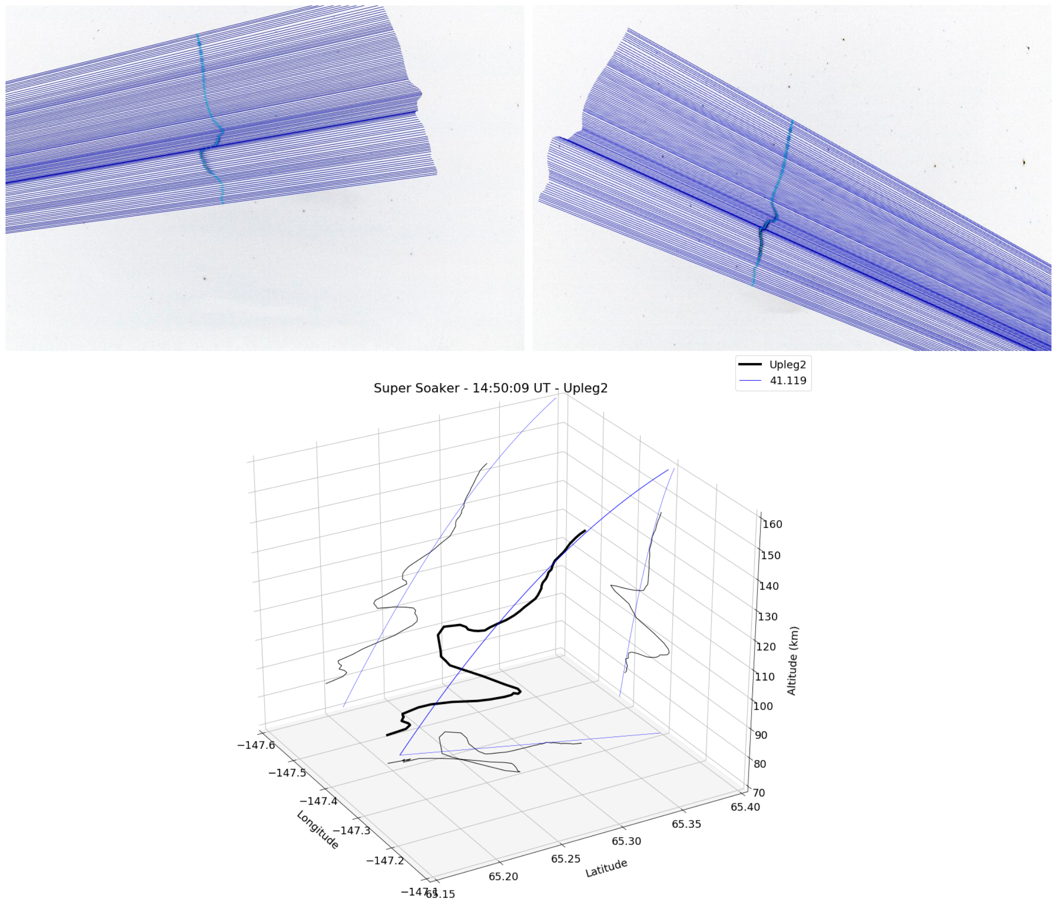

Figure 1.13: Concurrent negative photographs of the TMA trail and the three-dimensional representation of the triangulation result. The images in the top panel contain the projection lines that connect the TMA trail and the position of the camera site; i.e., if followed to the left, the blue lines in the top left panel lead to the camera site where the picture in the top right was taken. The triangulation result is represented by the dark black line, along with each planar projection by thin black lines. The blue ballistic-like trajectory is the rocket track.

horizontal winds. A strong vertical wind results in a non-linear evolution of the position with time. This is generally a good assumption, since the vertical winds are relatively small between 100 and 150 km, which is the altitude of interest in this text. Figure 1.14 shows the position of the TMA with time as well as the linear fitting necessary to determine the velocity in units of latitude and longitude per second.

The fitting procedure displayed in Figure 1.14 results in velocities with units of (latitude and longitude in) radians per second. Equations 1.15 are then used to transform radians per second

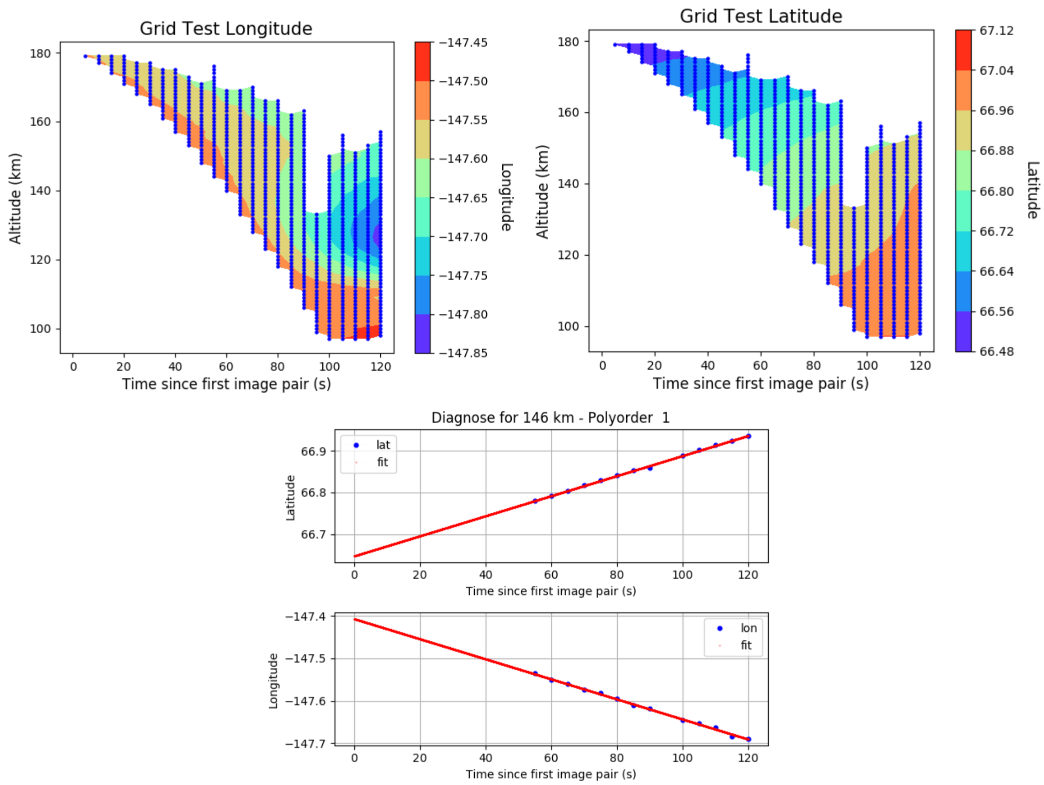

Figure 1.14: Top panel: An example of the evolution of the four-dimensional grid (latitude, longitude, altitude, and time) of the TMA. The blue dots in this panel represent the altitudes in which the latitude and longitude are determined. Bottom panels: A representation of the linear fitting of TMA latitude and longitude at 146 km. The blue dots represent the measured positions of TMA, while the red line is the fitting line.

into meters per second, i.e., in zonal and meridional winds. These winds are

$$u = r\cos\theta\frac{d\phi}{dt} \quad \text{and} \quad v = r\frac{d\theta}{dt}, \tag{1.15}$$

where r is the radius of the Earth plus the altitude of the measurement, u and v are the zonal and meridional winds, and θ and ϕ are latitude and longitude. The derivatives have units of radians per second, which result from the fitting procedure.

This approach yields measurements with a high degree of accuracy to determine the winds in the upper atmosphere. The measurement error is associated with the distance of closest approach between the two projections at any given point in the TMA trail. This quantity is usually small (<100 meters) and is used as the uncertainty of the latitude and longitude in the fitting. The distance between the two projections is used as a weight for the linear fitting (the point with smaller distance between projections is more significant in the fitting). The square root of the computed variance of this fitting results in the measurement error. Typical errors are approximately 5-10 ms^{-1}. The distance between the two projections is usually smaller than 100 meters and careful repetition of the triangulation decreases the error by a factor of square-root of the number of triangulated images. Larsen (2002) shows a comprehensive list of wind profiles measured with the sounding rocket technique from 1958 to 2002, mostly with the release of TMA.

The use of sounding rocket releases to investigate the dynamics of the upper atmosphere has the advantage of being the most accurate way to measure winds in the E-region. The two main disadvantages of this method are the lack of time-series measurements and the operational cost. As a result, most ionospheric data sets come from ground-based instrumentation because it is cost effective and easy to develop, install, and operate the instruments. However, these instruments also have major disadvantages. Passive optical instrumentation, such as scanning Doppler interferometers (SDI) and FPIs, rely on the use of a certain atmospheric emission to generate meaningful measurements. That can be challenging in the E-region due to commonly observed shear in the lower E-region where the oxygen green line peaks (Larsen, 2002).

Incoherent scatter radars (ISR) have also been used to determine the neutral wind profiles in the E-region, using the technique developed by Brekke et al. (1973) and reviewed by Johnson (1990). However, ISRs are expensive to deploy and require a minimum amount of electron density in the E-region to generate any meaningful results, which can be challenging at night and in the high-latitude winter. This measurement technique can only determine a local wind profile. Techniques to determine the E-region wind gradients have not been tested. The TMA trails can be released from the rocket both before and after its apogee (trails called upleg and downleg). This creates a two-dimensional separation between upleg and downleg that enables the calculation of the winds and the gradients along the entire rocket trajectory.

Chapter 3 follows the lifetime of a KHI with a high degree of accuracy by determining the position of the TMA trail in three dimensions. Wind measurements were also estimated and used to calculate the KHI parameters. Chapter 4 uses the two-dimensional separation between the upleg and downleg wind profiles to estimate the meridional advective acceleration. All of the rockets used in this dissertation were launched from Poker Flat Research Range in Chatanika, Alaska, at (65.13°N, 147.47°W).

1.5.2.1 Other Supporting Instrumentation

The Poker Flat Incoherent Scatter Radar (PFISR) was used in the study discussed in Chapter 4. It is one of the Advanced Modular Incoherent Scatter Radar (AMISR) systems. It is an electronically steerable radar that changes the beam phase of each of the transmitting antennas to probe different regions in the ionosphere. This radar has been in nearly continuous operation since early 2007, providing support for a number of sounding rocket campaigns. Figure 1.15 shows a birds-eye view of Poker Flat Research Range, where the rockets were launched, and the PFISR instrument location.

As shown in Figure 1.15, the radar is tilted 15 degrees east of north with its bore sight at a 74-degree elevation angle. These angles were chosen to provide maximum downrange coverage for the rocket measurements while also being able to take measurements up the magnetic field line. The possible viewing directions are described by Heinselman and Nicolls (2008) and are limited by the lobe limits of the transmitted beams.

This radar measures in two simultaneous beam modes, the alternating code and long pulse. As the name suggests, the long pulse (LP) consists of 480 μs pulses with an approximately 72 km range resolution. This beam is suitable for F-region measurements, which are higher in altitude. The alternating code (AC) corresponds to shorter pulses of 30 μs and approximately 5 km of range resolution, suitable for E-region measurements. The beam width is approximately 1° and its gain decreases with the cosine of the angle off bore sight. The true transmitting power of PFISR is 1.3 MW and 1.7 MW before and after its September 2007 upgrade from 96 to 128 panel systems. PFISR also has a maximum duty cycle of 10%, which is the pulse width divided by the pulse repetition time.

The PFISR can measure both the velocity and density of plasma. Velocity is measured by estimating the difference in wavelength between the transmitted and received beams in the radar's line-of-sight. This velocity is then converted to horizontal vector velocities through a Bayesian algorithm described by Heinselman and Nicolls (2008). The plasma density is related to the difference between the transmitted and received powers and is calculated through the integration of the auto-correlation function (ACF). The fitting of the ACF is one of the main sources of error, when measurements with low SNR cause an asymmetric (noisy) spectra. The measurement errors are also described by Heinselman and Nicolls (2008).

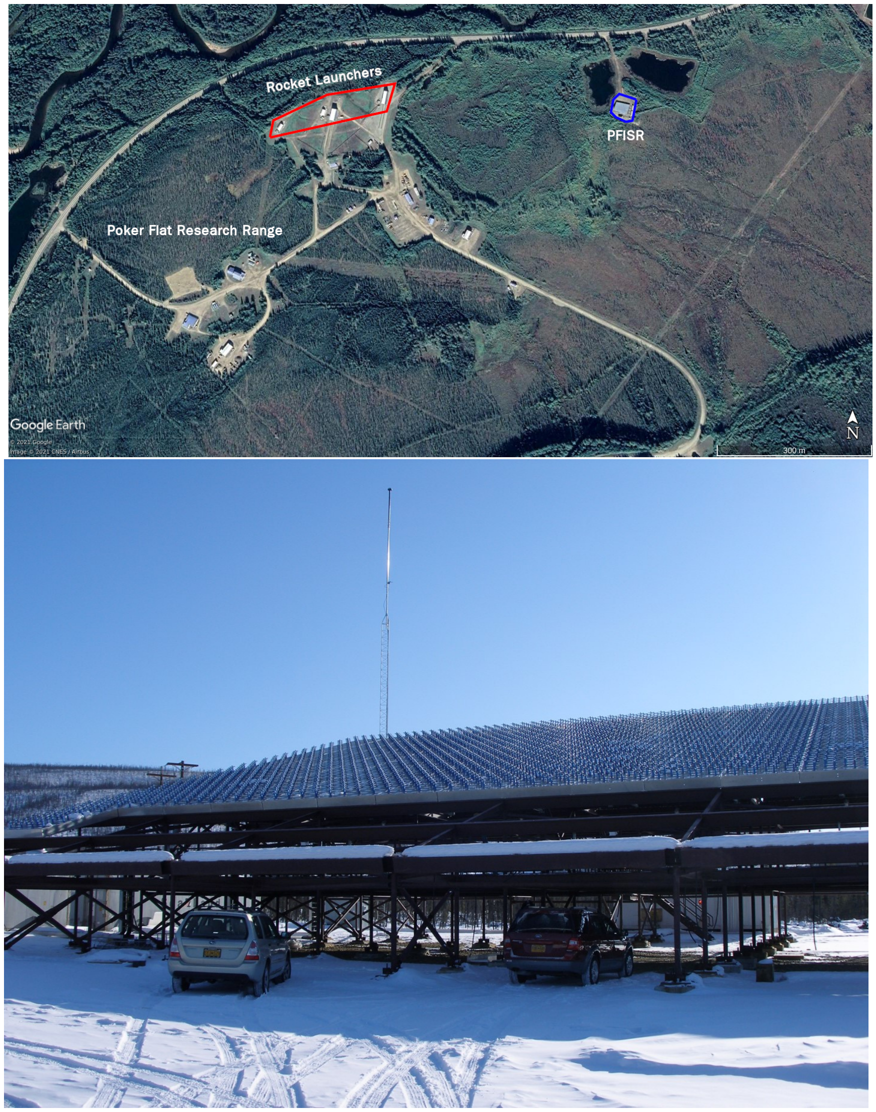

Figure 1.15: Top: A summertime satellite photo of the Poker Flat Research Range, showing the rocket launchers (red) and the PFISR instrument (blue). Bottom: Close-up picture of PFISR (photo credit Mike Kosch).

In the study presented in Chapter 4, both the AC and LP modes were used to measure the E-region plasma density profile and F-region plasma velocity. The plasma density was used to estimate the Hall and Pedersen drag coefficients. These quantities and the F-region plasma velocity were used in the modified version of equation 1.7 in the absence of neutral winds. More details are in Chapter 4.

1.6 Scientific Questions and Organization

1.6.1 Objective of the Study in Chapter 2 - New Results on the Mid-latitude Midnight Temperature Maximum (Mesquita et al., 2018)

The study in Chapter 2 explores the mid-latitude midnight temperature maximum using the NATION network of FPIs. As discussed in section 1.4.1, the MTM is a global phenomenon that originates at the equator. The following scientific questions are addressed by this study:

1. How should the amplitude of the MTM peak be estimated for the NATION network of FPIs?
2. Does the secondary MTM peak manifest in mid-latitude?
3. How far off the equatorial line do the MTM peaks manifest?
4. What is the seasonal variability of both MTM peaks in mid-latitude?
5. How does the two-dimensional structure of the MTM peaks relate to the wind field in the mid-latitude sector?

Earlier studies of the MTM characterized the amplitude of the phenomenon in one of three ways: 1) by connecting the local minima in the temperature curve with a line, 2) by using a model such as NRLMSISE/00 to characterize the thermal background, or 3) by fitting the temperature data with a combination of tidal oscillations and a Gaussian curve. The amplitude for methods 1 and 2 is estimated by subtracting the reference curve from the temperature data. Methods 2 and 3, model and fitting, give the best results. The study by Faivre et al. (2006) is an example of the model background, while the paper by Martinis et al. (2013) used a fitting procedure that included the MTM peak. The FPI data from NATION was included in the NRLMSISE/00 estimation of temperatures, which rendered the model inept for producing a thermal background. The full fitting, such as that performed by Martinis et al. (2013) was also not possible due to the low number of hours of measurements to be fitted: 12 hours at best. The thermal background was, however, built by fitting diurnal, semidiurnal, and terdiurnal tidal oscillations to the FPI data without the MTM peaks.

In the first few decades of MTM observations, the phenomenon was usually believed to be a single peak that originated at the equator. However, modeling studies such as the one done by Akmaev et al. (2009) showed the presence of a secondary peak. Observations of the secondary peak are sparse due to the measurements in low latitude, where the peak manifests early in the night, making it difficult to observe with passive optical ground-based instruments. The NATION observations discussed in Chapter 2 confirm the presence of the MTM as far north as 44.4°N. In the same chapter, the seasonality of the MTM is discussed through the hourly bin average of the residuals and fitting of the peaks (temperature data minus the fitted thermal background).

By using the background removal technique, the temperature was interpolated in two dimensions, which created temperature and wind measurements in a broad area. These extended over ∼1200 km in the widest latitudinal and longitudinal separations. The temperature and wind maps were then used to assess the passage of the MTM and its effects on the flow field.

1.6.2 Objective of the Study in Chapter 3 - In-situ observations of neutral shear instability in the statically stable high-latitude mesosphere and lower thermosphere during quiet geomagnetic conditions (Mesquita et al., 2020)

The study in Chapter 3 is associated with the Kelvin-Helmholtz instability observed during the Super Soaker campaign. As discussed in section 1.4.2, the KHI has been widely observed in the mesosphere and, while its occurrence in the thermosphere is not uncommon, the details of the evolution and breakdown of the feature are still a challenge in that altitude range. The following scientific questions are addressed in the study:

1. What is the triggering mechanism of Kelvin-Helmholtz instabilities in statically stable regions?
2. How does the Kelvin-Helmholtz instability evolve in the low thermosphere?

These questions were addressed using detailed triangulation of the KHI development and wind calculations. The high-resolution triangulation, with errors of less than 100 meters, was used to determine the position of the TMA as it assumed the cat-eye structure associated with the KHI. The KHI evolved and broke down into turbulence soon after the passage of the rocket. The TMA released during its passage was quickly dispersed through turbulence in an altitude range above the turbopause. The Richardson number was estimated using the wind profiles and confirmed that the observed KHI, in the statically stable thermosphere, was caused by a large shear around 105 km altitude. This indicates that the mechanism of generating KHIs in the thermosphere is associated with large sustained shears in contrast with the mesosphere, where a more modest and short-lived shear could trigger a KHI.

1.6.3 Objective of the Study in Chapter 4 - Measurements of the meridional advective acceleration and neutral wind forcing in the E-region at different geomagnetic activity levels

The study in Chapter 4 presents the first set of observations of the meridional advection of the winds in high latitude. As previously mentioned, although difficult to measure, the advective acceleration can be estimated through the sounding rocket technique. Other terms in the neutral momentum equation (instantaneous Lorentz, Coriolis, and centrifugal accelerations) are also analyzed. The following scientific questions are addressed by the study:

1. How do the vertical distribution of forces in the E-region and the advection change as a function of geomagnetic activity?

Advection is an acceleration caused by the creation of gradients in the atmosphere. While it cannot be estimated fully by the rocket launch campaigns discussed in Chapter 4, a number of assumptions will be examined, indicating that meridional advection is the more significant horizontal advecting agent.

The meridional advection acceleration can be a significant source of forcing in the E-region in strong geomagnetic activity, on the order of $\sim$0.1 ms^{-2}. In active geomagnetic conditions, advection is crucial to explain the wind profile features. The advective acceleration was often larger than the Lorentz forcing, which is traditionally understood as the main driver of fast winds in the high-latitude sector and in the presence of aurora. The analysis of Ψ indicated that strong geomagnetic activity produced westward winds that tended to keep an air parcel in the acceleration channel or turn equatorward at $\sim$125 km.

1.6.4 Organization

This dissertation is a combination of three manuscripts presented in chapters 2-3. Chapters 2 and 3 represent articles that have been peer-reviewed and published by the journals. Chapter 4 will be submitted to the journal for the peer-review process. The organization of each manuscript is as follows.

For the MTM paper (Mesquita et al., 2018) and Chapter 2, details about the FPI instrument, the NATION observation modes, and the dynamic integration are discussed in the NATION network and instrumentation section. The harmonic background removal procedure is discussed in the following section. The next section presents the results, emphasizing the MTM double-peaked structure, the background-extracted temperature interpolation, and the climatology of the MTM. That section is followed by discussion and conclusions.

For the KHI paper (Mesquita et al., 2020) and Chapter 3, details of the Super Soaker launches are presented, followed by the results section that introduces geophysical quantities such as the dimensionless numbers: Richardson, Reynolds, Froude numbers. The results section also provides a detailed explanation of the triangulation technique that is used to identify the KHI features. The conclusions and discussion sections include a comparison of existing measurements of the KHI, followed by a brief summary of the findings.

For the high-latitude neutral wind forcing paper and Chapter 4, geomagnetic activity is assessed using the local magnetometer (at Poker Flat), and regional and global auroral electrojet indices. Sounding rocket observations of winds are used to calculate the meridional advective, Coriolis, and centrifugal accelerations. The Super Soaker, JOULE II, HEX II, MIST, and Auroral Jets campaigns were used in this study due to the concurrent PFISR observations. Instantaneous Lorentz acceleration estimation and meridional advective acceleration are then introduced, along with the assumptions necessary to estimate these quantities. The results subsection is divided into three categories: quiet, moderate, and strong geomagnetic activity. The modified Coriolis parameter and the winds are then discussed in the context of the measured forcing for each campaign. Finally, the discussion and conclusion sections outline the importance of advection and Ψ.

Chapter 2

New Results on the Mid-latitude Midnight Temperature Maximum

Rafael L.A. Mesquita[1], John W. Meriwether[1], Jonathan J. Makela[2], Daniel J. Fisher[2], Brian J. Harding[2], Samuel C. Sanders[1], Fasil Tesema K.[3], and Aaron J. Ridley[4].

[1] Physics and Astronomy Department, Clemson University, Clemson, South Carolina, USA.

[2] Department of Electrical and Computer Engineering, University of Illinois at Urbana-Champaign, Urbana, Illinois, USA.

[3] Washera Geospace and Radar Science Laboratory, Bahir Dar University, Bahir Dar, Ethiopia.

[4] Department of Atmospheric, Oceanic, and Space Sciences, University of Michigan, Ann Arbor, Michigan, USA.

Published as:

Mesquita, R. L. A., Meriwether, J. W., Makela, J. J., Fisher, D. J., Harding, B. J., Sanders, S. C., Tesema, F., and Ridley, A. J.: New results on the mid-latitude midnight temperature maximum, Ann. Geophys., 36, 541–553, `https://doi.org/10.5194/angeo-36-541-2018`, 2018.

Abstract

Fabry-Perot interferometer (FPI) measurements of thermospheric temperatures and winds show the detection and successful determination of the latitudinal distribution of the midnight temperature maximum (MTM) in the continental mid-eastern United States. These results were obtained through the operation of the five FPI observatories in the North American Thermosphere Ionosphere Observing Network (NATION) located at the Pisgah Astronomic Research Institute (PAR) (35.2° N, 82.8° W), Virginia Tech (VTI) (37.2° N, 80.4° W), Eastern Kentucky University (EKU) (37.8° N, 84.3° W), Urbana-Champaign (UAO) (40.2° N, 88.2° W) and Ann Arbor (ANN) (42.3° N, 83.8° W). A new approach for analyzing the MTM phenomenon is developed, which features the combination of a method of harmonic thermal background removal followed by a two-dimensional inversion algorithm to generate sequential 2-D temperature residual maps at 30 minutes intervals. The simultaneous study of the temperature data from these FPI stations represents a novel analysis of the MTM and its large scale latitudinal and longitudinal structure. The major finding in examining these maps is the frequent detection of a secondary MTM peak occurring during the early evening hours, nearly 4.5 hrs prior to the timing of the primary MTM peak that generally appears after midnight. The analysis of these observations shows a strong night-to-night variability for this double-peaked MTM structure. A statistical study of the behavior of the MTM events was carried out to determine the extent of this variability in regard to the seasonal and latitudinal dependence. The results show the presence of the MTM peak(s) in 106 out of the 472 determinable nights (when the MTM presence, or lack thereof, can be determined with certainty in the data set) selected for analysis (22%) out of the total of 846 nights available. The MTM feature is seen to appear slightly more often during the summer (27%), followed by fall (22%), winter (20%) and spring (18%). Also seen is a northwest-ward propagation of the MTM signature with a latitude-dependent amplitude. This behavior suggests either a latitudinal dependence of thermosphere tidal dissipation or a night-to-night variation of the composition of the higher order tidal modes that contribute to the production of the MTM peak at mid-latitudes. Also presented in this paper is the perturbation on the divergence of the wind fields, which is associated with the passage of each MTM peak analyzed with the 2D interpolation.

2.1 Introduction

The Earth's atmosphere is heated during the day by the absorption of solar energy and cooled at night by emission of thermal radiation energy to space. However, in the thermosphere there is seen quite often, near midnight, a temperature peak with an amplitude up to 200 K. This phenomenon is called the Midnight Temperature Maximum (MTM). This interesting nighttime phenomenon was first reported in the 1960's in ground-based optical, radar, and in situ measurements (Greenspan, 1966; Nelson and Cogger, 1971; Behnke and Harper, 1973; Spencer et al., 1979). Also associated with this temperature peak is a density enhancement called the Midnight Density Maximum that has been detected with drag balance instruments on board the San Marco III and V satellites Arduini et al. (1992, 1993, 1997). These previous studies of the MTM phenomenon were carried out with observations within 20 degrees latitude range of the equator. The present paper is unique as it presents results for the mid-latitude range between 30 and 45 degrees latitude.

As discussed in the analysis of the Jicamarca nighttime radar measurements of electron temperatures, Bamgboye and McClure (1982) suggested the MTM peak resulted from the upward propagation of atmospheric tidal waves and is associated with a pressure/temperature bulge near midnight. Their work confirmed the equatorial MTM behavior described earlier by Herrero and Spencer (1982), which was based on a statistical analysis of the observations from the Neutral Atmosphere Temperature Experiment (NATE) mass spectrometer experiment on board of the Atmospheric Explorer-E (AE) satellite. These results showed a latitudinal distribution for the MTM that accounted for the seasonal variability in its peak amplitude within the $\pm 20^o$ latitude range covered by the AE satellite. Their findings show that the MTM is formed at the geographic equator and propagates poleward and westward in both hemispheres. Regarding its seasonality, Herrero and Spencer (1982) noted the dominance of the MTM feature in the summer hemisphere, with the temperature maximum occurring earlier in local time and with higher amplitude when compared with the MTM behavior in the winter hemisphere.

The modeling work discussed by Mayr et al. (1979) concluded that the MTM is the result of a nonlinear interaction of the diurnal, semi-diurnal and other higher order tides. Colerico et al. (2006) reported on the sensitive influence of the terdiurnal as well as higher order tidal modes that enhance the MTM peak amplitude. They suggested that the superposition of these higher order tidal modes has a latitudinal distribution in such a way that the MTM amplitude would also be variable within a given latitude span. Determining this latitudinal variation of the MTM amplitude would help improve our understanding of how the overlap of these tidal modes at mid-latitudes may vary with latitude due to the individual latitudinal dependence of each tidal mode contributing to the overall tidal forcing from below. It is also possible that the contribution of a non-migrating tidal wave if significant may also vary with latitude.

The MTM latitudinal structure was recently modeled by Akmaev et al. (2009) to be a wake-wave shaped disturbance in temperature with a phase lag relative to the latitude, i.e. the timing of the MTM peak occurs later in the evening at higher latitudes. Their study confirm the MTM as being a result of the thermal part of the constructive interference between the upward propagating and the *in-situ* diurnal, semi-diurnal, and other higher order migrating tidal modes Akmaev et al. (2009); Akmaev (2011). Among these important findings, Akmaev et al. (2009) found evidence for a weak secondary maximum in their Whole Atmosphere Model (*WAM*) occurring earlier in the evening. This result agrees with the detection of a secondary MTM peak that was reported by Faivre et al. (2006) from observations in the Peruvian sector. For the remainder of our paper, the terms "secondary" and "primary" refer to the earlier and later MTM peak, respectively.

Colerico and Mendillo (2002) presented data showing the relationship between the MTM and the Midnight Brightness Wave (MBW) which is characterized by an enhancement in the 630-nm emission. Away from the geomagnetic equator, this correlation is a result of the reversal of the meridional wind component from equatorward to poleward causing a downward shift in the F-region plasma distribution and a consequent increase in the 630-nm emission by dissociative recombination Sastri et al. (1994).

The MTM peak is commonly observed in the equatorial region with typical amplitudes of 150-200 K Figueiredo et al. (2017). An example of an amplitude as much as 300 K associated with Sudden Stratospheric Warming events have been presented Gong et al. (2016). In the local summer as addressed by Meriwether et al. (2008) and Meriwether et al. (2011), the MTM was seen to move with an average velocity of 300 ms^{-1} (as observed by Sobral et al. (1978)). However, it is not clear what role the coupling interaction between this tidal wave to the lower thermosphere/ionosphere might play in governing the amplitude of the MTM's night-to-night variability. It is also not known how far away from the geographic equator the MTM structure would continue to be observed, what the resulting latitudinal distribution would be, and how this behavior varies from season to season. Modeling this important MLT/IT (Mesosphere and Low Thermosphere/Ionosphere and

Thermosphere) coupling mechanism still remains a challenging task due to the uncertainty associated with the source composition of the forcing function underlying the tidal wave production of higher order modes at mid-latitude.

The availability of results from 2012 to 2015 in the NATION mid-latitude wind and temperature database gives us an opportunity to consider these questions. With a coverage of approximately 1200 km and 1300 km in the zonal and meridional directions respectively, this extended geographic coverage is well suited for observing the propagation behavior of a large-scale phenomenon such as the MTM.

2.2 Instrumental details

2.2.1 FPI instrument features

Each NATION FPI instrument uses an etalon combined with a 630-nm filter, an objective lens, a low noise CCD camera, and a double axis Sky-Scanner system. The interference images obtained by each FPI were analyzed to determine the Doppler shift and Doppler broadening for each direction observed. From these line-of-sight Doppler shift results, the meridional and zonal horizontal components of the neutral wind vector are determined. The temperatures are derived from the measurement of the Doppler broadening. The relative intensity is directly measured as the area enclosed by the 630-nm spectral peak. Typically, the measurement uncertainties in the line-of-sight Doppler shift and temperature are on the order of 3-5 ms^{-1} and 15 to 20 K, respectively. Further details regarding the FPI instrumentation used in the NATION network are given by Makela et al. (2012) and Makela et al. (2014). The data reduction and temperature estimation details were discussed by Harding et al. (2014).

2.2.2 NATION observing modes and look angles

The aim of the NATION network was to measure mid-latitude thermosphere winds, temperatures, and 630-nm intensities over the latitude span of from 32° N to 42° N. In addition to the FPI instrument, each NATION site was equipped with a cloud sensor to determine the extent of cloudiness so data associated with these periods can be removed. The NATION FPI instruments were able to communicate with each other in real time via the internet. This allowed the observing strategy to be modified depending upon the extent of cloudiness.

The selection of the observing mode was either the Cardinal Mode (the sequence of North, South, East, West and Zenith) or the Common Volume (CV), mode in which two or three FPIs observe the same region of the thermosphere from different angles. The former mode is adopted when the skies for one of the two (or three) stations that might otherwise be used in CV mode is hazy or overcast; or for probing thermospheric phenomena that requires a larger coverage in both latitude and longitude. In the case of clear skies for two or three NATION stations, the network switched to the CV Mode. For this strategy, line-of-sight Doppler shift data within the same CV can be analyzed to extract the zonal and meridional components. Due to the large-scale nature of the MTM, only the NATION Cardinal Mode has been used for the results reported in this paper.

Figure 2.1 shows the location of the five NATION observatories (red, which also indicates the position for the Zenith measurement) and the locations of Cardinal Mode measurements (green) within the thermosphere, assuming a 250 km peak height for the 630-nm $O(^1D)$ emission. With this height and an elevation angle of 45 degrees for each azimuth position, the distance between pairs of North and South and West and East positions is 500 km. These Cardinal Mode observation angles were chosen in order to provide a large coverage of both latitude and longitude without any compromise in quality of observations. At lower elevation angles the measurements would likely be affected by ground-generated light pollution.

2.2.3 Dynamic integration in image collection

The method of image collection called dynamic integration for each instrument in the NATION FPI network followed a procedure of image analysis, for which each measured spectrum is analyzed by the data collection computer to re-assess the need for increasing or decreasing the integration time for the next image collected by the CCD camera. The intent for this practice was to maintain a desired ratio of signal to noise from one image to the next so wind and temperature measurements are obtained with nearly the same uncertainty throughout the night. As the airglow signal becomes weaker or stronger during the night, the application of this procedure would increase or decrease the exposure time accordingly. This approach improves the cadence of measurements, which is integration time (between 20-720 seconds) times the number of look angles in the observation mode (typically the 4 cardinal positions and zenith), that generally maintains the desired value of measured uncertainties as the 630-nm airglow intensity varies throughout the night. This

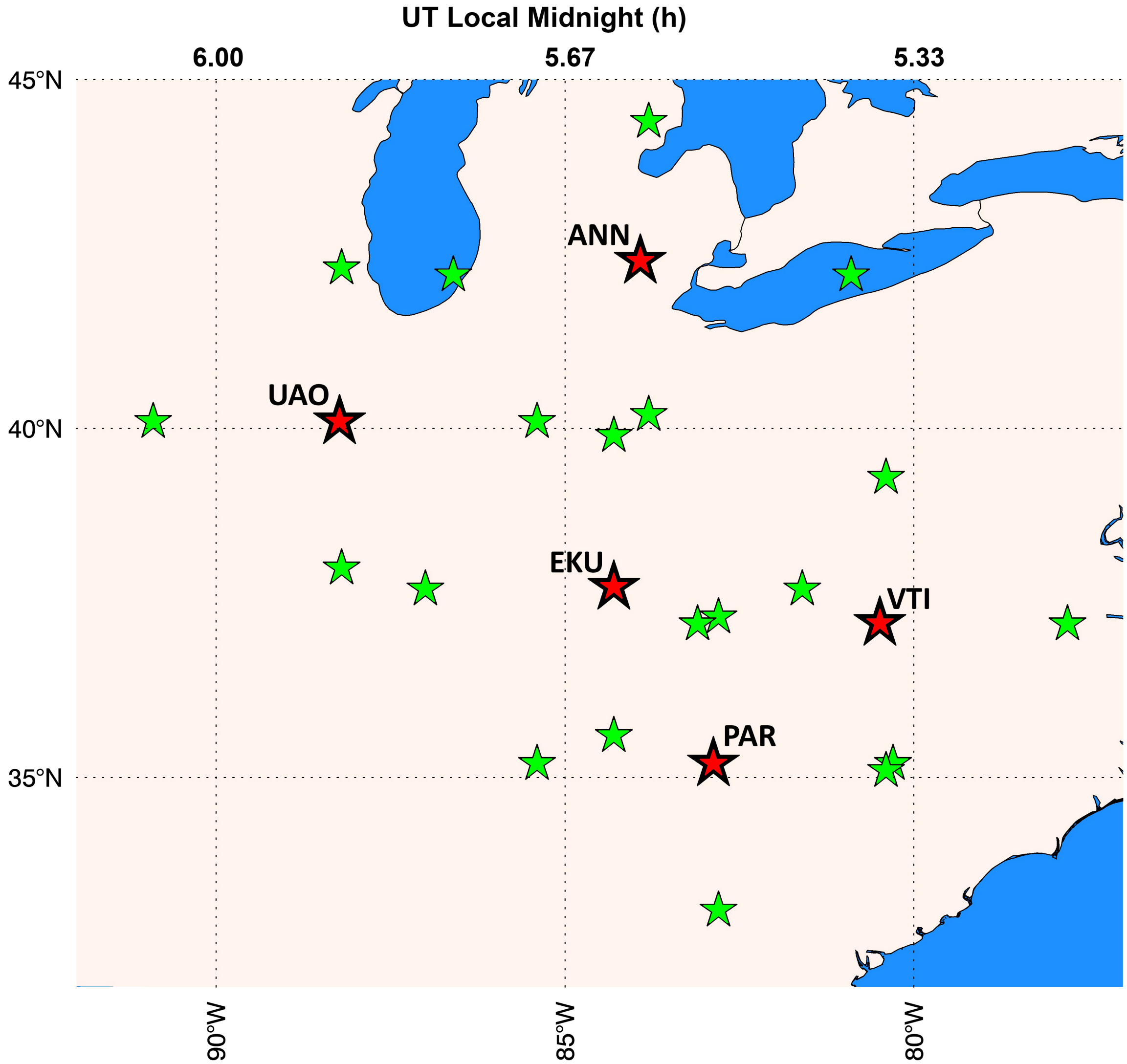

Figure 2.1: NATION Cardinal Mode FPI observing configuration. Red and green stars mark the NATION site position and the measurement locations, respectively, for north, east, south, and west directions assuming a 630-nm 250 km altitude. Red stars also represent the positions of the zenith measurement. The top axis represent the local midnight in universal time.

typically represents an improvement in the number of measurement cycles per hour (from 2.5 to 4.5 cycles per hour) maintaining a fairly constant signal to noise ratio.

2.3 Harmonic background removal model

The normal temporal pattern of nighttime thermosphere temperatures is a cooling trend after sunset with a reversal to a warming trend starting several hours before dawn. Hence, in the absence of the MTM peak(s) one would expect the nighttime temporal behavior to be similar to a U-shaped temperature background featuring a valley. Because the breadth of the MTM structure is typically two hours in local time, the determination of the MTM peak amplitude needs to account for a possible background curvature with local time. The method of determining the MTM amplitude that relies upon connecting the local minima with a straight line (Linear fitting approach) will underestimate the amplitude in most cases. Figure 2.2 illustrates this method, which only uses the two local minima connected by red lines for each MTM feature.

In this paper a new approach to estimating the MTM amplitude is introduced that uses all of the temperature data instead of just the turning points of the temperature series that mark the starting (i.e., before the MTM peak) and ending (i.e., after the peak) points of the MTM peak profile (see Figure 2.2 for differences between approaches). This procedure uses a model in which the temperature data including the MTM is assumed to be the superposition of a background thermal variation and a Gaussian disturbance attributed to the MTM peak. This generally is a good approximation, given that small-scale temperature fluctuations are not related to the MTM. By first filtering the temperature data to remove the MTM structure, the overall nighttime background temperature variation is determined and subtracted from the observed set of FPI temperatures. This technique allows the MTM peak to be extracted as a set of temperature residuals relative to the background variation.

This technique is similar to the algorithm published by Martinis et al. (2013) for analysis of radar ion temperature data with an adaptation for the shorter time span of the FPI measurements. The idea is to manually ignore the MTM peaks (by excluding from the data set the temperature data from the local minimum before the MTM peak to the local minimum after the MTM peak) and fit a harmonic model to the remaining temperature data (without the MTM peaks) to determine the background thermal variation that will be subtracted from the data. It is assumed that the model fit to the thermal variation can be constructed with the combination of 8 hr, 12 hr and 24 hr harmonics. The residual values are then searched for the MTM peak by fitting a Gaussian profile (equation 2.4.1). The function used for the harmonic background removal model is given by

$$T_{model}(LT) = a_0 + \sum_{i=1}^{3} a_i cos\left(\frac{2\pi\,(LT - b_i)}{\tau_i}\right); \tau_i[h] = [8, 12, 24], \qquad (2.1)$$

where a_0 is the thermal background average, a_i is the amplitude, b_i is the phase, and the τ_i is the period of each oscillation. An example of the differences in the results found using both approaches (linear fitting and the harmonic thermal background removal) can be seen in Figure 2.2. In this figure the differences are $\sim 6\%$ (125.6 K vs 118.4 K, and average difference of 6.6 K) for the primary MTM (around 03:00 LT) and $\sim 33\%$ (140.4 K vs 93.5 K, with the average difference of 27.3 K) for the secondary MTM near 21:00 LT. Figure 2.3 also shows this technique applied to the monthly climatology plot of MTM events in the months of February 2012, 2013, 2014 and 2015. This figure displays both MTM features with amplitudes well above the uncertainty of the measurements, there represented by the vertical error bar.

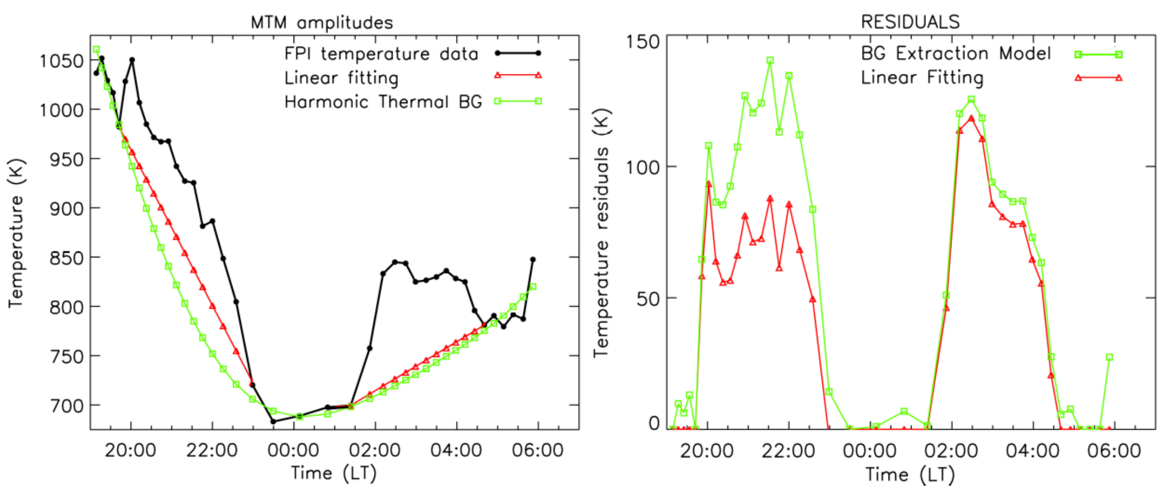

Figure 2.2: (a) An example of the double MTM structure (black points) and two continuum thermal backgrounds assumed (linear and harmonic) for estimating the MTM amplitude (data from for August 31, 2013). (b) Difference plots determined by subtractions of the background linear fit (red) and the harmonic fit (green) from the data points, respectively.

2.4 Results

The analysis of 846 nights was undertaken to study the frequency of the MTM and its double feature. These data came as a result of nearly 4 years (2012-2015) of observations by the

NATION network in the eastern US. To find the MTM peak with accuracy it was necessary to use the harmonic background removal technique which allowed for the detection of the double MTM structure and the set of resulting residuals in the climatology study and the temperature interpolation case study. These results were combined with the method of inversion Harding et al. (2015) to create 2D temperature maps that were plotted together with a superposition of the measured wind field.

In regards to quality control of the data, the data showing any nonphysical wind speeds and temperatures, temperature and wind uncertainties larger than 50 K and 25 m/s, respectively are not considered. The data is also filtered to remove periods of heavy cloud coverage. Also, note that when making reference to time, Local Time (LT) is the same as Solar Local Time in the results displayed in figures 2.2, 2.3, 2.4, 2.8 and 2.9.

2.4.1 MTM double peak structure

To further investigate the seasonal variability of the MTM peak structure, the same harmonic background removal technique was applied to the monthly-averaged temperature climatology. The monthly-averaged climatology for the MTM results from the collection of all the nights with the presence of the MTM peak, averaged in half-hour time bins for a particular month. The temperature residuals, derived by subtracting the harmonic background model from the temperature data are displayed in Figure 2.4. The same figure shows the harmonic fitting for the peak times and the Gaussian fit for each peak as described by equation 2.4.1, where A_0 is the amplitude, A_1 is the LT of the center and A_2 is the width of each peak. It is evident that there is an annual behavior seen in the timing of the MTM with the peak times being earlier in summer and later in winter months.

$$T_{residual}(LT) = A_0 \exp\left(\frac{-z^2}{2}\right), z(LT) = \frac{LT - A_1}{A_2}. \qquad (2.2)$$

The averaged temporal difference between the two curves (primary MTM peak time fittings minus secondary MTM peak time fittings) is 4:28±00:19 h. This result is consistent to what was found in the modeling work by Akmaev et al. (2009) and observed by Faivre et al. (2006). The averaged amplitudes for the primary and secondary MTM peaks are found to be 47 ±24 K and 24±14 K, respectively. The coefficients of the Gaussian fits for each MTM peak and each month of the averaged MTM nights for PARI can be seen in Figure 2.5. These coefficients for the Gaussian

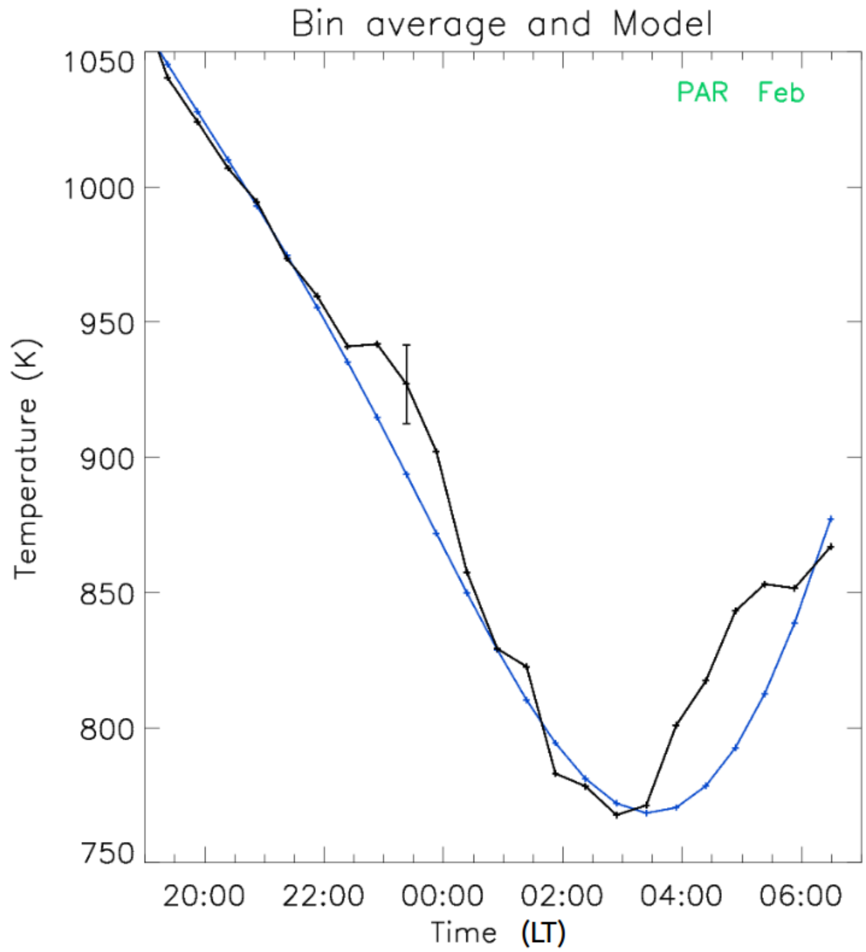

Figure 2.3: Monthly climatology plot of the temperature data for nights with MTM events in the months of February 2012, 2013, 2014 and 2015. The blue curve represents the thermal background and the black curve is the averaged data for PARI. The vertical error bar is a representative depiction of the averaged measurement errors.

fit are shown in equation 2.4.1.

The MTM is a tidal wave generated near the geographic equator and propagating northwestward (northern hemisphere) and southwestward (southern hemisphere) as a wake wave Akmaev et al. (2009). That means that the primary and the secondary MTM peaks (generated near the equator around midnight and before twilight, respectively) will travel towards the poles and appear at different times relative to the latitude. The NATION network placement and latitude range allows both MTM peaks to be detected, especially for winter observations with its longer periods of darkness. The early night MTM (secondary MTM) makes its appearance in the southernmost NATION site near 23:00 LT and the primary MTM near 04:00 LT.

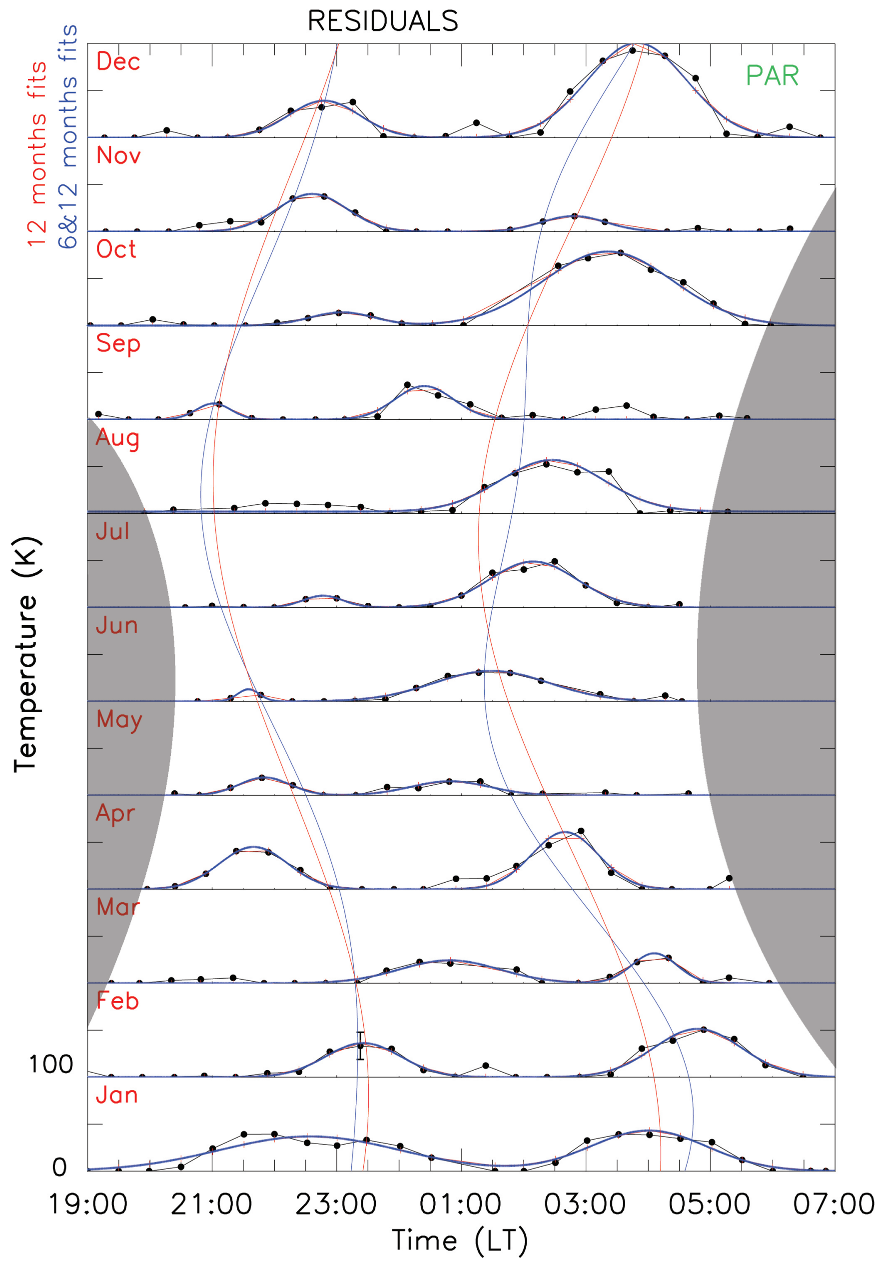

Figure 2.4: Residuals resulting from the harmonic background removal technique (real data minus the background model from equation 2.1) and the monthly averages similar to Figure 2.3. The annual (red) and annual and semiannual (blue) oscillations fittings are plotted in the vertical orientation. Shaded areas represent day time periods. The black dots connected by lines are the temperature residuals and horizontal blue curves are the least squares Gaussian fit for each of the MTM features (as described in equation 2.4.1).

The other factor contributing to achieving detection of both MTM peaks is the fact that in mid-latitudes the nights are longer during the winter, allowing for measurements as early as 17:00

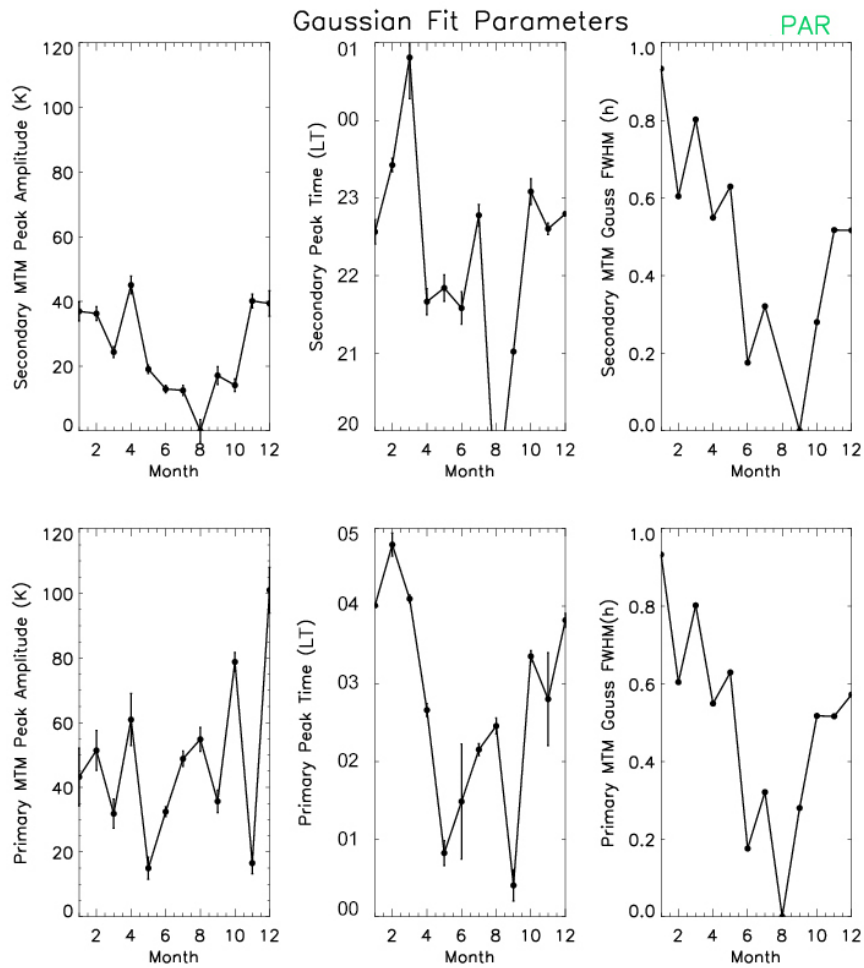

Figure 2.5: Coefficients for Gaussian fitting in Figure 2.4 and their respective deviations.

LT. However, during the summer months, when the nights are shorter, the bright continuum twilight background reduces the detectability of the secondary peak, as can be seen by inspection Figure 2.4.

2.4.2 Background extracted temperature interpolation

Figure 2.1 presents a map of the NATION cardinal mode measurement positions, showing that the NATION network offers a broad latitudinal and longitudinal coverage (about 1200x1200 km) of the Midwest continental region of the United States. Consequently, the possible analysis of the MTM peak and its large spatial structural characteristics, such as its direction of propagation and velocity, is expanded significantly as compared with the spatial extent observed by a single FPI observatory. This examination of the MTM spatial structure becomes more difficult if done using only the raw temperature data, where no emphasis is given to the MTM peaks, since the MTM thermal variation relative to the nighttime thermal variation represents a small fraction of the thermal background.

It is in this regard that the application of the harmonic thermal background removal procedure described by equation 2.1 becomes important. As shown above, the identification of the double MTM peak profile becomes more clear following the removal of the thermal background. Fitting a Gaussian to each of the two MTM peaks in the residual values yields accurate estimates for the amplitude and the peak time of occurrence. This procedure is also necessary in extracting the MTM peak structures for cases where smaller scale oscillations, such as gravity wave activity, might be present in the data.

The large number of measurement positions in the NATION network allows for the detection of both MTM peaks (when present), in an inversion analysis similar to what was done by Harding et al. (2015) for the Eastern Brazilian and the NATION FPI networks for the winds. The authors used inversion theory to build an algorithm capable of estimating the wind fields. In this work, a modified version of this approach is applied to the temperature residuals to generate a temperature field in a manner similar to what was described by Harding et al. (2015) to calculate a horizontal wind field. This algorithm searches for the smoothest horizontal wind and temperature fields that fit the data within the data uncertainty. Figure 2.6 shows the result of the application of this technique for the night of December 28, 2013. It shows the appearance of both MTM structures and the corresponding change in the horizontal wind field behavior as a function of local time.

Figure 2.6 results of this algorithm applied to the temperature residuals and winds. The propagation of the MTM is clearly seen to cross the NATION field of view from 03:00 UT to 06:00 UT and 08:00 UT to 09:30 UT (UT used here due to the spatial coverage of the network, local midnight is approximately at 05:30 UT in the middle of the network). Both MTM peaks, appear with winds in the southeastward direction and temperature maximums propagating predominantly to the westward and northwestward directions, respectively. However, the winds around the time of the secondary peak are faster and in the east-southeastward direction, while the primary MTM peak is associated with a slower wind field in the south-southeastward direction. This behavior is typical of the reversal of the winds occurring before the passage of the primary MTM peak Akmaev et al. (2009).

Further evidence for the double-peaked MTM structure comes from calculating the diver-

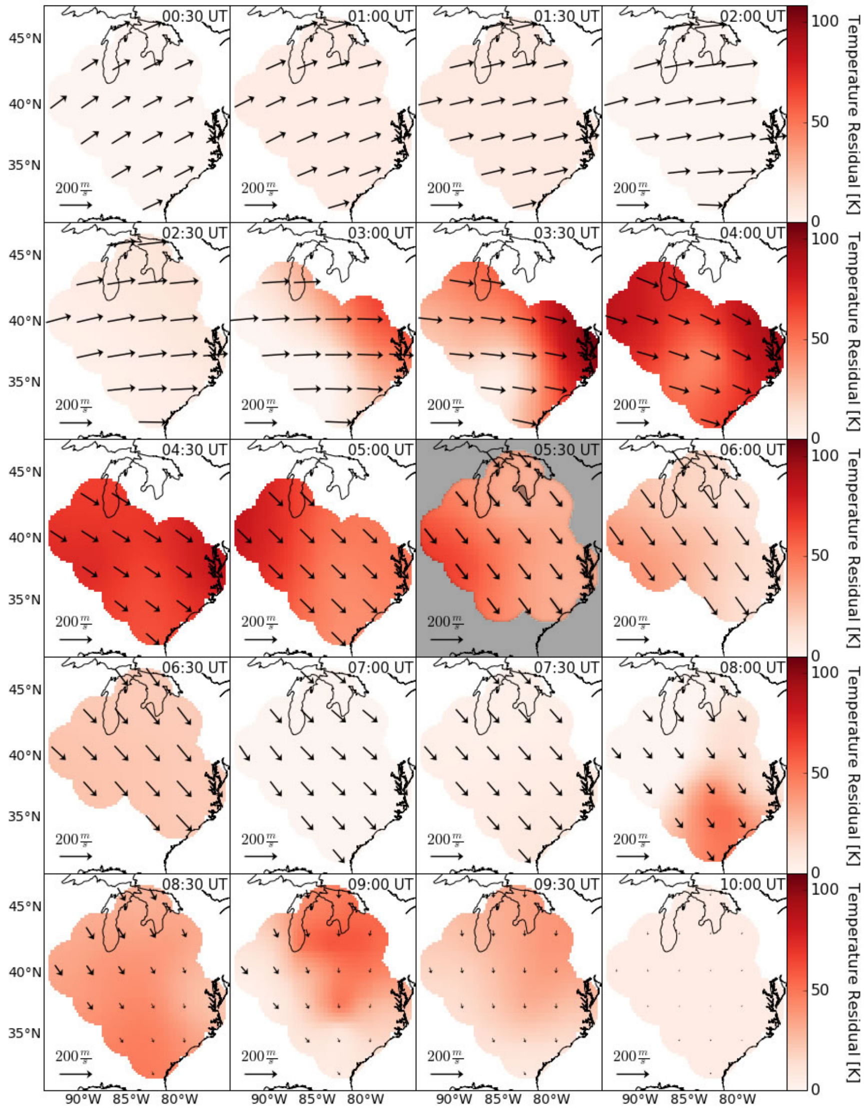

Figure 2.6: 2D temperature maps generated from the measurements with the harmonic thermal background removal technique for the night of December 28$^{\text{th}}$ 2013. Two clear MTM events are seen as suggested by the modeling work of Akmaev et al. (2009). The gray-shaded map represents the approximate local midnight in the middle of the NATION network.

gence of the wind field. The wind field is estimated at a 5-minute cadence for the whole night over NATION at each time step. For every grid point, the divergence is calculated by comparing the residual value with its neighboring grid points, and the divergence is averaged over the entire grid. Figure 2.7 shows two periods of strong convergence at 04:00 UT and 08:30 UT, coincident with the peaks in the temperature seen in Figure 2.6. Each period of convergence is preceded by a period of divergence.

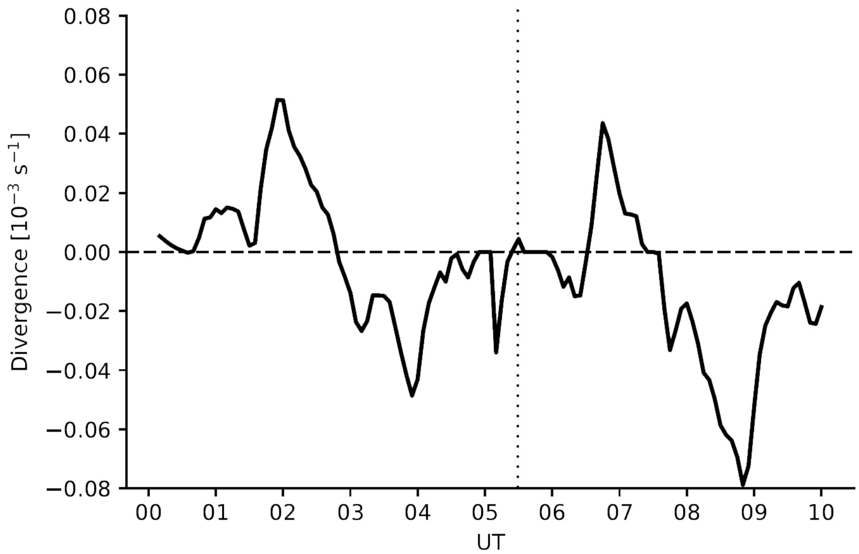

Figure 2.7: Average divergence calculated for the wind field present in Figure 2.6. Period of divergence followed by convergence that coincide with both MTM peaks. The vertical line represents the local midnight in average longitude of the NATION network.

The signature of the winds provides independent evidence for the occurrence at the mid-latitude MTM, as the convergence at 04:00 UT and 08:30 UT correspond to the peaks in the temperatures, as would be expected from adiabatic heating. The divergence pattern displayed in Figure 2.7 is mainly associated with the reversal of the meridional winds, resulting of the upward propagation of the tidal waves, as discussed by Akmaev (2011). The preceding period of divergence may be associated with the pressure bulge front Herrero et al. (1985), but this cannot be conclusively explained without a larger number of observed nights with full coverage and perhaps measurements of pressure or vertical winds.

2.4.3 Statistics

Before describing the results of the statistical analysis of the mid-latitude MTM peak amplitude and time of occurrence based upon NATION data, we examine the definition of the MTM peak used in this analysis. The MTM peak structure is typically represented by primary and secondary peaks with the primary peak occurring later with a larger amplitude. The time window of measurements for the NATION network would typically be in the range of 19:00-07:00 LT. We define the MTM peak to be a significant increase in the temperature measurements compared to the thermal background. A threshold of 50 K or the measurement uncertainty (largest between the two criteria) is used to define such an increase as a MTM peak with the conditions that the MTM enhancement starts after 20:00 LT, continues for more than one hour, propagates northward, and appears in at least 3 different measurement positions. That defines a **MTM category** used to collect the temperature increase events as well as the timing of the increase. The MTM-related brightness increase in the 630-nm intensities imposes another constraint. For an event to be in this MTM category, a brightness enhancement must also be evident in the FPI's 630-nm intensities (related to the brightness wave phenomenon discussed by Colerico et al. (2006)). The MTM signature is also much larger in amplitude than the small-scale temperature fluctuations induced by gravity-wave activity and repeatable (each MTM peak happening in similar times from one night to the next).

The other two categories in the statistical analysis are the **NO MTM category** (clear absence of a defined maximum) and the **inconclusive category** (all nights with measurements from more than 3 stations that do not bring enough information to be able to categorize them neither as a MTM or NO MTM nights; typically nights with full moon or nights with long periods of cloud coverage). Out of a total number of 846 analyzed nights, 44% were inconclusive, 43% had no MTM peaks and 13% had the presence of the MTM in the temperature data.

Figure 2.8 represents an example of a NO MTM night in a plot of the temperature data with the points shifted in latitude depending upon the latitude at the 250-km pierce point for each measurement direction. In the case of figuresMTM 2.8 and 2.9, the east, west, and zenith measurements are averaged within a 30 minute bin. These measurements have the same latitude and the longitude-related differences are averaged out since east and west positions are equally spaced relative to the zenith. The measurements for the north and south directions (indicated for each color/site as the top and bottom lines, respectively) are displayed in figuresMTM 2.8 and 2.9. These results do not have any bin averaging applied. Figure 2.9 displays an example of a MTM night that also shows the appearance of a double MTM structure feature.

Looking at the results of the statistical analysis with regard to the MTM amplitude (maximum peak), the MTM phenomenon shows no clear seasonal dependence for the range of latitudes that NATION measurements cover. This behavior can be observed with Figure 2.10 (histogram with number of nights vs MTM amplitude). The number of MTM nights for summer is slightly larger than the results seen for the other seasons, and any differences are negligible given the uncertainty in the analysis. Figure 2.10 also shows the the distribution of amplitudes, with the (80,100] bin being the one with the largest number of occurrences (39 nights), corroborating the result observed

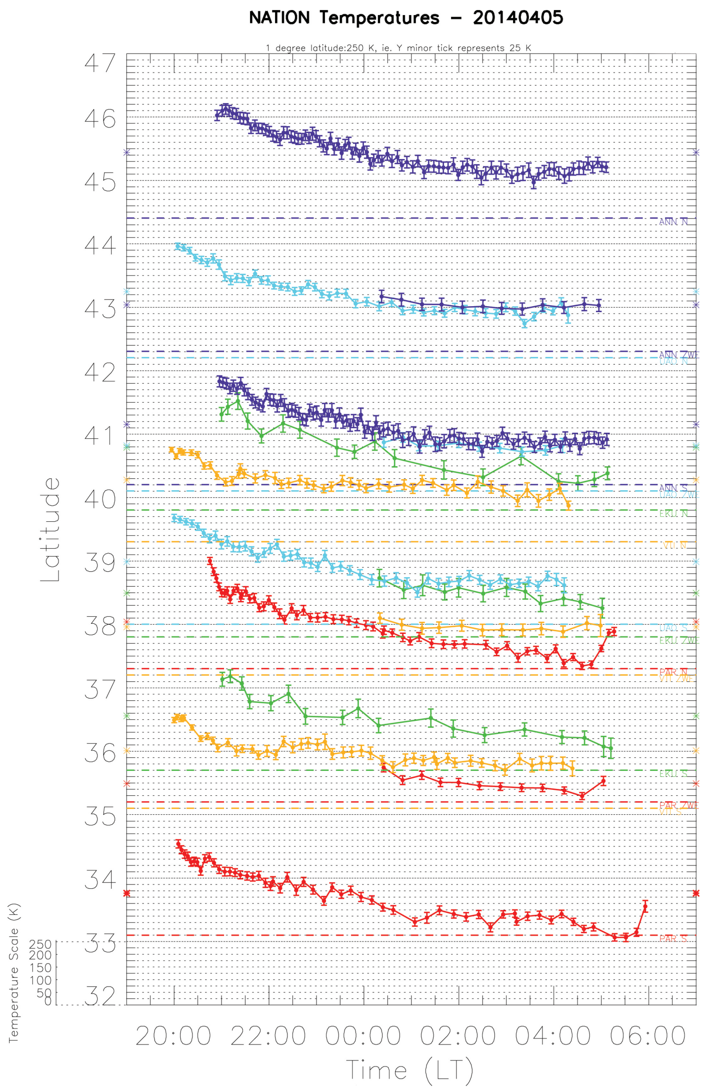

Figure 2.8: NATION latitudinal temperature distribution graph for April 5, 2014; illustrating the lack of the double or single MTM structure. Each color represents the FPI temperature results of a NATION station with a set of 3 temperature lines (north, zonal, south directions). From bottom to top, the line colors of red, orange, green, blue, and purple represent results for the PAR, VTI, EKU, UAO, ANN NATION sites, respectively. The north, zonal, and south measurements are shifted to their respective latitudes, and the horizontal dashed baseline represents 800 K for that particular measurement. The magnitude of one degree latitude corresponds to a 250 K difference. The asterisks on the left and right vertical axises represent the temperature averages for each latitude set of measurements.

at Table 2.1, which shows the MTM amplitude being 90.6 ± 24.9 K.

Figure 2.10 can also be used to show the MTM distribution with respect to the seasons. The seasonality of the MTM occurrence for the mid-latitude section is found to be slightly larger for summer (with 27%) compared to the other seasons, with spring (with 18%) showing the lowest

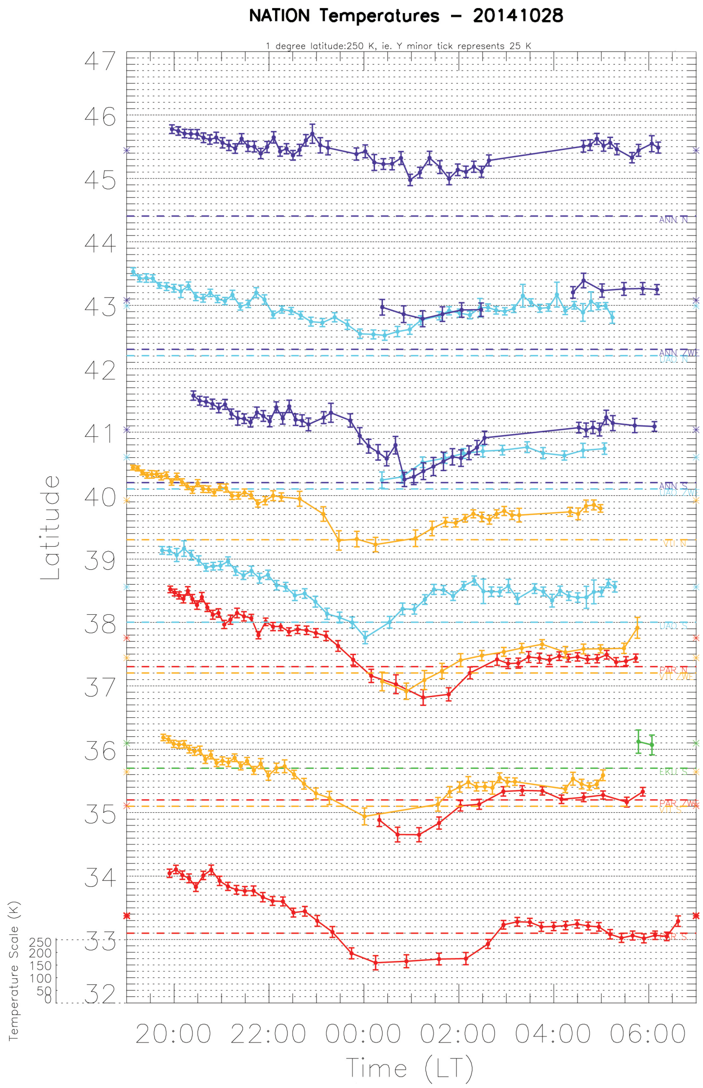

Figure 2.9: Temperature distribution graph similar in style to Figure 2.8, for August 31, 2013. These results illustrate the presence of the double MTM structure. The secondary peak near 22:00 LT in the southernmost measurement and the primary MTM peak near 03:00 LT.

frequency of the phenomenon occurrence. That behavior is consistent with modeling results and observations by Akmaev et al. (2009) and Martinis et al. (2013) respectively.

For NATION mid-latitudes the MTM phenomena appear to be quite active in the FPI data. As shown in Figure 2.9, the MTM double peak structure appearing at all sites within the NATION network, meaning that the MTM is seen as far as the most northern measurement by ANN North which is located at 44.4°N and -83.8°W. It indicates that within the NATION latitudinal span the MTM phenomenon is penetrating further toward the pole than the latitude of the southernmost

Table 2.1: Information about the MTM perturbation times (times for the beginning of the first peak and ending of the second) and maximum amplitude for all the stations.

	Starting time (LT)	Ending time (LT)	Max amplitude (K)
Average	21.8	2.4	90.6
Standard deviation	1.3	1.5	24.9

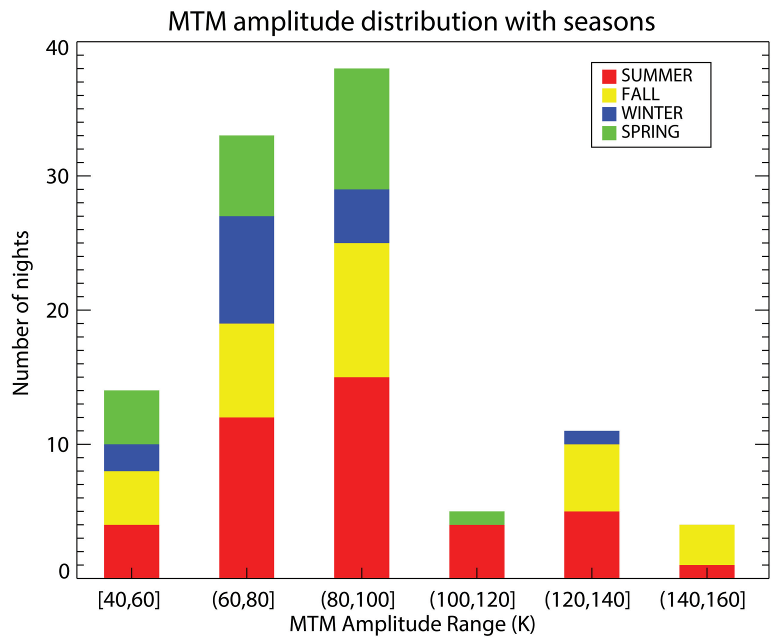

Figure 2.10: MTM statistical distribution with regard to season and maximum amplitude for all the stations. The more frequent MTM amplitudes are found in the (60,80] and (80,100] ranges with 33 and 39 nights, respectively. MTM events with large amplitudes exceeding 120 K are occasionally seen (15 nights).

appearance reported by Colerico et al. (2006) for the Southern American region.

2.5 Discussion

The primary results of this work show the frequent detection of the MTM as a double peak phenomenon for the NATION network at mid-latitudes and within the American longitudinal sector. The reason that the secondary MTM peak is not generally seen at low latitudes is because its amplitude is weak and its occurrence would normally take place during the evening twilight where detection is more difficult. However, the time it takes the secondary peak to propagate to midlatitudes proves enough temporal separation from the twilight to make it detectable. Furthermore, the results are consistent with what is shown by Akmaev et al. (2009); Akmaev (2011) and Faivre et al. (2006). The application of the NATION network to the study of the MTM phenomenon produced strong evidence of the MTM amplitude variability with northwestward propagation, which is the typical direction of propagation shown in Figure 2.6, and previously observed near 39.0° for the southern hemisphere Colerico and Mendillo (2002); Colerico et al. (2006), this study confirms the presence of the MTM as far north as ANN North corresponding to 44.4° N.

From a latitudinal standpoint, the MTM structure is much the same to what is observed in lower latitudes in regard to its direction of propagation. However the amplitude is generally weaker and it appears with different morphology if compared to the analysis made for MTM events seen in the equatorial region Figueiredo et al. (2017); Gong et al. (2016). The amplitude variation of the MTM as it propagates both poleward and westward may be mostly due to the difference in phases contributing by the superposition of the tidal modes Akmaev et al. (2009); Akmaev (2011), which changes the result of the tidal wave superposition in the mid-latitude region. Like any phenomenon in the upper atmosphere, the MTM is also subjected to partial or total dissipation processes. It will be important in future work to gain a better understanding on what are the contributing factors causing the MTM to have such variation (with respect to both time and space), possibly by examining TEC content and ionosonde data to search for possible correlation between the MTM peak amplitude and the F-region plasma density.

It is understood that the formation of the mid-latitude MTM tidal wave is more influenced by higher-order tidal modes Akmaev et al. (2009). Thus, the MTM peak structure does not have amplitudes as large as that found for the equatorial region observations. This is perhaps because the tidal forcing is stronger at low latitudes. Part of the reason why it was possible to observe the MTM peaks in the mid-latitude region was also the use of the harmonic background removal model. Its application enabled a more accurate investigation of the amplitude of the MTM and the development of the 2D temperature residual maps for the NATION network. It was necessary to develop the harmonic thermal background removal technique in order to trace the MTM and avoid any underestimations as well as enable to detect such low amplitudes when compared to the thermal background. This approach estimates the MTM peak amplitude, with a difference of as much as 33% when comparing it to the result of the linear fitting approach (Figure 2.2).

The harmonic background removal model and the coverage of measurements from the NATION network enabled the imaging of the MTM feature using the process of the 2D interpolation of the phenomenon. Figure 2.6 shows this result for the night of December 28, 2013. In this case the MTM can be detected with the presence of its double peak structure. The first peak, around 04:30 UT, has a strong westward component when compared with the primary MTM peak's northwestward behavior. It is also, for that particular night, longer lasting (about twice as long as the primary MTM) and with faster southeastern winds. The propagation speed of this peak is $\sim 120ms^{-1}$.

The second MTM (primary), around 8 UT, has a northwestward propagation behavior with the northward component more pronounced. The wind field present in Figure 2.6 suggests a flow towards the MTM peak, as the earlier peak, typical of the pressure bulge responsible for the generation of the MTM peaks, though with weaker winds. Another interesting result is the velocity of the primary MTM to be of $\sim 240ms^{-1}$. The example associated with this night indicates the primary MTM moves faster in the background of weaker winds. Unfortunately similar analysis can only be done with the presence of clear skies in a vast area of the network, indicating that such analysis would be more feasible if done in the a cloudless region such as the US western region.

With regard to its seasonality, the primary MTM peak shows a clear annual/semi-annual behavior in amplitude appearing more often during summer with 27% (around 9% more than spring), which can be seen in Figure 2.10. That behavior also appears in the phase of both MTM peaks as well. Both peaks exhibit annual/semi-annual behavior as can be seen from Figure 2.4. From the same figure, the time difference between the two vertical fittings is 4:28$\pm$00:19 hours, consistent with results from the WAM model Akmaev et al. (2009). From the same figure we have 47.6$\pm$24.8 K and 24.9$\pm$14.3 K for the average MTM amplitudes for the PARI site. Along with these averages we have the average of the maximum amplitude 90.6$\pm$24.9 K (accounting for all the sites), starting time of 22:15$\pm$01:19 LT and ending time of 02:53$\pm$01:30 LT. No particular trend is found for the MTM in regard to its amplitude as can be seen in Figure 2.10.

2.6 Conclusions

Previous work on the MTM phenomenon has concentrated upon the equatorial and low latitude results, and the question of the extent that the MTM phenomenology reached into higher latitudes had not been examined carefully. One reason for this might be attributed to the limitation associated with the application of a Fabry-Perot interferometer that has only a photomultipler detector and is observing only one interference order. Such instruments do not have sufficient sensitivity to observe the weak 630-nm nightglow with the necessary accuracy and observing cadence to be able to detect the mid-latitude MTM phenomenon with confidence. Thus, it is likely for this reason that previous work associated with mid-latitude FPI observations did not report the successful detection of this phenomenon Hernandez and Roble (1976); Herrero and Spencer (1982). Thus, the results presented in this paper illustrate how the new technology of FPI instrumentation featuring observations of multiple interference orders and the much higher quantum efficiency of the bare CCD detector has resulted in temperature observations with much improved quality regarding the reduction of observing errors and the increase in the number of samples per hour.

With the results reported in this paper, the MTM signature for the mid-latitude region shows a strong indication for the appearance of a double peak structure rather than a single peak as characteristic of the MTM results seen for lower latitudes. As stated before, these new results are consistent with the double MTM peak results found in the modeling work reported by Akmaev et al. (2009); Akmaev (2011) and Faivre et al. (2006). We also note that the application of a more suitable analysis technique would improve the accuracy of the MTM peak amplitude estimations Hickey et al. (2014); Ruan et al. (2013); Azeem et al. (2012).

By making a month to month binned average of the MTM nights and using the harmonic background removal model, the variation of the MTM characteristics with season become evident, as shown in Figure 2.4. This climatology displays the fact that the extent of the NATION network coverage allows for the detection of both peaks. As the MTM double peak structure travels northward from the equator, both MTM peaks become observable because of a systematic latitudinal-dependent phase shift of the MTM peak occurence times to later local times with higher latitudes. Moreover, the longer winter nights help to make possible the observation of the MTM double peak structure.

The application of the harmonic background removal model for the night of Dec 28th 2013 shows the 2D behavior of the MTM. The wake wave behavior of the MTM is well displayed in Figure 2.6. It is also clear that the secondary and primary MTM peaks cross the NATION network moving in somewhat different directions (northwest-west to northwest-north).

In regard to its general behavior, the mid-latitude MTM structure develops more often during the summer months (as shown in Figure 2.10). However, the secondary maxima is more prominent during the winter months as shown in Figure 2.4. It is difficult to determine if that behavior is due to the nature of the phenomenon or due to the difference between the duration of summer and winter nights. Nevertheless, the amplitude of the secondary MTM peak is stronger in the winter months as illustrated by the results shown in Figure 2.5 (top left graph).

Further work would be interesting to carry out for the same latitudinal region, but with the NATION sites relocated to the southwestern United States. This relocation would provide better quality data year-round due to the clear skies found in this dryer region, which would improve the 2D analysis of the MTM double peak structure in all seasons. Application of models such as general circulation models (WAM and TIEGCM) would help assess the similarity between the results from NATION and these model predictions. This analysis should help to understand the underlying day-to-day variability of the MTM double peak structure. Future work should also include a thorough investigation of the OH behavior, because the small OH contamination that exists for weak 630-nm airglow intensities may lead to a time-dependent error in the temperature measurements that could affect the background fit.

Chapter 3

In-situ observations of neutral shear instability in the statically stable high-latitude mesosphere and lower thermosphere during quiet geomagnetic conditions

Rafael L.A. Mesquita[1], Miguel F. Larsen[1], Irfan Azeem[2], Michael H. Stevens[3], Bifford P. Williams[4], Richard L. Collins[5], and Jintai Li[5,1].

[1] Physics and Astronomy Department, Clemson University, Clemson, South Carolina, USA.

[2] Atmospheric & Space Technology Research Associates, LLC, Louisville, Colorado, USA.

[3] Space Science Division, Naval Research Laboratory, Washington, District of Columbia, USA.

[4] GATS Inc., Boulder Division, Boulder, Colorado, USA.

[5] Geophysical Institute, University of Alaska, Fairbanks, Alaska, USA.

Published as:

Mesquita, R. L. A., Larsen, M. F., Azeem, I., Stevens, M. H., Williams, B. P., & Collins, R. L., et al. (2020). In situ observations of neutral shear instability in the statically stable high-latitude mesosphere and lower thermosphere during quiet geomagnetic conditions. Journal of Geophysical Research: Space Physics, 125, e2020JA027972. `https://doi.org/10.1029/2020JA027972`.

Abstract

Though the Kelvin-Helmholtz instability (KHI) has been extensively observed in the mesosphere, where breaking gravity waves produce the conditions required for instability, little has been done to describe quantitatively this phenomenon in detail in the mesopause and lower thermosphere, which are associated with the long-lived shears at the base of this statically stable region. Using trimethylaluminum (TMA) released from two sounding rockets launched on January 26, 2018, from Poker Flat Research Range in Alaska, the KHI was observed in great detail above 100 km. Two sets of rocket measurements, made 30 minutes apart, show strong winds (predominantly meridional and up to 150 ms^{-1}) and large total shears (90 ms^{-1}km^{-1}). The geomagnetic activity was low in the hours before the launches, confirming that the enhanced shears that triggered the KHI are not a result of the E-region auroral jets. The four-dimensional (three-dimensional plus time) estimation of KHI billow features resulted in a wavelength, eddy diameter, and vertical length scale of 9.8 km, 5.2 km, and 3.8 km, respectively, centered at 102km altitude. The vertical and horizontal root-mean-square velocities measured 29.2 ms^{-1} and 42.5 ms^{-1}, respectively. Although the wind structure persisted, the KHI structure changed significantly with time over the interval separating the two launches, being present only in the first launch. The rapid dispersal of the TMA cloud in the instability region was evidence of enhanced turbulent mixing. The analysis of the Reynolds and Froude numbers (Re=7.2×10^3 and Fr=0.29, respectively) illustrate the presence of turbulence and weak stratification of the flow.

3.1 Introduction

Dynamical instabilities are known to play an important role in producing enhanced mixing, in redistributing energy and momentum, and in producing transport of various minor chemical species. The mesosphere in particular is frequently subject to instabilities associated with the spectrum of gravity waves that propagates through that region. The mean reduced static stability associated with the negative lapse rate of the layer makes it easier to meet the conditions required for shear instability of the Kelvin-Helmholtz KHI type, although other instabilities may play a role as well. The shear instabilities in the mesosphere are mostly short-lived transient phenomena produced either when gravity waves begin to break or when the superposition of the gravity-wave-induced vertical temperature variation and the background negative lapse rate lead to reduced static stability, requiring only a modest shear to become dynamically unstable. Examples of instability structure observed in the mesosphere, as well as discussions of the relevant dynamics, can be found in articles by Bishop et al. (2004), Hecht (2005), Pfrommer et al. (2009), and Baumgarten and Fritts (2014), among others.

In the transition across the mesopause and the lower thermosphere, where an isothermal or positive lapse rate develops, the conditions are inherently more stable, at least in principle inhibiting dynamical instabilities, but Larsen (2002) showed that large shears, close to the Richardson number (Ri) threshold required for instability ($Ri < 0.25$), are a frequent and persistent feature of that altitude range with mean shears maximizing in the 95 to 105km altitude range. Based on TIME-GCM model results, Liu (2007) showed that the observed shears in that altitude range follow an envelope consistent with the maximum shear for the Richardson number threshold condition. Liu (2017) examined the wave forcing that drives these long-lived shears using the NCAR Whole Atmosphere Community Climate Model (WACCM) and analyzed the effects on diffusion and tracer transport of the large shears. Further discussion of the dynamics and implications of these long-lived shears can also be found in that article.

Direct observations of shear instabilities in that region are difficult to obtain. Measurements with the most sensitive sodium resonance lidars, for example, often extend only to the altitude where the large persistent shears occur (Bishop et al., 2004, e.g.,). Sensitive incoherent scatter radar measurements, such as those made with the Arecibo Observatory 430MHz radar, can be used to map out the electron density contours with height and time resolution of a few hundred meters and a few minutes, respectively, sufficient to show the billow structure characteristic of the KHI. Larsen (2000a) argued that the billow structure observed with incoherent scatter radars was driven by, and showed direct evidence of, the occurrence of shear instability in the neutrals, resulting in quasi-periodic echo structure within Sporadic E layers, for example. Since the ions are still highly collisional below 105km, the plasma mimics the structure in the neutral background. Neutral shear instability as a driver for plasma structuring and further instability is of interest in itself; but a notable conclusion of the study was that, since the plasma structure is often present for many hours during the night, the large neutral shears and the conditions for neutral instability must also be present in that narrow height range for extended periods. Hysell et al. (2012) extended the Arecibo incoherent scatter radar studies of plasma and neutral instabilities in the 95 to 110km altitude range, measuring temperature and neutral wind profiles over time to show that unstable conditions were persistent and long-lived. The region can also be subject to other types of long-lived instabilities, such as the convective roll instability first discussed by Larsen (2004) and Hurd et al. (2009) in the context of the mesopause/lower thermosphere interface. Mondal et al. (2019) reported lidar observations of "C-type" structure and attributed it to "frozen-in" KHI billows advecting with the background wind, although the time scale of two or more hours for the development of the structures reported by those authors argues for the convective roll instability rather than the KHI, for the reasons discussed in detail by Larsen (2004).

Although less common than the lidar and radar observations, structure attributable to KHI has been seen in tracer trails released from sounding rockets in the mesopause/lower thermosphere region. Larsen et al. (2005) showed the presence of a KHI structure in a trail deployed at a mid-latitude site in Japan during the Sporadic-E Experiment over Kyushu 2 (SEEK-2) campaign, which provided measurements in a region with quasi-periodic Sporadic-E echoes. The trimethylaluminum (TMA) trail showed a set of eight billows between 100 to 115 km altitude. The low apogee trajectory of the rocket provided a nearly horizontal trail in that height range, which helped reveal the KHI billow structures. The horizontal and vertical scale sizes were 5 and 2km, respectively, in a region with large shear that peaked at approximately 90 $\mathrm{ms^{-1}km^{-1}}$ at 102 km altitude. The wind measurements exhibited an unusually strong horizontal variation between the upleg and downleg portion of the trail.

We report here on the observations of winds and KHI overturning structure in measurements made as part of the Super Soaker sounding rocket experiment. The rocket measurements were made during geomagnetically quiet conditions on January 26, 2018, from the launch site at the Poker Flat Research Range (65.13 °N, 147.49 °W) in Alaska. The primary goal of the experiment was to study the effects of an artificial Polar Mesospheric Cloud (PMC) on mesospheric energetics, chemistry, and dynamics. Here we will focus on the wind and instability structure measurements made with two rockets that were launched 37 minutes apart as part of a three-rocket salvo. Both rockets deployed TMA, a chemiluminescent vapor that acts as a tracer of the neutral motions when released in the upper atmosphere (Larsen, 2002, see, e.g.). One of the trails from the first rocket showed clear evidence of Kelvin-Helmholtz-type billow structure and the associated overturning. The measurements presented here show a new aspect of the phenomenon in that the quality of the images used to track the tracer trails was sufficient to obtain the detailed three-dimensional structure of the billows directly by triangulation. The two measurements separated by 37 minutes also show the persistence of the large shears responsible for the instability. The occurrence of this type of overturning instability in the statically-stable conditions associated with the mesopause/lower thermosphere transition region is particularly important because it provides a mechanism for vertical mixing and transport in a region that would otherwise inhibit that type of vertical interchange.

3.2 The Super Soaker launches

The Super Soaker experiment included the launch of three rockets on Jan. 26, 2018, with the goal of studying the effects of an artificially formed Polar Mesospheric Cloud generated by explosively dispersing 220 kg of pure water at 85 km altitude. The first two rockets (UE41.120 and UE41.119) carried TMA tracers and were launched at 14:11:34 UT and 14:48:19 UT, respectively. The third rocket (UE41.122) carrying the water release was launched at 14:49:49 UT. Local time at the launch site is 9 hours behind UT. A coordinated suite of ground-based instruments that included Rayleigh, sodium, and iron lidars, and an Advanced Mesospheric Temperature Mapper were used to observe the response of the atmosphere to the water release (results to be discussed in forthcoming paper). In addition to those instruments, white light imaging cameras were used to track the position of the TMA tracers.

The results presented here focus on data from the first two rockets (UE41.119 and UE41.120), which were launched 37 minutes apart and released the TMA neutral wind tracer between 80 and 160 km altitude on both the upleg and downleg portions of the flight trajectory. Figure 3.1 shows the rocket trajectories and the flight path of a NASA aircraft used as a mobile camera platform flying at an altitude of 8 km. Additional camera sites were located at Poker Flat and Coldfoot, Alaska, also shown in Figure 3.1. The TMA rocket trajectories were spatially closer together and separated from the water release. At 80 km altitude where the rockets began to release TMA, the two rocket trajectories were 5 km apart. Meanwhile at the same altitude, but on the descending portion of the trajectory, the rockets were 34 km apart. At 85 km, where the water was released, the closest horizontal distance between the water rocket and the nearest TMA rocket was 80 km.

The upleg trail from the second rocket is shown in Figure 3.2. TMA is a pyrophoric liquid that ignites on contact with oxygen. At high altitudes in the mesosphere and thermosphere, the low oxygen density produces a slow reaction that generates chemiluminescence that makes the trail visible for 10 minutes or longer, depending on the altitude. Triangulation based on observations

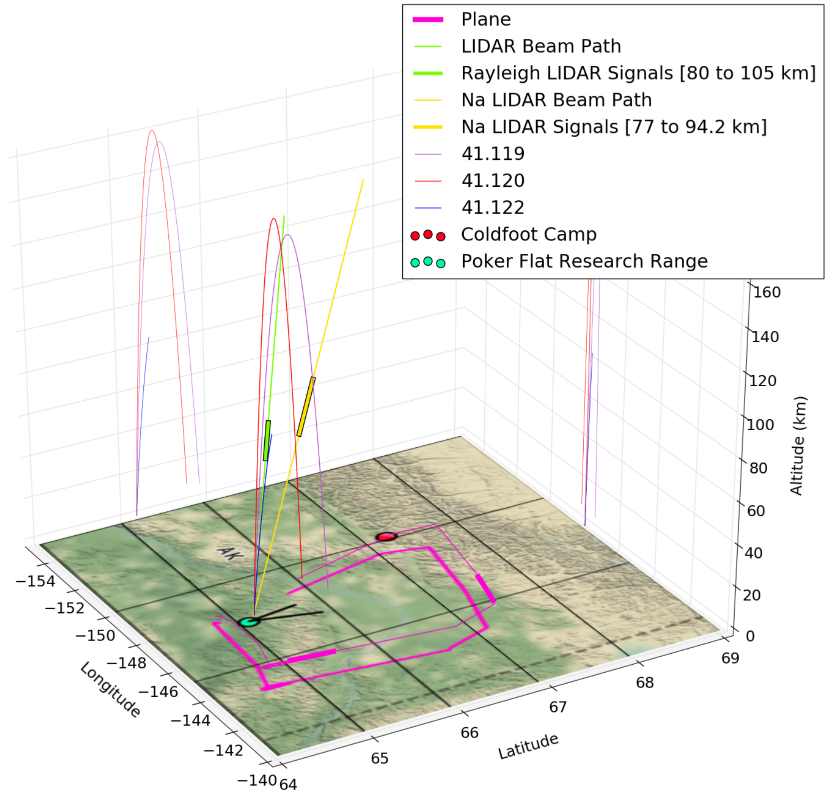

Figure 3.1: Map with the trajectories and camera site locations for the Super Soaker experiment. Rockets UE41.120 and UE41.119 deployed TMA on the upleg and downleg, and rocket UE41.122 carried water that was released near 85 km. The yellow line represents the sodium (Na) lidar beam pointing direction (20° zenith angle, 0° azimuth), with the highlighted region where the temperature measurements had errors smaller than 20 K. The green line represents the Rayleigh lidar beam pointing direction toward zenith. The highlighted region represents the altitude range of the measurements used in this paper.

from two or more spatially-separated sites can be used to obtain the trail position as a function of time and altitude. The implemented manual triangulation procedure used here was described by Larsen et al. (1998), Larsen (2000b), Ingersoll (2008), and Larsen (2013). The advantage of this particular implementation is that the determination of the trail position in the images is partially automated, along with the matching of corresponding positions along the trails in image pairs, which gives higher-resolution results than has been possible with direct manual matching of image features. The primary sources of data in the analysis presented here were Coldfoot and a NASA aircraft flying above any cloud coverage.

Each image captured from one camera site is a two-dimensional representation of the TMA trail. The triangulation technique uses image pairs from different locations at the same time to determine the three-dimensional position of each point in the trail (as represented in Figure 3.2). First, the two-dimensional position of the trail is determined by the coordinate transformation from image pixels to right ascension and declination using the known positions of the stars visible in each image. Right ascension and declination are converted to horizon coordinates, viz., elevation and azimuth for each point in the trail, using the geographic coordinates for the site and the time when the image was taken. Combining image pair data gives the full three-dimensional coordinates of a series of points along the trail. Repeating this process for a series of image pairs produces a time series that can be used to obtain the meridional and zonal winds as a function of height from the motion of the trail. The sources of uncertainty in the triangulation procedure were described by Larsen et al. (1998) and Larsen et al. (2003), and come from the intersection of the two line-of-sight projections and the deviation of the individual measured positions from the linear fitting used to estimate the rate of displacement within a certain altitude bin. A number of studies mentioned values of 3-5 ms^{-1} for the uncertainties in the wind measurements including the paper by Larsen et al. (2003), in which the authors used the same wind estimation technique and algorithm as the one used to estimate the Super Soaker winds. This technique is illustrated in Figure 3.2 where the yellow lines represent the projections from the paired camera site to points in the trail. For example, the projected lines in the Coldfoot image (top left of Figure 3.2) will lead to the position of the aircraft at the moment that image was taken if extended to the left beyond the edge of the image.

The Poker Flat launch site is well within the auroral oval but the Poker Flat magnetometer (Figure 3.3) showed that conditions during the night of the launches, and especially during the observing period, were quiet with very small deflections in all three magnetic field components. The minor activity (<200 nT) near local magnetic midnight ended more than 2 hours prior to the launches. The auroral jets, which create enhanced wind speeds and large shears in the lower E-region and affect the stability of that region (Larsen et al., 1997), did not play a role in generating the enhanced shears analyzed in this manuscript due to the quiet geomagnetic behavior. The vertical line in Figure 3.3 indicates the start of the first TMA upleg trail at 14:16 UT (05:16 LT). The first few images for the second upleg were captured at 14:49 UT (05:49 LT). The Kp index at the time of the launches was 0.3, which is another indicator of the quiet conditions.

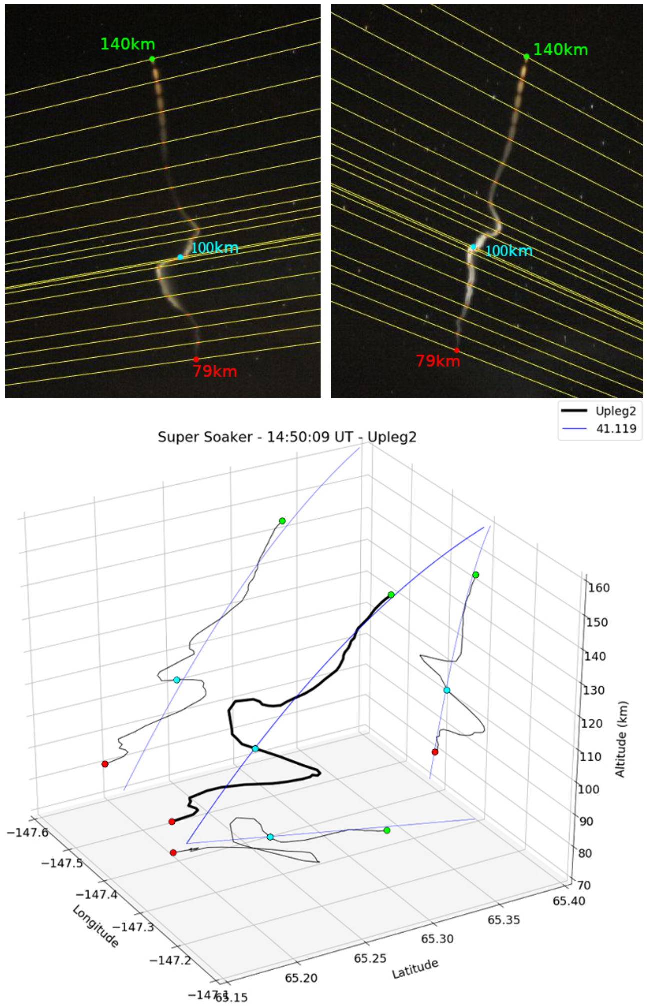

Figure 3.2: (Top panel) Images of the upleg trails from the second rocket (UE41.119) as observed simultaneously from the Coldfoot ground site (left) and the NASA aircraft (right). Yellow lines represent the projections(lines that connect the TMA trail in the picture and the camera site where the adjacent picture was taken) used for the triangulation. (Bottom panel) A three-dimensional representation of the resulting positions of the trail and the rocket trajectory and their two-dimensional projections onto the x-y, y-z, and x-z planes. The color coded points show the correspondent altitudes between the upper images and the points in the generated triangulation.

3.3 Results

The high-resolution triangulation described above produced the upleg and downleg wind profiles shown in Figure 3.4 for each of the two TMA launches. The profiles show features that are typical for geomagnetically quiet conditions. Although the peak wind speeds and shears are large, they fall within the range in the distribution plots for mid-latitude profiles (see, e.g. Larsen, 2002). The downleg wind profile from the first launch shows highly sheared winds of up to 90 $\mathrm{ms^{-1}km^{-1}}$

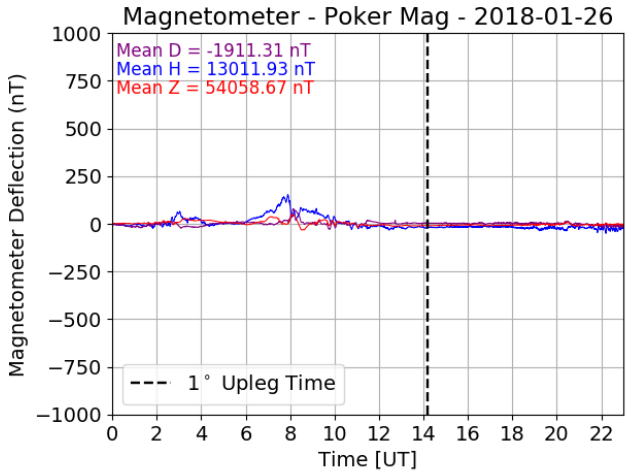

Figure 3.3: Magnetometer data from Poker Flat showing quiet geomagnetic conditions. The vertical dashed line represents the start time of the first upleg.

around the turbopause region between 100 and 105 km. Profiles of the potential temperature show that the altitude of the mesopause was ∼99 km based on both the Na lidar and NRLMSISE/00 temperature profiles during the first launch when the KHI billow structure was observed (these results are not included in this manuscript). The magnitude of the shear is large enough to meet the necessary condition for KHI, namely that the Richardson number is $Ri < 0.25$.

Indeed, the trail images showed direct evidence of KHI billow structure in the high-shear region, as illustrated in Figure 3.5, which shows the development of the billow structure, the generation of secondary instabilities, and the mixing associated with the break-up of the billow into turbulence, which occurs in less than 2 minutes in the image sequence. In the last image displayed in Figure 3.5 the trail becomes fainter within the KHI billow region, suggesting that mixing and diffusion is taking place. In the same image, the trail remains bright above and below the 100 to 105 km region.

The expression for the Richardson number can be written in the form (Scorer, 1997; Liu et al., 2004; Cushman-Roisin and Beckers, 2011)

$$Ri = \frac{N^2}{M^2} = \frac{\frac{g}{T}\left(\frac{dT}{dz} + \frac{g}{c_p}\right)}{\left[\left(\frac{du}{dz}\right)^2 + \left(\frac{dv}{dz}\right)^2\right]}; \tag{3.1}$$

where N is the Brunt-Väisälä frequency and M is the Prandtl frequency; g is the acceleration of gravity; c_p is the specific heat at constant pressure; u and v are the zonal and meridional wind

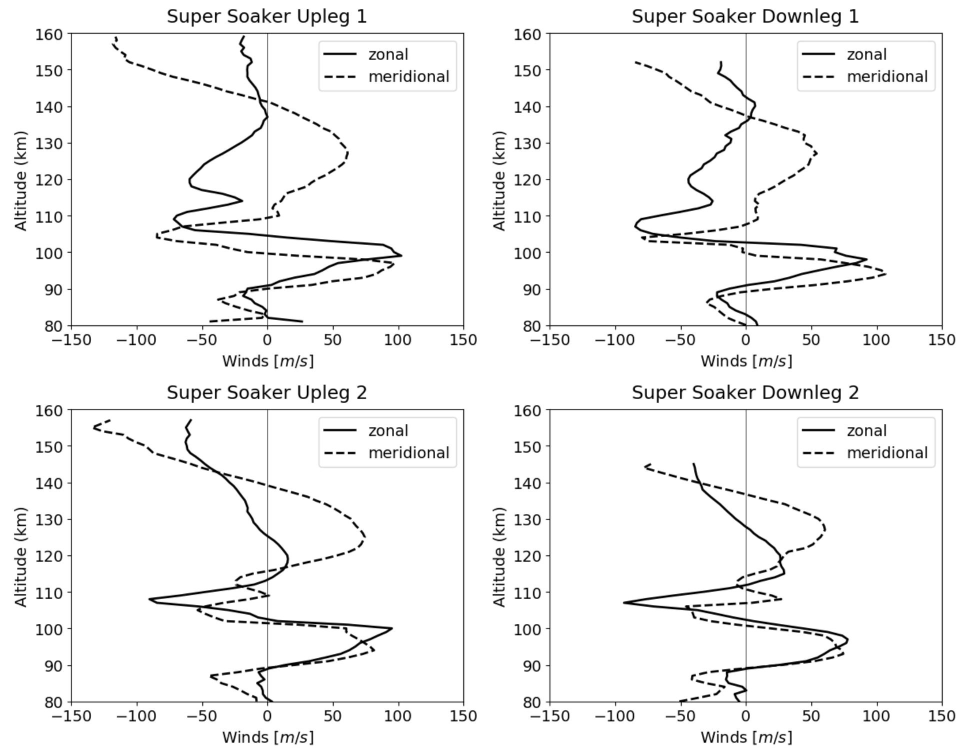

Figure 3.4: Wind profiles obtained from the two chemical tracer rockets. The wind profiles are calculated from the TMA trails in both up and down trajectories of the rockets, resulting in upleg 1 (14:12 UT), downleg 1 (14:16 UT), upleg 2 (14:49 UT), and downleg 2 (14:52).

components, respectively, from Figure 3.4; and T is the temperature(as displayed in Figure 3.6). The values for T were estimated with the NRLMSISE/00 empirical model (Picone et al., 2002). The Na lidar measurements in the altitude range where the billows were observed have rather large errors in the order of 20 K; and the lapse rate from the lidar profile (Figure 3.6) is also more unstable. Using NRLMSISE/00 values therefore gives a more conservative estimate for Ri. As seen in Figure 3.7, the Richardson number profiles show values below 1/4 for all four wind profiles. The smallest values occurred during the first launch near 100 km altitude in both the upleg and downleg profiles, although the eddy structure associated with the KHI was observed only in the downleg trail resulting from the first rocket launch and is shown in Figure 3.5.

The high-resolution triangulation results in Figure 3.8 show the development of the billow structure in a sequence of plots over a period of approximately one minute. This figure shows the KHI located between 100 and 105 km altitude. The eddy diameter and vertical scale (L_x and L_z) were approximately 5.2 and 3.8 km; and the wind speed near the center of the eddy at 102 km was

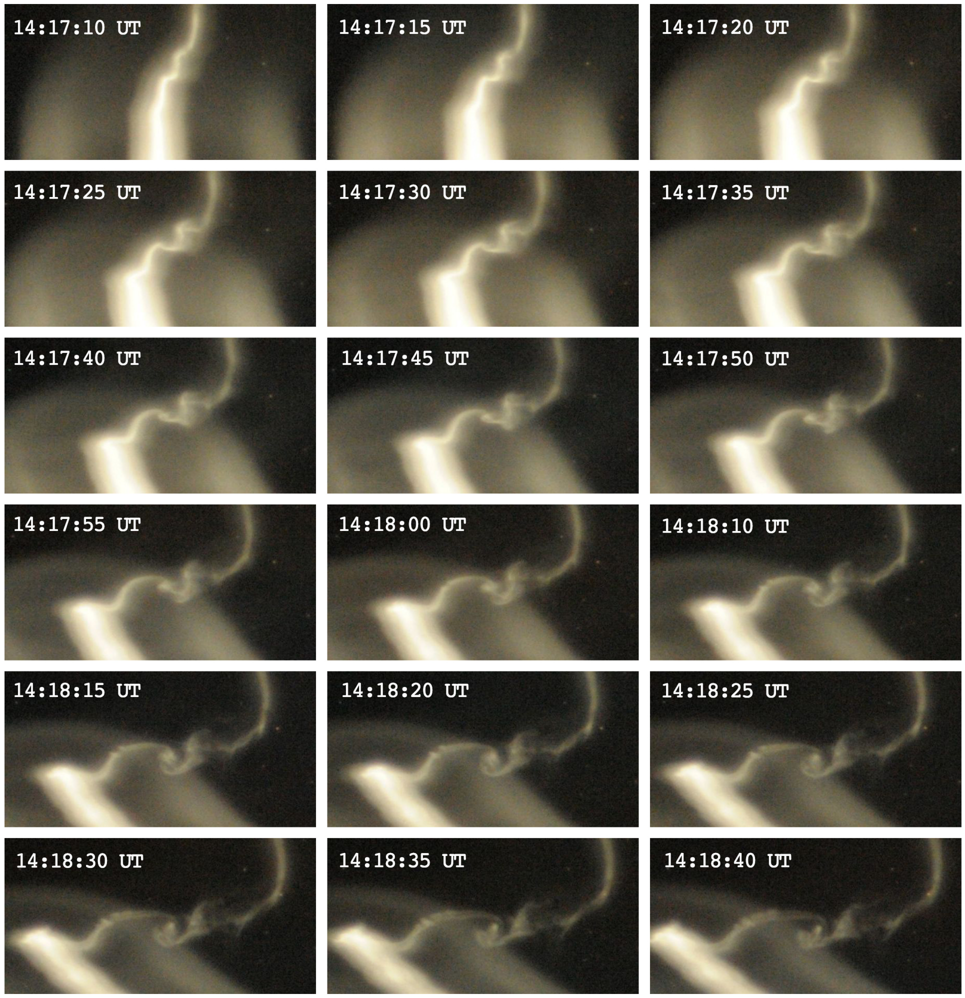

Figure 3.5: Evolution of the Kelvin-Helmholtz billow structure, present in the downleg 1 trail, in the zoomed-in images taken from Coldfoot, Alaska. Each image represents a 1-second exposure at a 5-second cadence, and the whole series represents the interval from 14:17:10 UT to 14:18:40.

44 ms^{-1}.These quantities were calculated by fitting the altitude of the crest of the KHI for U_z and U_x (purple points in Figure 3.8), and using the distances between the points as illustrated in the same figure (14:17:45 UT time stamp). These points were used to calculate the wavelength (distance between the two green points), the eddy diameter (distance between the lowest green and yellow points) and the vertical scale (distance between the purple and yellow points) of the KHI.

In a recent study Chau et al. (2020) used radar imaging observations of a KHI at a lower altitude in the mesosphere to obtain detail comparable to the case presented here. The summertime measurements from the high-latitude Middle Atmosphere Alomar Radar System showed the presence of billow structure around 85 km altitude, with Ri=0.15 and Reynolds number Re=3.9 × 10^4. The

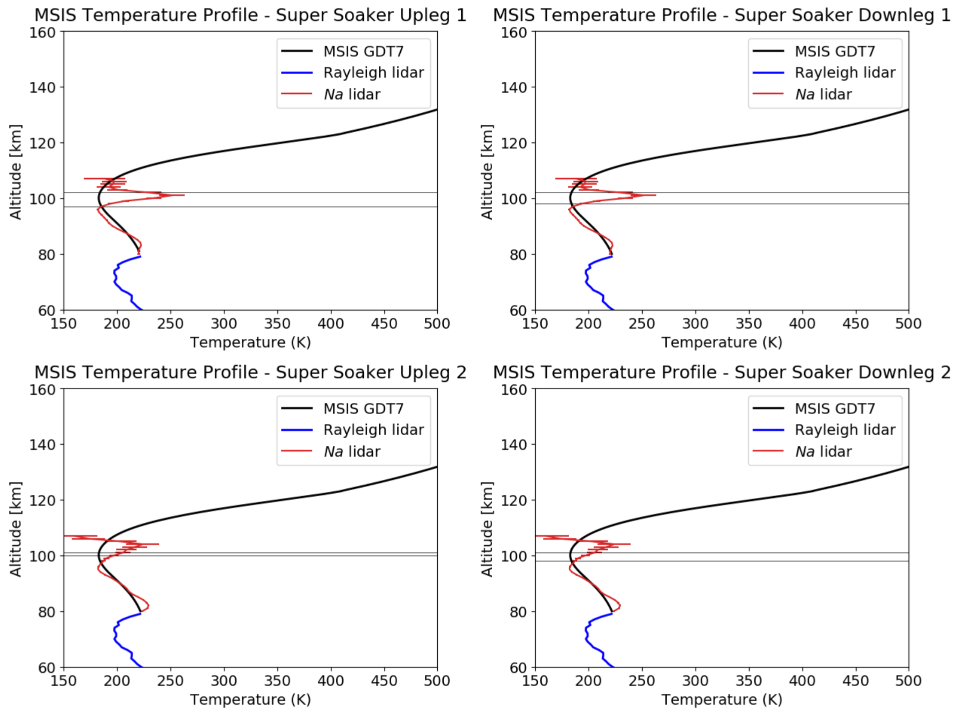

Figure 3.6: NRLMSISE/00 empirical model temperature profiles used to calculate the Ri from Figure 3.7 (black). Half-hourly averaged (from 14:00 UT to 14:30 UT for the first launch and from 14:30 UT to 15:00 UT for the second launch) Na lidar temperature profiles (red) and the Rayleigh lidar temperature (blue), both measured at Chatanika, Alaska during the launches. Horizontal lines enclose the region of $R_i < 1/4$ from Figure 3.7.

shear in the unstable region was 45 ms^{-1}km^{-1} at the time of the event. The authors also measured the billow width (3km), the thickness of the unstable layer (2.4 km), and the wavelength in the zonal direction (8 km). Our analysis follows theirs and a comparison of the observed parameters is presented in more detail in the next section (Table 3.1).

The Reynolds number (Re) was calculated for our case using the expression (Cushman-Roisin and Beckers, 2011)

$$Re = \frac{L_x\sqrt{u^2+v^2}}{\nu}, \tag{3.2}$$

where the background wind $\sqrt{u^2+v^2}$ (u and v are the zonal and meridional winds, respectively, obtained from Figure 3.4) is 43.8 ms^{-1}, the eddy diameter (L_x) is 5.2 km, and the kinematic viscosity (ν) is 31.6 m^{2}s^{-1} (calculated using temperature and neutral density from NRLMSISE/00) at 102 km. Re was 7.2$\times$10^3 for downleg 1 in the region where the billow structure was observed. The

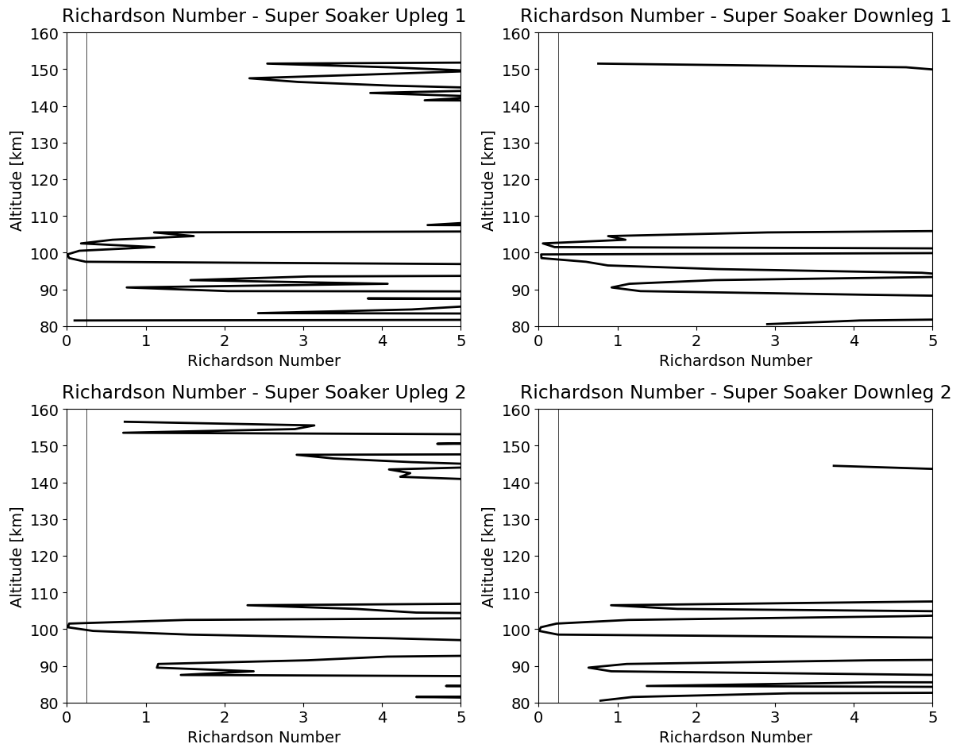

Figure 3.7: Richardson number profiles calculated with equation 3.1, using NRLMSISE/00 to estimate the temperatures and the winds obtained from the rocket measurements. Vertical dashed lines represent the threshold Ri value.

kinematic viscosity is calculated using

$$\nu = \frac{\mu}{\rho} = \frac{\beta T^{3/2}}{\rho\,(T+S)}, \tag{3.3}$$

where μ is the dynamic viscosity, ρ is the neutral density (from NRLMSISE/00), β is a constant equal to 1.458×10^{-6} kg(smK$^{1/2}$)$^{-1}$, and S is the Sutherland's constant equal to 110.4 K. This expression for the kinematic viscosity and the constants used in its calculation can be found in the book U.S. Standard Atmosphere (1976).

The billow root-mean-square vertical velocity $U_z = 29$ m/s was obtained from the triangulation in Figure 3.8; and, similar to Chau et al. (2020), we calculate root-mean-square horizontal velocity

$$U_x \sim \frac{U_z L_x}{L_z} = 39.5\text{ms}^{-1}. \tag{3.4}$$

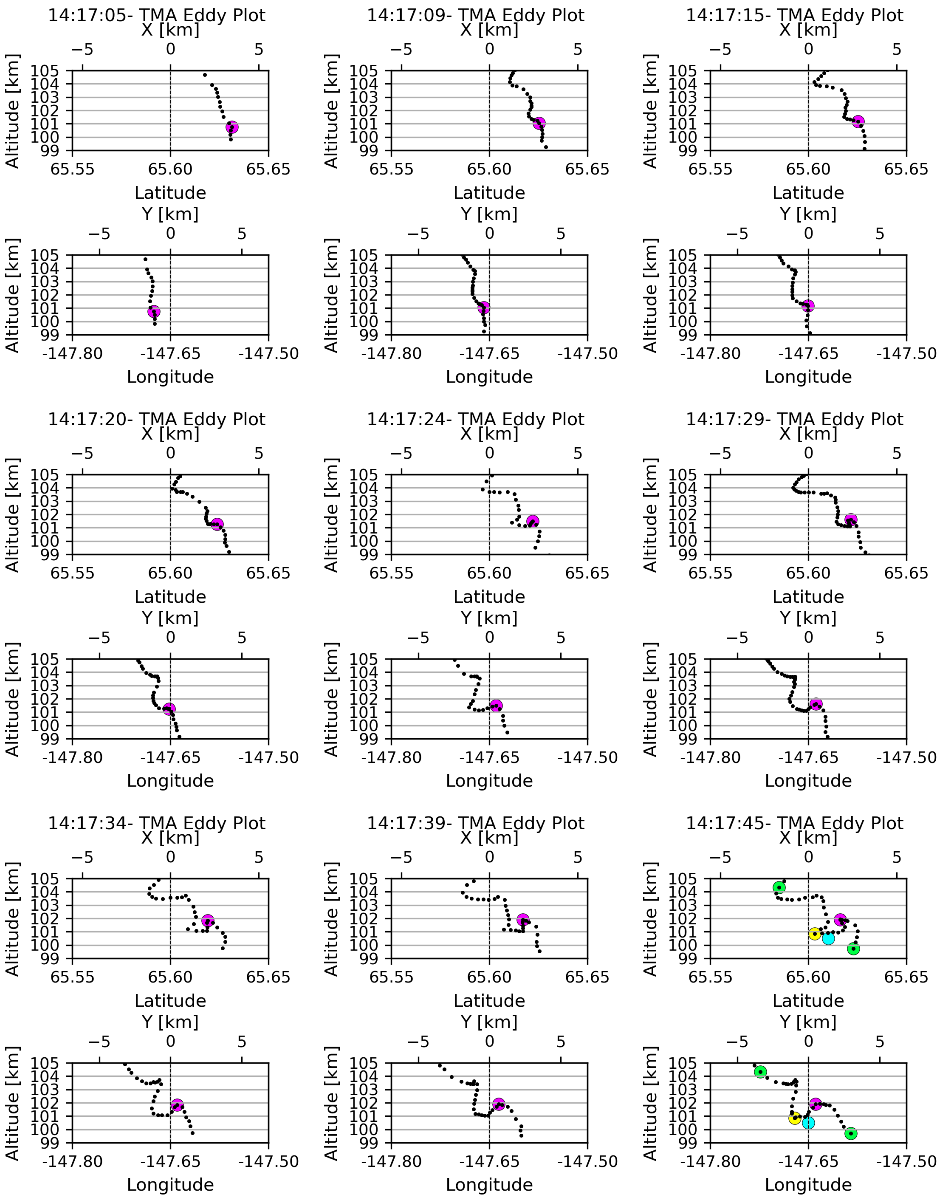

Figure 3.8: High resolution triangulation of the KHI billow evolutionpresent in downleg 1 (9 latitude and longitude plot pairs). Each individual figure has the projection of the eddy in latitude (top) and longitude (bottom) with the respective distances from the reference position between 14:17:05 and 14:17:45 UT. The distances from the reference latitude and longitude are represented as X and Y, respectively. The purple points represent the crest of the KHI and the point used to calculate the billow root-mean-square vertical and horizontal velocities of the eddy. The figure for 14:17:45 UT was used to calculate the wavelength (distance between the two green points), the eddy diameter (distance between the lowest green and yellow points), and the vertical scale (distance between the purple and cyan points) of the KHI.

The U_x was also measured using the triangulation in Figure 3.8 resulting in U_x=42.5 ms^{-1}; however, only the value 39.5 ms^{-1} has been used in the calculations present in this paper. The Froude number (Fr) can be estimated as

$$Fr = \frac{U_x}{NL_x} = 0.29. \tag{3.5}$$

This result represents characteristics of a subcritical flow ($Fr < 1$), which indicates weak stratification ($Fr > \mathcal{O}(10^{-2})$). The relationship between Fr and the turbulence dissipation rate (ϵ) can be written as

$$\epsilon = FrNU_x^2, \tag{3.6}$$

which results in $\epsilon = 38.1$ Wkg^{-1}, with $N = 0.0263$ s^{-1} (value used to calculate the Ri in equation 3.1 at 102 km, altitude of the KHI) for downleg 1. Table 3.1 summarizes the quantitative results and compares them with previous studies.

Parameters at z	Super Soaker (downleg 1)	SEEK-2 Larsen et al. (2005)	Chau et al. (2020)
Altitude z (km)	102	106	85
Ri	0.05	0.1	0.10-0.15
L_z (km)	3.8	1.5	2.4
L_x (km)	5.2	1.95	3
λ (km)	9.8	5	8
Re (z)	7.2×10^3	8.4×10^2	3.9×10^4
Fr (z)	0.29	0.37	0.80
U_z (ms^{-1})	29.2	29.7	12
U_x (ms^{-1})	39.5/42.5	38.6	15
ϵ (Wkg^{-1})	38.1	84	1.125
L_z/λ	0.38	0.3	0.3
L_x/Lz	1.35	1.3	1.25

Table 3.1: Quantitative summary of the KHIs from Super Soaker observed in the downleg 1 and calculated through the triangulation. The results of the KHI parameters estimated for the SEEK-2 (Larsen et al., 2005) and the study by Chau et al. (2020) in comparison to the Super Soaker KHI. The U_x =39.5 ms^{-1} represents the calculated version from equation 3.4; while U_x =42.5 ms^{-1} represents the direct measurement through triangulation.

3.4 Conclusions and Discussion

The Super Soaker launches were carried out in quiet geomagnetic conditions at high latitudes and showed the strong winds and large shears that also characterize the mesosphere/lower thermosphere region at mid- and low latitudes. The observed winds resemble those closer to the upper limit of the distributions in Figures 2, 3, and 4 in the article by Larsen (2002). As discussed by Liu (2017), the persistent large winds and shears appear to be driven by gravity wave forcing modulated by the background tidal oscillations, based on high-resolution general circulation model results. The analysis of the visible structure in the trails, the Ri calculations, and the high-resolution triangulation results (Figures 3.5, 3.7, and 3.8, respectively) all suggest the presence of Kelvin-Helmholtz shear instability in the flow during the launches. The image sequence and the triangulation of the billow structure show the full evolution of the KHI, from the initial perturbation in the trail to the appearance of dynamic instability to the development of enhanced mixing due to turbulence.

As discussed in the introduction, most observations of similar instability events have been made in the mesosphere (e.g., Bishop et al., 2004; Hecht, 2005; Lehmacher et al., 2007; Pfrommer et al., 2009; Hysell et al., 2012; Fritts et al., 2014; Baumgarten and Fritts, 2014; Chau et al., 2020) where the lapse rate is usually negative and closer to the adiabatic lapse rate than at higher altitudes near the mesopause and in the lower thermosphere region. Consequently, the Brunt-Väisälä frequency is smaller in the mesosphere as well, and more modest shears can therefore generate dynamic shear instability in this region. As observed by Baumgarten and Fritts (2014), for example, the interaction of random gravity waves is the source of shears that drive the instability in the mesosphere. Shears in this region are usually short-lived, on the order of 15 minutes, due to the transient nature of gravity wave interactions. In the mesopause and lower thermosphere region, Larsen (2002) found that the approximate altitude range of maximum shear is 95 to 110km. The height where the maximum shear occurs varies with time in this range of altitudes, following the downward phase progression of waves propagating through the region (see, e.g., Liu, 2017). The amplitudes of these waves are modulated by an envelope that enhances the shears in this critical range of the lower E-region. This effect was discussed by Larsen and Fesen (2009), and a particular example can be seen in Figure 8 of that article. There is also further discussion of the effect from a modeling perspective in the article by Liu (2007), which shows that the magnitude of the shears is limited by the static stability, and in a broader context by Liu (2017). The high-shear region is statically stable due to the positive lapse rate, as shown in Figure 3.6. However, between the mesosphere and thermosphere, in the region highlighted by horizontal lines in Figure 3.6, the lapse rate is nearly isothermal, based on the NRLMSISE/00 temperature profile. Therefore, it requires larger shears to generate shear instabilities. Our measurements, along with those from earlier lidar and rocket studies, suggest that the shears can be long-lived, on the order of several hours (see e.g., Larsen and Fesen, 2009).

Another example of a KHI billow observation with rocket tracers in this altitude range is from the SEEK-2 campaign (Larsen et al., 2005). The billows were observed at altitudes between 100 and 115 km, although the largest amplitudes were found between 100 and 110 km. The layer with the billows was characterized by Richardson numbers below the critical value of 1/4. Table 3.1 shows the estimated parameters for the SEEK-2 campaign. The horizontal wavelength in that case was found to be ∼5 km. Even though the wavelength of SEEK-2 KHI was approximately half of the Super Soaker measurements (9.8 km) the ratio of the vertical scale and the wavelength for both campaigns were compatible. Larsen et al. (2005) observed the KHI structure in the upleg trail (see Figure 11 of that article). The downleg trail located 50 km further downrange showed evidence of strong turbulent mixing indicated by the rapid diffusion of the TMA tracer in that region, and a significant reduction in the wind shear relative to the upleg. The rapid diffusion is similar to what is seen in the last few frames of Figure 3.5, where the TMA quickly dispersed within the altitude range of the unstable layer. Incoherent scatter radar observations of a KHI in the transition region between the mesosphere and lower thermosphere was analyzed by Hysell et al. (2012). Their eigenfunction analysis showed phase propagation (50 ms^{-1}) and horizontal wavelengths (10 to 15 km), comparable with those presented here (52.7 ms^{-1} and 9.8 km, respectively).

The modeling results of Fritts et al. (2014) for the evolution of the billow structure for different Ri and Reynolds number (Re) combinations show that lower Ri and larger Re produce more rapid mixing. They also examined the effects of varying Ri on the eddy break-down into secondary instabilities. For a higher Ri of 0.20 the eddy's core degenerates into secondary instability first; while for lower Ri (0.05 and 0.10) the secondary instabilities appear first around the edges of the eddy with its core remaining stable for a longer period of time. They showed that the characteristics of the instability structure have a strong dependence on both Ri and Re. We can compare the instability structure from our observations qualitatively with the their findings, specifically Event 1, which was deeper and had stronger turbulence with lower Ri. Their simulation results for Ri=0.05 and

Re=2500 show general agreement with the results presented here, where Ri=0.05 and the Reynolds number was estimated to be Re=7.2×10^3 at 102 km in the center of the eddy. The observed billows break down into secondary instabilities at the edge of the eddy (see Figure 3.5), with the core maintaining integrity for a longer period of time. As to its physical characteristics, Baumgarten and Fritts (2014); Fritts et al. (2014) reported a wavelength of ∼10 km and a depth of ∼2.5-3 km, giving a billow depth to wavelength ratio of approximately 0.25-0.4. From Figure 3.8, the wavelength is 9.8 km and the depth is 3.8 km, which makes the ratio ∼0.38, well within the range of ratios from the Fritts et al. (2014) simulation. Figure 3.5 also shows that it takes a little less than 2 minutes for the billow to develop and break into turbulent mixing. The last image (bottom right of the panel in Figure 3.5) shows the TMA diffusion associated with the turbulence that followed the KHI.

The event analyzed by Chau et al. (2020) had maximum shear of 45 ms^{-1}km^{-1} at approximately 85 km altitude. This shear is comparable to those generally present in the mesosphere, as discussed by Liu (2007, 2017). The shears for our case (Figure 3.4) are approximately twice as large (∼90 ms^{-1}km^{-1}). The eddy diameter (L_x), the thickness of the unstable layer (L_z), and the horizontal wavelength (λ) for their event are 3, 2.4, and 8 km, respectively. These results are different from the results presented here, with L_x=5.2 km, L_z=3.8 km, and λ=9.8 km, respectively. However, the ratio L_z/λ for both studies is the same ($\sim$ 0.3) and the ratio L_x/L_z is similar ($\sim$ 1.3). Their estimation of the turbulence dissipation rate (1.125 Wkg^{-1}) is smaller than the value from equation 3.6 (18 Wkg^{-1}) due to the ratio of the mass densities of the two regions, which is $\sim \mathcal{O}(10^{-1})$. Their calculated values of the Froude and buoyancy Reynolds numbers were 0.8 and 2.5×10^4, which results in a Reynolds number of 3.9×10^4 using the relationship $Re_b = ReFr^2$ as described by Pouquet et al. (2019). For the Super Soaker case these quantities were $Fr = 0.29$ and Re=7.2×10^3. The Reynolds number in the altitude range around 85 km (Chau et al., 2020) is expected to be larger than that around 100 km, due to the lower viscosity. The lower Froude number indicates that the KHI studied here occurred in a region where stratification effects are more important than those presented by Chau et al. (2020) for an altitude of 85 km. Their measurement of the billow root-mean-square vertical velocity (U_z=12 ms^{-1}) is a little less than half what we measured (U_z=29 ms^{-1}). This represents evidence of the rapid mixing and the vertical mobility within the unstable altitude range at 100 to 105 km.

We can conduct a similar analysis for the SEEK-2 event (Larsen et al., 2005). Assuming that the ratios $L_z/\lambda = 0.3$ and $L_x/L_z = 1.3$ are the same for that case, using the horizontal wavelength calculated by Larsen et al. (2005) and using NRLMSISE/00 to calculate the viscosity, one can estimate the same parameters described above Chau et al. (2020), namely, $N = 0.0257\text{s}^{-1}$, $\epsilon = 84$ W/kg, $Fr = U_x/\sqrt{gL_x} = 0.28$, and $Re = 843$. The calculation is approximate, but in both instances these parameters are similar. The Brunt-Väisälä frequency N for both cases is approximately the same. In both SEEK-2 and Super Soaker we have a virtually constant temperature profile within the range of the instability. The value for Fr is also very similar, which means that the level of stratification for both campaigns is roughly the same and slightly stronger for SEEK-2. The ϵ parameter and Re are different, as expected, primarily due to the difference in ν between the altitudes where the instabilities were observed.

The fact that dynamic instabilities can occur in the stable lapse rate region of the mesosphere/lower thermosphere transition is not new. Measurements of background wind shears have already suggested that, and to a more limited extent, so have direct observations of billow structure. The results presented here give a more quantitative estimate of the parameters and transport and mixing effects that can be expected for such instabilities at those altitudes. These results are indicative of a mechanism for enhanced transport of mass, energy, and chemical constituents across atmospheric layers where the static stability typically inhibits such transport.

3.5 Summary

In this paper we have analyzed the occurence of a Kelvin-Helmholtz instability in the high latitude region between the D- and E-regions. We summarize our findings as follows:

1. Direct observation of the KHI is shown in Figure 3.5. The turbulence, which resulted from the KHI, is also evident in that altitude range due to the faster dispersion of the TMA. The evidence of overturning structure and turbulence in this region is expected to produce mixing and vertical transport across the statically stable layer.

2. The evolution of the KHI is such that the billow breaks down into turbulence from the edges in, which is compatible with the DNS analysis by Fritts et al. (2014).

3. The high-resolution triangulation of the KHI (Figure 3.8) allowed us to estimate the following quantities present in Table 3.1:

   (a) L_x=5.2 km

(b) L_z=3.8 km

(c) λ=9.8 km

(d) Fr=0.29

(e) Re=7.2 × 10^3

(f) U_z=29.2 ms^{-1}

(g) U_x=39.5 ms^{-1} (calculated) and 42.5 ms^{-1} (measured)

(h) ϵ=38.1 Wkg^{-1}

4. The dimensional analysis of the KHI presented here shows that while the vertical scale to wavelength ratio and the ratio between horizontal to vertical scales are similar to those presented by Chau et al. (2020), the phenomenon is of a different nature, where the high shear ($\sim$90 ms^{-1}) is the triggering mechanism. The triggering mechanism of the KHI presented here is likely the same that generated the KHI in the study of the SEEK-2 campaign by Larsen et al. (2005).

3.6 Acknowledgments

RM and MFL acknowledge partial support from NASA grant NNX16AF67G and NSF grants AGS-1552214 and AGS-1360594 while the research was conducted. IA and MHS acknowledge support from NASA grant NNX16AF67G. The data used in this paper can be found in the repository `https://doi.org/10.5281/zenodo.3905282`. The NIK*.dat files represent the triangulation of the eddy structure (used to generate Figure 3.8) and the Po*.vel represent the wind profiles (used to generate Figure 3.4). This work uses pyglow, an open-sourced Python package that wraps several upper atmosphere climatological models, is also available in the data repository mentioned above (see ‘pyglow-master.zip’).

Chapter 4

Measurements of the meridional advective acceleration and neutral wind forcing in the E-region during different geomagnetic activity

Rafael L.A. Mesquita[1], Stephen R. Kaeppler[1], Miguel F. Larsen[1], Roger Varney[2], Ashton Reimer[2], Robert F. Pfaff[3], Irfan Azeem[4], John D. Craven[5], and Mark Conde [5].

[1] Physics and Astronomy Department, Clemson University, Clemson, South Carolina, USA.

[2] Center for Geospace Studies, SRI International, Menlo Park, California, USA.

[3] NASA/GSFC, Greenbelt, Maryland, USA.

[4] Atmospheric & Space Technology Research Associates, LLC, Louisville, Colorado, USA.

[5] University of Alaska Fairbanks, Fairbanks, Alaska, USA.

To be submitted as:

Mesquita, R. L. A., Kaeppler, S. R., Larsen, M. F., Varney, R., Reimer, A., Pfaff, R. F.: Measurements of the meridional advective acceleration and neutral wind forcing in the E-region at

different geomagnetic activity levels, Journal of Geophysical Research: Space Physics, 2021.

Abstract

Forcing of high-latitude E-region winds has been extensively studied in various scales. However, measurements of the advective acceleration in the upper atmosphere are sparse in previous studies because it is difficult to observe using traditional methods. In this study, we used sounding-rocket launches at Poker Flat Research Range to measure the meridional advective acceleration of the horizontal winds in different geomagnetic activity levels. These measurements occurred in Kp indices ranging from 0.3 (Super Soaker) to 4.3 (Auroral Jets). The Poker Flat Incoherent Scatter Radar (PFISR) was used to measure F-region plasma velocities and E-region electron densities, which we used to calculate the instantaneous Lorentz acceleration. Measurements from the Alaska magnetometer network and the global auroral indices were used to assess the geomagnetic levels on different scales. Winds measured in different geomagnetic activity levels were within the same range of magnitude below 110 km (<100 ms^{-1}). Above that altitude, winds increased with geomagnetic activity, peaking at ~300 ms^{-1} (Auroral Jets). The meridional advection and instantaneous Lorentz accelerations increased with geomagnetic activity and were mainly in the same direction. The analysis of the modified Coriolis parameter (Coriolis and centrifugal parameters minus the Hall drag) showed that in certain altitudes the winds have a tendency to either keep an air parcel in the acceleration channel or to turn equatorward in strong geomagnetic activity.

4.1 Introduction

Neutral wind advection corresponds to the transport of wind gradients by the background wind. During active geomagnetic periods, enhanced electric fields and plasma density inside the aurora oval can cause large winds due to the Lorentz force, which further intensifies the nonlinear advective effects in the high-latitude thermosphere (Conde et al., 2001; Anderson et al., 2012; Fuller-Rowell, 2013). This increased advection in the meridional direction can transport the wind gradients outside the oval, accelerating winds on a larger scale. Although advection has been quantified in modeling studies (e.g., Mikkelsen et al., 1981; Fuller-Rowell and Rees, 1984; Kwak and Richmond, 2007; Fuller-Rowell, 2013), observations of the forcing terms including the advection have been sparse. Unlike other forcing terms that depend only on the neutral and plasma velocities, observing advection requires simultaneous measurements of winds at different locations to calculate the wind gradients. Few studies have measured these gradients in the thermosphere (F-region wind gradients measured by Anderson et al., 2012; Aruliah and Griffin, 2001, and references therein). Other studies presented evidence of strong wind gradients at high-latitudes but did not calculate the gradients or advection (Killeen and Roble, 1984; Conde et al., 2001; Zou et al., 2021). Therefore, the advection has not been directly observed in the E-region. Sounding rocket measurements of winds represent an opportunity to observe the advective, Coriolis, and centrifugal accelerations. Incoherent scatter radar measurements of plasma velocity and electron density allow for the calculation of the Lorentz acceleration. The purpose of this investigation is to address the scientific question: How does the vertical distribution of forces in the E-region and the advection change as a function of geomagnetic activity?

Previous modeling studies simulated the high-latitude forcing and showed that the advection, ion drag, Coriolis, and pressure gradient can be significant terms in the neutral momentum equation in the thermosphere (Mikkelsen et al., 1981; Killeen and Roble, 1984; Fuller-Rowell and Rees, 1984; Kwak and Richmond, 2007, both E- and F-regions by). Using a two-dimensional (altitude and latitude) thermospheric model, Mikkelsen et al. (1981) modeled the forces to interpret the sounding rocket wind observations by Mikkelsen et al. (1981), which occurred in the early evening MLT sector. They displayed accelerations as a function of altitude (Mikkelsen et al., 1981, Figures 2-5 of) and showed that the horizontal advection was comparable with the Lorentz force and was the dominant acceleration at certain altitudes above 110 km. They also found an approximate balance between Coriolis and curvature terms, where the meridional curvature term is the centrifugal acceleration. The Coriolis acceleration turns the winds to the right in the northern hemisphere while the Hall drag tends to turn winds to the left. Mikkelsen et al. (1981) estimated the Hall drag to peak was a factor of three smaller than the Coriolis parameter ($13.5 \times 10^{-5} s^{-1}$), which caused large westward winds to turn in the poleward direction. Fuller-Rowell and Rees (1984) used a three-dimensional, time-dependent, global model to simulate the response of the high-latitude thermosphere to a substorm. They found that in the pre-midnight sector, the pressure gradient force, centrifugal force, and the Coriolis force balance, which causes winds accelerated by Lorentz forcing to be sustained over many hours. They also showed the mechanism in which faster winds produce a larger radius of curvature in the winds.

One study, Killeen and Roble (1984), presented a set of forcing terms simulated with the thermospheric general circulation model (TGCM). Their steady-state run of the model showed that ion drag and pressure gradient approximately balance in the F-region (300 km) with Coriolis and advective accelerations playing an important role in the E-region (120 km). Kwak and Richmond (2007) used the Thermosphere Ionosphere Electrodynamics General Circulation Model (TIE-GCM) to investigate the high latitude wind dynamics as a function of altitude during different geomagnetic conditions. They used the Weimer model (Weimer, 2001), which uses the interplanetary magnetic field (IMF) as a proxy for geomagnetic activity, to drive the high-latitude convection pattern. They showed that the meridional (divergent or convergent) pressure gradient, Coriolis force, and horizontal advection (primarily centrifugal) form an approximate balance above 123 km. This causes the rotational ion drag (Pedersen) to accelerate winds in a two-cell convection pattern with a delay. They found that the Hall drag contributes to divergent (equatorward) flows below 123 km, causing the flow to be in modified geostrophy similar to the study of Larsen and Walterscheid (1995). Kwak and Richmond (2007) discussed that curvature terms do not increase quadratically with the winds due to the tendency of fast winds to produce larger radii of curvature. The TIE-GCM results indicated that the horizontal advection magnitude is larger above 123 km.

Although the modeling studies have shown that advection can be an important term (Mikkelsen et al., 1981; Kwak and Richmond, 2007; Fuller-Rowell, 2013), advection is not routinely observed. Tsuda et al. (2009) argued that the advection was negligible due to the sudden onset of a geomagnetic substorm and the absence of activity preceding their European Incoherent Scatter Scientific Association (EISCAT) radar observations. Their neutral winds measurements peaked at 225 ms^{-1} at 118 km in the hour before the event with $Kp < 3$. Cai et al. (2019) used a Fabry-Perot interferometer (FPI) to show how F-region winds were impacted by substorms. They mentioned that advection could be an important source of forcing for events three and four in their investigation, although they did not calculate this acceleration. They recorded winds of approximately 125 ms^{-1} shortly before event three of their paper. They also reported accelerations up to 0.1 ms^{-2} due to energy deposited during substorms in the F-region. Anderson et al. (2012) used the overlapping region between two scanning Doppler imagers (SDI) to derive wind gradients. This technique showed that in the high-latitude Alaskan F-region the largest wind gradient was the geomagnetic meridional shear of zonal winds due to ion drag, followed by the geomagnetic meridional shear of the meridional wind. Recently, Zou et al. (2021) also used SDI to measure winds and reported that it was unclear whether the acceleration they measured was an effect of high-latitude advection or local forcing mechanisms.

A number of techniques have been developed to measure the neutral wind profiles in the

E-region; however, these methods have generally not been used to quantify advection. Brekke et al. (1973) developed a now well-known technique to measure thermospheric winds using incoherent scatter radars (Johnson et al., 1987; Brekke et al., 1994; Nozawa and Brekke, 1995, 1999a,b; Maeda et al., 1999, ISR, e.g.,). However, techniques to measure advection with this instrument have not been tested yet. Maeda et al. (1999) used EISCAT to calculate the material derivative of the neutral wind $\vec{U}$ but did not address the advection separately. (Nozawa et al., 2005) used EISCAT at Svalbard and Tromsø to measure the Lorentz force, the Coriolis acceleration, and the Eulerian acceleration (total) of the wind ($\partial\vec{u}/\partial t$). They found that ion drag is effective at accelerating winds above 107 km at Tromsø and 118 km at Svalbard. They calculated a maximum zonal ion drag of 0.03 ms^{-2} at 115 km altitude using the Tromsø EISCAT data.

Another prominent approach to calculate the E-region winds uses sounding rockets to release vapor tracers. Larsen (2002) presented a collection of 400 neutral wind profiles measured with this technique between 1958 and 2002. Larsen et al. (1997) discussed the results of the Atmospheric Response in Aurora (ARIA) experiment, which launched rockets out of the Poker Flat Research Range during various levels of geomagnetic activity. They found that the aurora causes a jet to develop between 110 and 120 km altitude, showing that winds generally increase with aurora activity. However, the authors did not calculate the forcing terms during the ARIA launches.

This technique can be used to measure thermospheric winds with high accuracy and to determine neutral momentum equation forcing terms, such as Coriolis and centrifugal accelerations. Typical errors are approximately 5-10 ms^{-1}, as discussed by Larsen et al. (1998). It can also be used to measure the advective acceleration along the rocket trajectory when the winds are observed in multiple locations, such as upleg and downleg. However, a disadvantage of this technique is that it lacks the time history of the winds and it can only occur at night during periods when the moon is down.

In this study we use sounding rockets to measure the thermospheric E-region wind profiles at different geomagnetic activity levels at high latitude. We calculate the Coriolis and centrifugal accelerations, and the meridional advection of the winds. We also use the Poker Flat Incoherent Scatter Radar (PFISR) measurements to investigate the instantaneous Lorentz forcing. Then, we analyze these accelerations individually and by combining the turning terms (Coriolis and centrifugal parameters, and Hall drag). We compare our results to the modeling studies of Mikkelsen et al. (1981) and Kwak and Richmond (2007).

4.2 Measurements and data analysis

4.2.1 Regional auroral electrojet

The global auroral electrojet index (AE) developed by Davis and Sugiura (1966) is one of the main tools to assess the state of geomagnetic activity. A network of magnetometers in the northern hemisphere high-latitude sector measures AL and AU to calculate the AE index (Weygand et al., 2014). A large AE signifies a large difference between westward and eastward electrojet currents, which is characteristic of auroral activity. Because of the localized nature of the sounding rocket and PFISR observations, a regional auroral index may be more relevant for this investigation. Tanskanen (2009) developed IL, a regional auroral index similar to the AL index, to measure the westward electrojet currents.

We used the Alaska Magnetometer network data to calculate the regional auroral electrojet indices (IE = IU-IL). The data used to estimate IU and IL is the total measured magnetic field component minus its daily average for that specific day. For each time step, the values for the highest (IU) and lowest (IL) magnetometer measurements are stored and subtracted from each other, resulting in a regional auroral index (IE). These indices provide insight into the state of the electrojet over Alaska, which signifies the occurrence of a substorm within the boundaries of the magnetometer network.

4.2.2 Sounding rocket observations

The wind profiles presented in this paper were measured with the rocket-borne release of trimethylaluminum (TMA), a non-toxic liquid that produces chemiluminescence on contact with atmospheric oxygen, glowing for several minutes (Rosenberg et al., 1963; Larsen, 2002, 2013). All the experiments in this study were carried out at the Poker Flat Research Range in Alaska (65.13°N, 147.47°W) with ∼11:00 Universal Time (UT) magnetic midnight. Although there are many rocket-borne TMA wind profiles for the high-latitude sector (Larsen, 2002), this paper focuses on five sounding rocket missions (JOULE II, HEX II, MIST, Auroral Jets, and Super Soaker) because of their concurrent PFISR and Alaska magnetometer network data.

The TMA trails created along the rocket trajectory drift with the neutral winds. Before and after the apogee the trails are named “upleg” and “downleg”. The trails are photographed from at least two ground sites to determine the position of each point in the trail through triangulation.

The triangulation technique is described in detail by a number of investigations (Larsen et al., 1998; Larsen, 2000a; Ingersoll, 2008; Mesquita et al., 2020, and references therein). It consists of a coordinate transformation between TMA image pixels to the trail altitude, latitude, and longitude. We calculated the positions of the TMA trail over time by repeating the process on selected sets of image pairs, which we then converted into zonal and meridional velocities.

The primary source of error in the triangulation technique comes from the distance of closest approach between the line-of-sight projections from the two camera sites. A perfect interception between the two lines would result in zero uncertainty. The measurement error associated with these distances is approximately 5-10ms^{-1} as discussed by Larsen et al. (1998).

4.2.3 PFISR vector velocities and instantaneous Lorentz acceleration calculation

We calculate the Lorentz force using PFISR observations. Here we use the Lorentz acceleration without the neutral winds to focus exclusively on the magnetospheric forcing. Therefore, we introduce instantaneous Lorentz acceleration, which does not depend on the neutral winds. This equation is defined as

$$\vec{LF} = \left[\frac{\sigma_P B^2}{\rho}(v_E) + \frac{\sigma_H B^2}{\rho}(v_N)\right]\hat{\phi} + \left[\frac{\sigma_P B^2}{\rho}(v_N) - \frac{\sigma_H B^2}{\rho}(v_E)\right]\hat{\theta}, \tag{4.1}$$

where ρ is the neutral atmospheric density, the subscript N and E correspond to the directions in which these velocities are positive (north and east), and

$$\vec{v} = \frac{\vec{E} \times \vec{B}}{B^2}, \tag{4.2}$$

is the plasma velocity positive east and north, where $\vec{E}$ is the electric field. We use the NRLMSISE-00 Atmosphere Model (Picone et al., 2002) to determine the neutral density, which is used to calculate the Pedersen (σ_P) and Hall (σ_H) conductivities with the equations in Appendix 4.7. All of the quantities in equation 4.1 are calculated in geographic coordinates, with ϕ being the longitude (positive east) and θ the latitude (positive north).

The Poker Flat Incoherent Scatter Radar (PFISR) is a phased array radar capable of electronic beam steering on a pulse-to-pulse basis (Kelly and Heinselman, 2009a,b). We used this radar to determine the electron density (N_e) and to calculate the F-region plasma vector velocities ($\vec{v}$) using the Bayesian approach described by Heinselman and Nicolls (2008) and all beam directions. The calculation uses the long pulse beam to determine the F-region plasma velocity and uses the alternating code beam to measure the E-region plasma density with a range resolution of 5 km. The beam configuration is also described by Heinselman and Nicolls (2008).

4.2.4 The advective acceleration calculation and the neutral momentum equation

Simultaneous observations of the winds at multiple locations are needed to calculate the wind gradients and advection. Anderson et al. (2012) established the measurement of wind gradients by using bi-static SDI instruments. This technique is limited to a few locations in the Alaskan F-region, as explained by Zou et al. (2021). The sounding rocket wind measurements at Poker Flat Research Range provide a unique opportunity to determine the advective acceleration of neutral winds in the E-region. These measurements produce spatially separated wind profiles that are necessary to estimate the wind gradients in the meridional direction because of the northward rocket trajectories. To define the correct sign of the advection, as well as the remaining terms estimated in this study, we define the numerical neutral momentum equation in zonal and meridional directions as

$$\frac{\partial u_E}{\partial t} = -\frac{u_N^{\mathrm{UP}}}{R}\left(\frac{u_E^{\mathrm{DO}} - u_E^{\mathrm{UP}}}{\theta^{\mathrm{DO}} - \theta^{\mathrm{UP}}}\right) + \left[\frac{\sigma_P B^2}{\rho} v_E + \frac{\sigma_H B^2}{\rho} v_N\right] + f u_N^{\mathrm{UP}} \tag{4.3}$$

and

$$\frac{\partial u_N}{\partial t} = -\frac{u_N^{\mathrm{UP}}}{R}\left(\frac{u_N^{\mathrm{DO}} - u_N^{\mathrm{UP}}}{\theta^{\mathrm{DO}} - \theta^{\mathrm{UP}}}\right) + \left[\frac{\sigma_P B^2}{\rho} v_N - \frac{\sigma_H B^2}{\rho} v_E\right] - f u_E^{\mathrm{UP}} - \frac{(u_E^{\mathrm{UP}})^2}{R}\tan\theta, \tag{4.4}$$

where $\vec{u} = u_E\hat{\phi} + u_N\hat{\theta}$.

Equations 4.3 and 4.4 include the Eulerian wind acceleration (here referred to as total acceleration: the sum of all forcing terms calculated in this study), the meridional advection, the instantaneous Lorentz forcing, and the Coriolis and centrifugal accelerations (equation 4.4 only). The superscript UP and DO refer to the rocket position and wind measurements in the upleg and downleg. For all of the cases discussed in this paper, the downleg trail is always located north of the upleg trail.

A few assumptions are necessary to calculate the advection. Equations 4.3 and 4.4 include only the meridional advective acceleration of zonal and meridional winds because no two simultaneous wind profiles are measured along the same latitude. The vertical advection can be significant due to large wind shears in the low thermosphere (Larsen, 2002) where a small vertical wind can be present. The vertical advection cannot be estimated because the vertical wind measurements are absent. The zonal advection cannot be estimated because the rocket trajectory is in the northward direction. However, we neglect the zonal advection because in the auroral region the gradients are larger in the meridional direction. Anderson et al. (2012) showed that, in the high latitude F-region, the meridional gradient of the zonal winds was the largest. This was followed by the meridional gradient of the meridional winds. Other assumptions include:

1. The winds in uplegs and downlegs are measured simultaneously, i.e., we assume $\partial/\partial t$ equals zero between uplegs and downlegs. In reality, the upleg measurement occurs between 1 and 3 minutes before the downleg. This is a good assumption since applying an acceleration of 0.07 ms^{-2} to an air parcel (value close to the maximum accelerations displayed in Figure 4.6) for two minutes gives a difference in wind speeds of 8.4 ms^{-1}, which is a small fraction of the wind measurements in the altitude range of interest.

2. The rocket moves faster than the gradients. This assumption is similar to the assumption above, but necessary since the sampled gradient needs to be stationary. This is a fair assumption given that the rockets move at approximately 1000 ms^{-1}.

3. The measured winds are equal to the winds in the rocket trajectory. This trajectory is determined with high accuracy using radar and GPS. The TMA assumes the velocity of the neutral winds shortly upon releasing. Therefore, a simple numerical regression of the three-dimensional position of the TMA over time coincides with the rocket trajectory (see Figure 2 of Mesquita et al. (2020)). However, we note that in the 2 to 3 minutes of images used to determine the winds for each trail, the TMA drifts away from the rocket trajectory by a considerable amount (at 100 ms^{-1} the TMA travels 18 km in 3 minutes).

While meridional advection is obviously not the full advection, we refer to the meridional advection of zonal and meridional winds as "advection of u_E and u_N" from this point on for simplicity.

Campaign	Kp	Launch time (UT)	(MLT)
Super Soaker	0.3	01/26/18 - 14:10	01/26 - 03:15
JOULE II	2.7	01/19/07 - 12:31	01/19 - 01:31
HEX II	3.3	02/14/07 - 09:38	02/13 - 22:22
MIST	4.0	01/26/15 - 09:15	01/25 - 22:10
Auroral Jets	4.3	03/02/17 - 05:50	03/01 - 18:40

Table 4.1: Launch time for the first rocket of each campaign, organized by Kp index, in both UT and MLT.

4.3 Results

In the following subsections we detail the geomagnetic conditions for each of the launches and classify them into three categories based on geomagnetic activity level, i.e., the Kp index. The five sounding rocket campaigns in order of geomagnetic activity are Super Soaker, JOULE II, HEX II, MIST, and Auroral Jets. The launch times and Kp index for each of these campaigns are shown in Table 4.1. We describe the detailed background geomagnetic activity of each campaign in terms of the local and global auroral indices, and the PFISR measurements. Using the Kp index, we classify the campaigns as follows:

1. **Quiet geomagnetic activity**, with no activity whatsoever, Kp=0.3, during the Super Soaker campaign;
2. **Moderate geomagnetic activity**, with winds measured in the presence of substorms, Kp$\sim$3, during the JOULE II and HEX II campaigns; and
3. **Strong geomagnetic activity**, with winds measured during strong substorms, Kp$\sim$4, during the MIST and Auroral Jets campaigns.

4.3.1 Quiet geomagnetic activity (Kp=0.3)

The Super Soaker campaign occurred during a geomagnetically quiet interval, with Kp=0.3. It is included in this analysis as a control because the campaign was designed to take place in the absence of aurora. As a consequence, the plasma density in the E-region was too low for useful PFISR measurements. All the local and global measures (Kp, AE, and IE indices, and the magnetometer data from Poker Flat) show no signs of magnetometer perturbations associated with aurora before or at the time of the launches. The launches occurred in the post-magnetic midnight local time (MLT) sector. The scientific objectives of the Super Soaker campaign and details of the rocket flights are discussed by Mesquita et al. (2020) and Collins et al. (2021). Three rockets were used, but only two carried TMA. These rockets were launched 30 minutes apart and each created a trail before and after the apogee between 80 and 160 km altitude.

4.3.2 Moderate geomagnetic activity (Kp∼3)

The JOULE II and HEX II campaigns represent the moderate geomagnetic activity category in this study. Both campaigns had a Kp∼3 at the time of their launches. The JOULE II campaign consisted of two pairs of rockets: two rockets with various instrumentation followed by two rockets with TMA released between 90 and 140 km altitude. The second Horizontal E-region Experiment (HEX), named HEX II, also consisted of four rockets. Details of these campaigns can be found in the work by Sangalli et al. (2009); Burchill et al. (2012) for JOULE II and Scott (2009) for HEX II. JOULE II launched into a stable auroral arc while HEX II launched into intense pulsating aurora.

Figures 4.1 and 4.2 show the background geomagnetic conditions for the launches of JOULE II and HEX II. These figures contain a summary of the geomagnetic conditions as rows: (a) the IMF, (b) global auroral electrojet indices (AE, AL, and AU), and (c) local auroral electrojet indices (IE, IL, and IU). These figures also show the summary of the PFISR observations and derived quantities in rows (d) F-region plasma velocity in geographic coordinates and (e) plasma density (N_e). The Pedersen Lorentz accelerations (push) in zonal and meridional directions are shown in rows (f) and (h). The Hall Lorentz accelerations (turn) in zonal and meridional directions are shown in rows (g) and (i). The vertical green line represents the launch time of the first rocket in the salvo.

Figures 4.1 and 4.2 show that the JOULE II and HEX II campaigns launched in different geomagnetic conditions. Both figures show evidence of a substorm that occurred after a southward turn of the IMF Bz between 45 and 60 minutes before the first launch. The substorm for JOULE II occurred in the post-magnetic midnight sector, while for HEX II it occurred in the pre-magnetic midnight sector. Row (e) shows a small deflection in the H component of the Poker Flat magnetometer in the hour before the first launch of both campaigns. Unfortunately, PFISR was turned off during the HEX II launches due to potential interference with the payload telemetry, which caused the gap in Figure 4.2. However, the F-region plasma velocity and Lorentz forcing for both campaigns were calculated in the period prior to the launches to assess the time history of the local forcing.

Row (e) in Figures 4.1 and 4.2 shows an increase in N_e for both campaigns, consistent

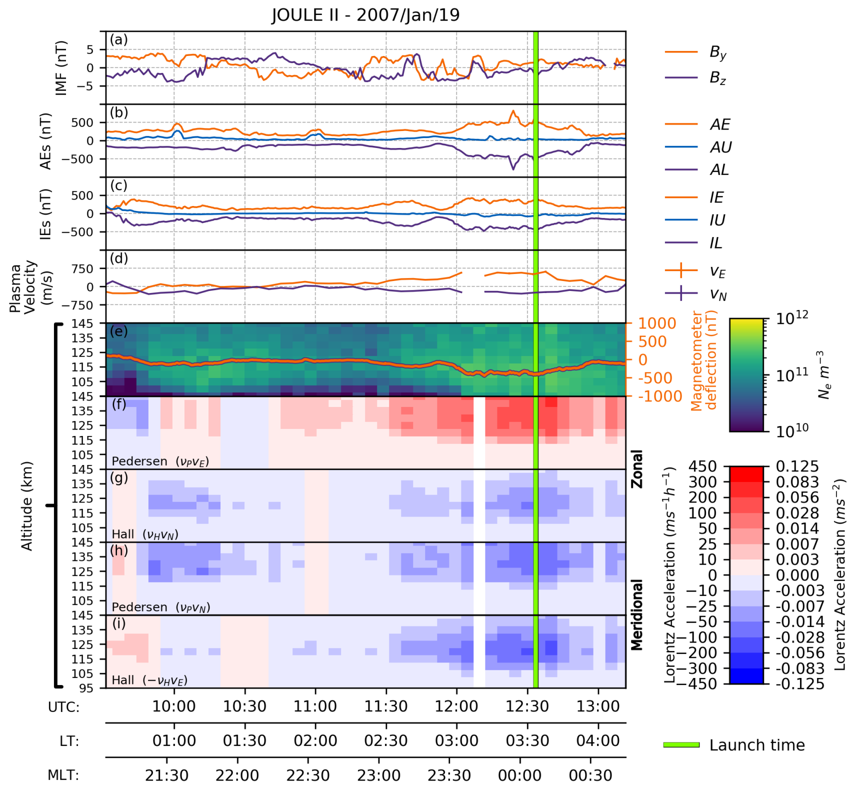

Figure 4.1: Summary of the background conditions for the JOULE II mission. Rows (a) interplanetary magnetic field (IMF) (B_y in orange and B_z in purple), (b) global auroral electrojet indices (AE in orange, AU in blue, and AL in purple), and (c) local auroral electrojet indices (IE in orange, IU in blue, and IL in purple) represent the geomagnetic conditions. The remaining rows display the PFISR measurements and derived parameters, which are (d) F-region plasma velocity (v_E and v_N in the zonal and meridional directions) and (e) the plasma density (N_e) with the H component of the Poker Flat magnetometer. Rows (f) and (h) represent the zonal and meridional Pedersen instantaneous Lorentz accelerations. Rows (g) and (i) represent the zonal and meridional Hall instantaneous Lorentz accelerations. The vertical green line represents the launch time of the first rocket.

with the substorm signature and linked to auroral activity directly above PFISR. The substorm perturbation can also be seen in Figure 4.1 row (d), where the plasma velocity progressively increases from approximately 100 to more than 750 ms^{-1} around the time of the first launch of the JOULE II campaign. The Pedersen Lorentz acceleration rows in both figures show a similarly broad peak in altitude in both zonal and meridional directions.

4.3.3 Strong geomagnetic activity (Kp$\sim$4)

The MIST and Auroral Jets campaigns represent the strong geomagnetic activity category, with Kp$\sim$4. The Mesospheric Inversion Layer Stratified Turbulence (MIST) campaign was conducted

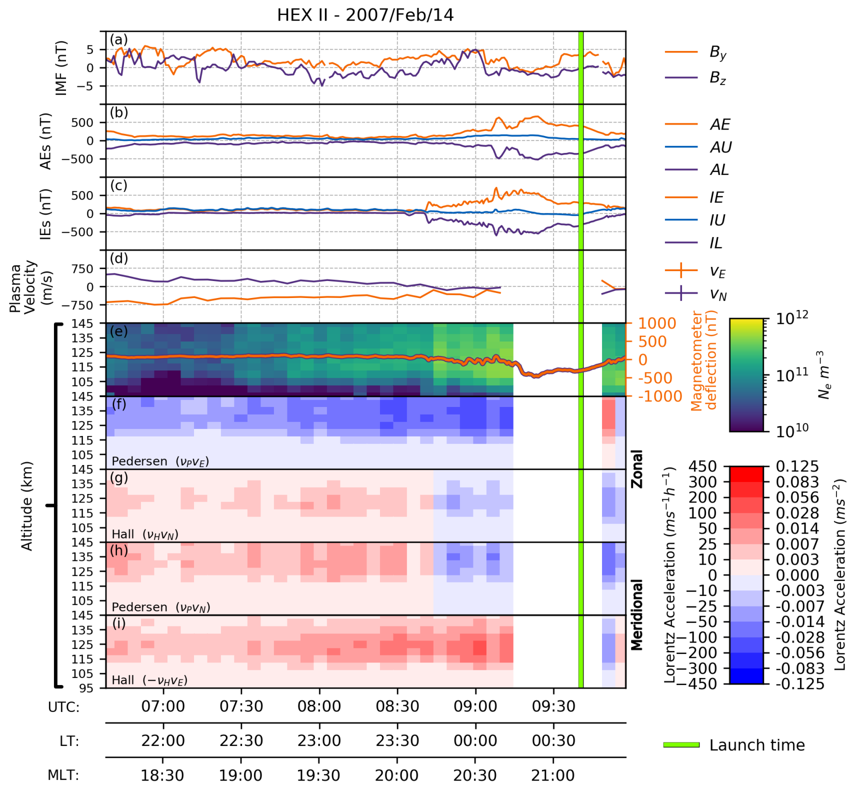

Figure 4.2: Summary of background conditions for the HEX II campaign, similar to Figure 4.1 for JOULE II.

with the Mesosphere and Lower Thermosphere Experiment (MTeX). Details of these launches can be found in the work of Lehmacher et al. (2018). The two rockets that carried TMA payloads will be referred to as MIST 1 and MIST 2. The rockets were launched 30 minutes apart and created trails between 90 and 150 km. The main goal of the Auroral Jets campaign was to study the neutral wind jets associated with stable auroral arcs, first observed by Larsen et al. (1995) and modeled by (Larsen and Walterscheid, 1995). It consisted of launching two rockets: one carrying instruments and one carrying TMA to generate trails between 90 and 180 km continuously before and after the apogee. Both campaigns launched into different stages of strong substorms. MIST 1 launched shortly after the break of an intense arc in pulsating aurora, MIST 2 launched in intense diffuse aurora, and Auroral Jets launched into a stable auroral arc.

Figures 4.3 and 4.4 display conditions of intense substorms around the launch times for MIST and Auroral Jets. Both campaigns launched rockets in the pre-magnetic midnight sector with large AE and IL indices, large magnetometer disturbances, and high plasma density associated with

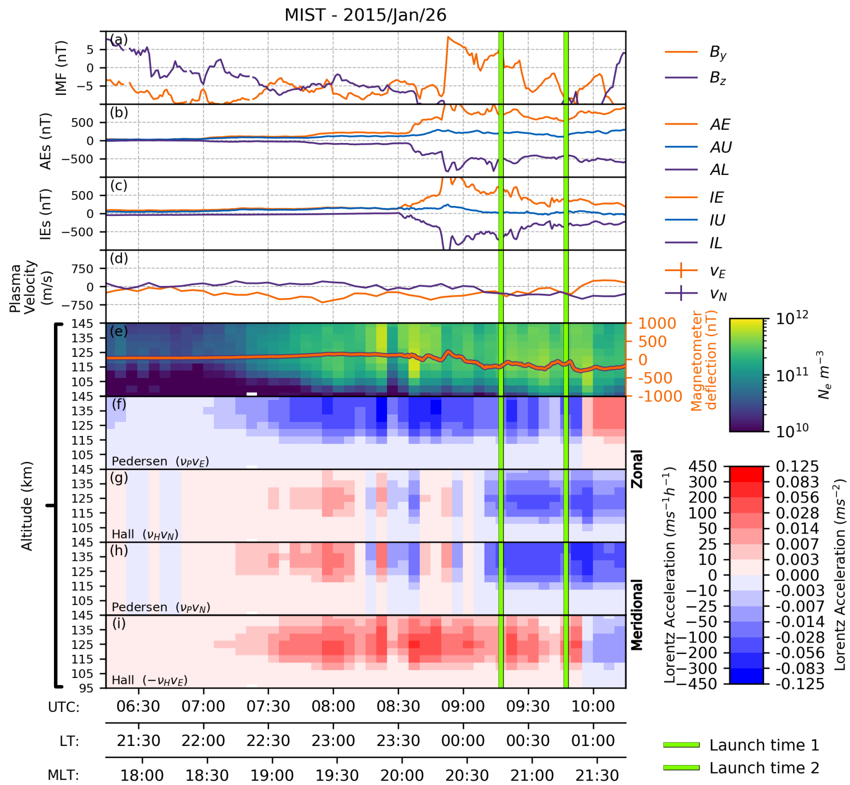

Figure 4.3: Summary of background conditions for the MIST campaign, similar to Figure 4.1 for JOULE II. The green lines represent both MIST 1 and MIST 2 launch times.

intense aurora. In Figure 4.3, there is clear evidence of a substorm with the IMF Bz turning south at 7:30 UT. In Figure 4.4 the southward turn of the IMF Bz occurs at 5:05 UT. The F-region plasma velocity in the hour that preceded the launches was approximately 550 ms^{-1} for MIST and 1400 ms^{-1} for Auroral Jets.

Even though the F-region plasma velocity was faster for Auroral Jets, the MIST campaign had higher plasma density, which resulted in similar Lorentz forcing for both campaigns. This acceleration was as broad in altitude as in the moderate cases; however, the peak one-hour mean Lorentz acceleration was approximately 200 ms^{-1}h^{-1} for MIST 1 and Auroral Jets in the zonal direction. In the meridional direction, it was 160 ms^{-1}h^{-1} for Auroral Jets and 90 ms^{-1}h^{-1} for MIST 1. The Lorentz acceleration was in similar directions, predominantly westward and northward, for MIST 1, MIST 2, and Auroral Jets. This behavior is expected for the MLT sector in which these rockets were launched.

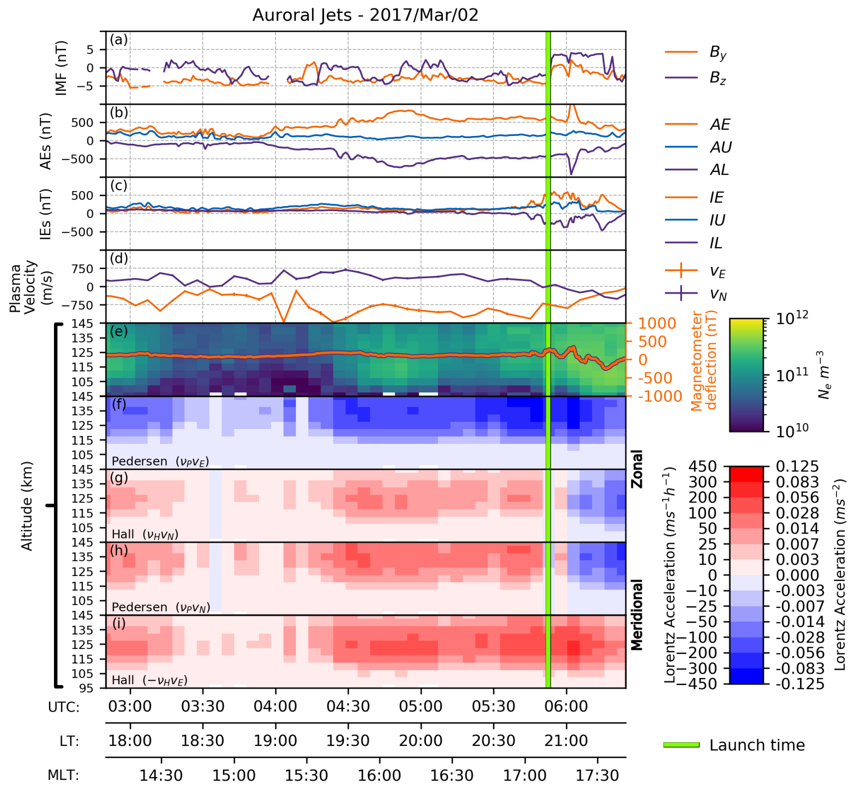

Figure 4.4: Summary of background conditions for the Auroral Jets campaign, similar to Figure 4.1 for JOULE II.

4.3.4 Measured winds

Figure 4.5 presents a collection of all the wind profiles analyzed in this paper. The figure displays profiles between 95 and 145 km altitude, which is the range of interest in this study. Based on the study of Larsen et al. (1997), we expect the wind profiles would vary based on geomagnetic conditions and local time of the measurements.

The quiet geomagnetic activity category (Super Soaker campaign) occurred in the absence of any noticeable activity and is shown in the top panel of Figure 4.5. The Super Soaker wind profiles show large shears discussed by Mesquita et al. (2020). The wind profiles for Super Soaker are consistent with the winds from the ARIA IV experiment, launched in quiet geomagnetic activity and presented by Larsen et al. (1997). Both ARIA IV and Super Soaker winds oscillate around zero and create a near circular hodograph above 100 km altitude. This behavior is consistent with upward propagating tides as described by Mikkelsen and Larsen (1991).

The moderate geomagnetic activity category (JOULE II and HEX II campaigns) is repre-

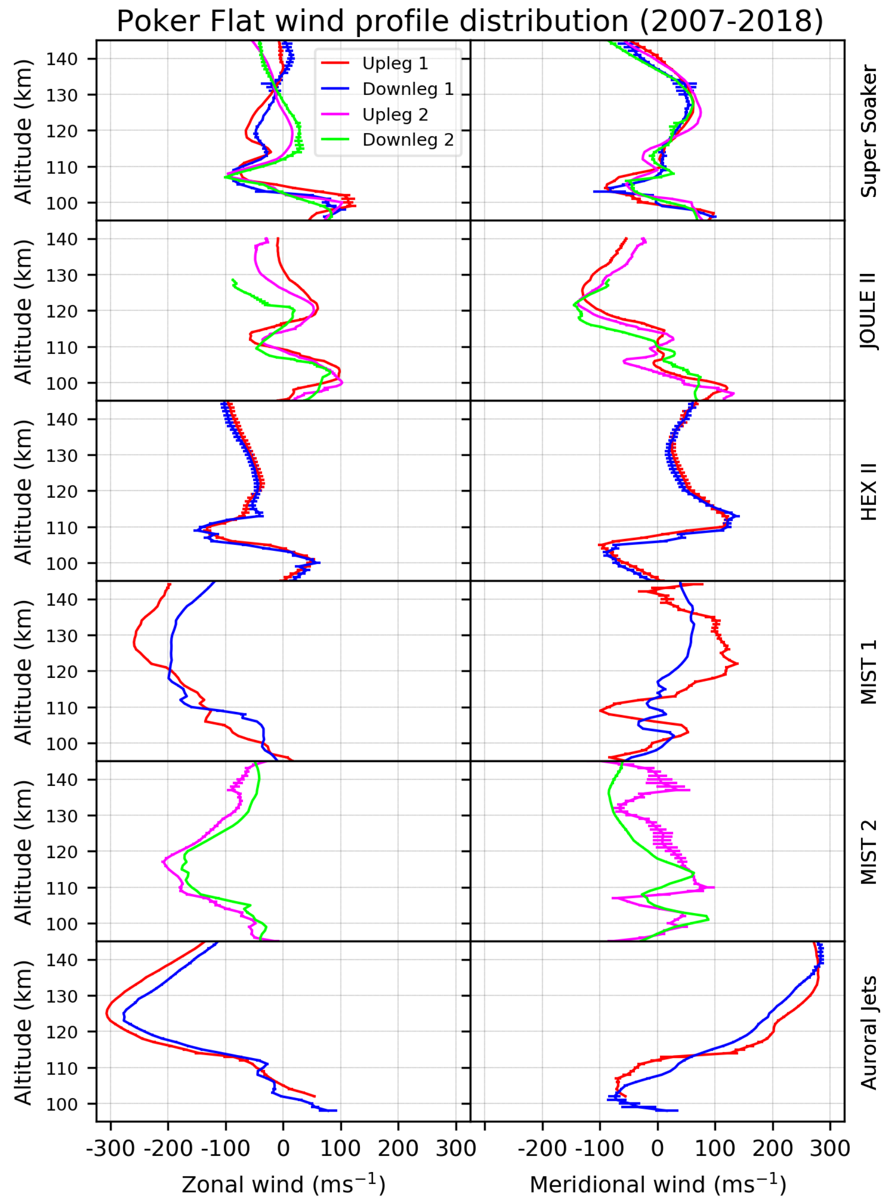

Figure 4.5: Summary of the zonal (left panel) and meridional (right panel) wind profiles measured during the Super Soaker, JOULE II, HEX II, MIST 1 and 2, and Auroral Jets campaigns. Upleg# (TMA released before the apogee) and Downleg# (TMA released after the apogee) (1 for the first rocket and 2 for the second rocket, less than an hour after the first launch). Launch times are shown in Table 4.1.

sented in the second and third panels of Figure 4.5. The winds within the available altitude range for JOULE II were predominantly southwestward above 110 km and in the same direction as the Lorentz forcing. This behavior is shown in Figure 4.1 and is expected in the post-magnetic midnight sector (Larsen et al., 1997). The HEX II campaign also exhibits behavior consistent with the Lorentz forcing, with northwestward winds and accelerations above 110 km, as shown in Figure 4.2. Below 110 km the winds of both campaigns are within the envelope of variability consistent with the Super Soaker campaign in the same altitude range.

The strong geomagnetic activity category is represented by MIST (both launches) and Auroral Jets in the bottom three panels of Figure 4.5. The measured wind profiles for MIST and Auroral Jets are consistent with winds of disturbed geomagnetic background conditions similar to the ARIA II experiment but in the pre-magnetic midnight sector (Mikkelsen et al., 1981; Larsen et al., 1997). The winds within the available altitude range for MIST and Auroral Jets were predominantly northwestward and in the same direction as the Lorentz forcing, as shown in Figures 4.3 and 4.4. The Auroral Jets and MIST campaigns had relatively similar Lorentz forcing with broad peaks in altitude. However, the Auroral Jets campaign had consistently faster winds in both zonal and meridional directions. The zonal and meridional winds for MIST peaked at 270 ms^{-1} and 150 ms^{-1} at 125 km. For Auroral Jets, the zonal winds peaked at 300 ms^{-1} at 125 km and meridional winds peaked at 280 ms^{-1} at 140 km.

Figure 4.6 summarizes our calculation of the accelerations based on the observations for all the launches discussed here. We show the meridional advective, Lorentz, Coriolis, centrifugal, and total accelerations. The advection terms were estimated using the method described in section 4.2.4. The measured instantaneous Lorentz acceleration profile was averaged for one hour preceding each launch as described in section 4.2.3. We calculated Coriolis and centrifugal accelerations using equations 4.3 and 4.4, and found in equations 2 and 3 of Mikkelsen et al. (1981).

In much of the altitude range displayed in Figure 4.6, the advective acceleration is small for both the quiet and moderate categories. However, for the strong category, the advection term can be large, indicating the nonlinear behavior of the wind patterns during active geomagnetic conditions (Mikkelsen and Larsen, 1983; Larsen and Mikkelsen, 1983). The strong category also has the largest total acceleration, approximately 0.16 ms^{-2}. The advection for the quiet geomagnetic activity category (Super Soaker) is truncated at 110 km because a Kelvin-Helmholtz instability (discussed by Mesquita et al., 2020) likely caused a localized peak in velocity that is non-representative of the wind gradient between the upleg and downleg. The maximum advective acceleration for the moderate geomagnetic activity category (JOULE II and HEX II) is <0.06 ms^{-2}. The maximum advective acceleration for the strong geomagnetic activity category (MIST and Auroral Jets) is >0.08

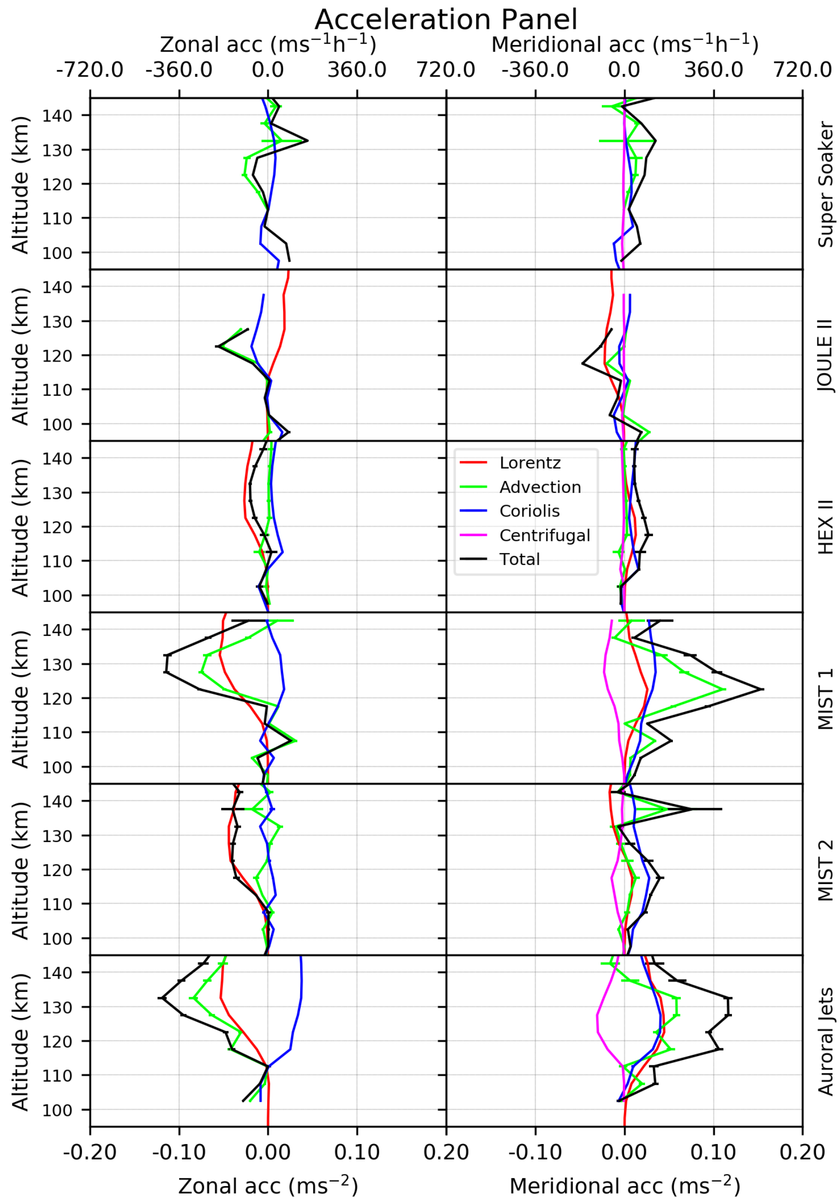

Figure 4.6: Acceleration panel from all of the campaigns: Super Soaker, JOULE II, HEX II, MIST (first and second launches separated), and Auroral Jets. The accelerations are: meridional advective (green), Lorentz (red), Coriolis (blue), centrifugal (pink), and total accelerations (black), in both ms^{-1}h^{-1} and ms^{-2}.

ms^{-2}. The averaged instantaneous Lorentz acceleration profiles exhibit a broad peak in altitude. The peak value for this acceleration becomes larger as geomagnetic activity increases (from JOULE II to Auroral Jets). The Lorentz acceleration experiences a southward reversal above 125 km between MIST 1 and MIST 2. The Coriolis and centrifugal accelerations are especially significant for the strong category, with similar magnitude but opposite signs. The Coriolis acceleration is slightly larger throughout the profiles in Figure 4.6.

The Rossby number (Ro) offers an insight into the importance of the nonlinear forcing terms in the neutral momentum equation. Mikkelsen and Larsen (1983) used the condition in which $Ro \ll 1$ to neglect the advection. They defined the Ro as

$$Ro = \frac{|\vec{u}|^2/L}{|\vec{u}|\,(2\Omega\sin\theta)}, \tag{4.5}$$

where L is 2000 km, the length of variation and typical radius of the oval for moderate and strong geomagnetic activity. The value for L is the same as used by (Larsen and Mikkelsen, 1983), which is a good approximate value for the aurora oval as estimated using the Global Ultraviolet Imager (GUVI) aboard the Thermosphere Ionosphere Mesosphere Energetics and Dynamics (TIMED) satellite (Zhang and Paxton, 2008). The latitude of the measurements is θ. We estimated the Ro for each of the campaigns by applying this approach. The result is displayed in Figure 4.7.

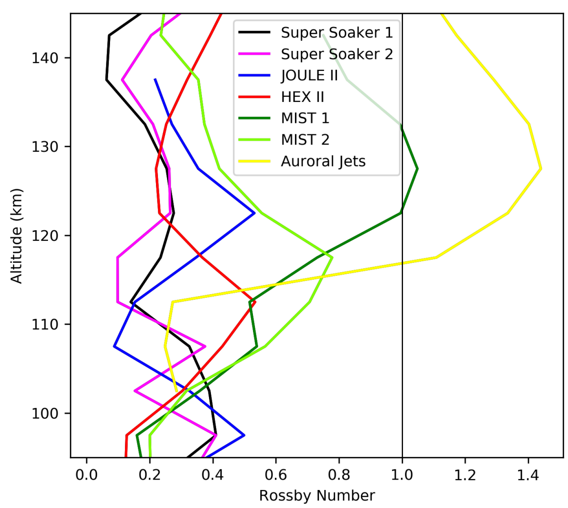

Figure 4.7: Rossby number for all the wind profiles discussed in this paper, calculated with equation 4.5 and the upleg wind profiles in Figure 4.5. First and second uplegs for the Super Soaker and MIST campaigns are displayed separately.

The Rossby number results show that the campaigns that took place in strong geomagnetic activity (MIST 1, MIST 2, and Auroral Jets) have larger Ro, as expected. While the quiet and moderate geomagnetic activity campaigns show a smaller Ro, none of the profiles in Figure 4.7 exhibits $Ro \ll 1$, with the exception of a few altitude ranges for the Super Soaker campaign (quiet category). Moderate category winds in the JOULE II and HEX II campaigns produced Ro peaking at approximately 0.5. By contrast, no measurement of $Ro \gg 1$ is present in Figure 4.7. Using equation 4.5 we estimate that a wind of 270 ms^{-1} would be required to produce $Ro = 1$ at the latitude of Poker Flat. MIST 1 and Auroral Jets are the only campaigns with $Ro > 1$: 1.05 for MIST 1 and 1.4 for Auroral Jets. The Ro maximum for these campaigns coincides with the peak in advection (Figure 4.6) at approximately 125 km.

4.4 Discussion

The results described above will be discussed in comparison with the modeling results of Mikkelsen et al. (1981) and Kwak and Richmond (2007), which will be referred to as MK81B and KR07. Since we are addressing the nonlinear terms, such as advective and centrifugal acceleration, in the neutral momentum equation, the full nonlinear model simulations presented by these studies are suitable points of comparison for the measured forcing terms. MK81B and its companion study by Mikkelsen et al. (1981) discuss accelerations during disturbed geomagnetic conditions, interpreting the results of two rocket launches from Poker Flat Research Range at 65.12 N and 147.43 W, the same location as our study. KR07 is a general circulation model with accelerations discussed in both winter (northern) and summer (southern) hemispheres at latitudes larger than 50 degrees, using the IMF as a proxy for geomagnetic activity. Their simulations with IMF Bz = -2 nT and -10 nT are similar to measurements presented in the results section of this paper for moderate and strong geomagnetic activity categories.

In the following subsections we discuss the effects of the centrifugal acceleration on the divergent (meridional) balance of forces by introducing the modified Coriolis parameter, and the behavior of Lorentz and advective accelerations in comparison with MK81B and KR07. We also discuss the winds, the Rossby number, and the balance of forces in the E-region in comparison with MK81B, KR07, and other studies.

4.4.1 Coriolis and centrifugal accelerations

The approximate balance between Coriolis and centrifugal (curvature acceleration in the meridional direction) accelerations was discussed by MK81B. They found that these accelerations balance to a high degree below 200 km; but the Coriolis acceleration is larger below 150 km. This behavior is clear in the meridional panel of Figure 4.6, where the Coriolis acceleration is larger than the centrifugal acceleration and in the opposite direction. The peaks in ratios between centrifugal and Coriolis accelerations are 0.20 (at 102 km - Super Soaker), 0.22 (at 102 km - JOULE II), 0.29 (at 107 km - HEX II), 0.65 (at 125 km - MIST 1), 0.52 (at 117 km - MIST 2), and 0.75 (at 127 km - Auroral Jets). As discussed by KR07, faster winds tend to increase the rotational radius of the flow (centrifugal or curvature radius), which limits the increase in the centrifugal acceleration, making the nonlinear centrifugal acceleration smaller than the Coriolis. Our results are consistent with those of KR07.

The balance between the Coriolis and centrifugal accelerations discussed above can affect the tendency of an air parcel to remain in the acceleration channel (aurora oval). This tendency was first discussed by Fuller-Rowell and Rees (1984), who concluded that Coriolis and centrifugal accelerations balance in the pre-magnetic midnight sector. MK81B addressed the tendency of a westward wind to generate turning in the poleward direction by comparing the Coriolis parameter (13.5×10^{-5}) to the peak Hall drag (4×10^{-5}). A similar argument was discussed in the modified geostrophy work by Larsen and Walterscheid (1995), who defined the modified Coriolis parameter ($f-\beta$, where β is the Hall drag). From equation 4.4, we see that the Coriolis parameter is further modified by the centrifugal acceleration. Therefore, the tendency of a zonal wind to turn in the meridional direction is associated with the Coriolis, centrifugal, and Hall ion-drag accelerations.

Similar to Larsen and Walterscheid (1995), we assess the tendency of an air parcel to converge poleward by redefining the modified Coriolis parameter (Ψ), which includes the centrifugal acceleration parameter. This coefficient can be written as

$$\Psi = f + u_E \frac{\tan\theta}{R} - \frac{\sigma_H B^2}{\rho}, \tag{4.6}$$

where the right-hand side features the Coriolis parameter, centrifugal acceleration parameter, and the Hall drag.

Given a westward wind, the Coriolis term tends to turn the wind poleward while the Hall term tends to turn the wind equatorward. This tendency, which was discussed by MK81B and KR07, was defined in the modified geostrophy study by Larsen and Walterscheid (1995). Comparing only these two terms for all of the campaigns, as done by MK81B and Maeda et al. (1999), we see an overall tendency to a poleward turn. However, with the inclusion of the centrifugal parameter in equation 4.6, we see that Ψ is nearly zero for the Auroral Jets campaign between 120 and 125 km, and negative for MIST 1 at 117.5 km and MIST 2 between 120 and 130 km. The nearly zero Ψ indicates a tendency for the winds to remain in the acceleration channel for Auroral Jets, while the negative Ψ for the MIST launches indicates a tendency for the winds to turn equatorward, in the altitudes mentioned above. Since a curvature radius in the zonal direction cannot be calculated from the available data, we cannot consider the effect of the zonal curvature acceleration parameter on the turning component in that direction.

The peak altitude of zonal winds can be explained by the modified Coriolis parameter Ψ and the balance between meridional Coriolis and centrifugal accelerations. The altitude in which the zonal winds peaked (Figure 4.5) coincides with the altitude of maximum ratios and minimum Ψ. This indicates that the channel of maximum acceleration has an altitude range related to the Hall drag and the Coriolis and centrifugal parameters. A modest Pedersen Lorentz force can generate fast winds as long as the Ψ tends to keep an air parcel in the acceleration channel.

4.4.2 Lorentz acceleration

The instantaneous Lorentz force is analyzed as the magnetospheric force with typical peak values and directions highlighted in Table 4.2, which shows that the maximum instantaneous Lorentz acceleration for each campaign increases with geomagnetic activity. This acceleration was predominantly in the northwest direction in the pre-magnetic midnight sector, as displayed in Figure 4.6 (HEX II, MIST, and Auroral Jets). However, it was in the southeast direction in the post-magnetic midnight sector (JOULE II).

Campaign	(MLT)	ILF (campaign)	Ion drag (KR07)
JOULE II	01:31	southeastward (0.02 ms^{-2})	northeastward (0.016 ms^{-2})
HEX II	22:22	northwestward (0.02 ms^{-2})	southwestward (0.003 ms^{-2})
MIST	22:10	northwestward (0.06 ms^{-2})	southwestward (0.003 ms^{-2})
Auroral Jets	18:40	northwestward (0.07 ms^{-2})	northwestward (0.001 ms^{-2})
MK81B N	17:30	northwestward (0.04 ms^{-2})	northwestward (0.001 ms^{-2})
MK81B S	17:30	northwestward (0.03 ms^{-2})	northwestward (0.001 ms^{-2})

Table 4.2: Launch time, peak instantaneous Lorentz forcing (ILF) direction and magnitude for JOULE II, HEX II, MIST (first launch), Auroral Jets, and modeled Lorentz force for both northern (MK81B N) and southern (MK81B S) profiles of Mikkelsen et al. (1981) compared with ion drag of Kwak and Richmond (2007) (KR07) for the corresponding MLT at 142 km between 60 and 70 degrees latitude (Figure 13 of that study). Our campaigns are displayed in order of geomagnetic activity from lowest (JOULE II) to highest (Auroral Jets).

Table 4.2 includes the peak zonal and meridional Lorentz forcing below 145 km from MK81B (interpreting measurements that occurred at ∼17:30 MLT), for both northern and southern profiles. Our observed Lorentz acceleration agrees with the direction (northwestward) of MK81B in the pre-magnetic midnight sector but with a larger magnitude. The Lorentz accelerations for MIST and Auroral Jets were approximately 1.5-2 times larger than the MK81B prediction.

The study by KR07 does not include the instantaneous Lorentz forcing; therefore, we compare our results to their modeled ion drag. The Lorentz acceleration directions in Figure 4.6 agree with the ion drag simulated by KR07 in the zonal direction (westward). In the meridional direction only our results for Auroral Jets agree with KR07, with a northward Lorentz forcing. The KR07 model predicted ion drag was approximately 0.002 (0.016) ms^{-2} in the pre-magnetic (post-magnetic) sector. These ion-drag magnitudes are generally smaller than our observations and the predictions of MK81B. That is likely due to the KR07 model choice to use an IMF Bz of -2 in the winter northern hemisphere. A different run of TIE-GCM in stronger geomagnetic activity in the northern hemisphere may improve this comparison, as inputting a larger southward turn of the IMF Bz would likely increase the oval radius and the area of enhanced plasma velocity. They discussed a case of IMF Bz of -10, which is closer to the values of MIST and Auroral Jets, but that simulation is displayed only in the southern summer hemisphere.

In our study, the shape of averaged instantaneous Lorentz acceleration profiles is broad in altitude because of different peak altitudes of the Hall and Pedersen conductivities. The peak altitude for this acceleration does not coincide with the peak altitude of the winds (see Figures 4.6 and 4.5). The Lorentz forcing profiles for both MK81B and ion drag for KR07 are also broad in altitude, which generally agrees with our results.

4.4.3 Advective acceleration

The meridional advective acceleration is analyzed with peak magnitude and directions in Table 4.3. This table shows that the peak magnitude of advective acceleration increases with geomagnetic activity. This acceleration was predominantly in the northwest direction for campaigns that occurred in the pre-magnetic midnight sector, as displayed in Figure 4.6 (HEX II, MIST, and Auroral Jets). However, it was purely in the westward direction for JOULE II, which took place in the post-magnetic midnight sector. The studies by MK81B and KR07 modeled both the zonal and meridional advective accelerations (horizontal or *h-advection*). KR07 included the curvature acceleration in the horizontal advection. They argued that the advection in their case is mainly centrifugal, indicating that the advection terms in equations 1 and 2 of their study were small. Here we compare our calculated advection with their h-advection. We acknowledge that separating their centrifugal and advective accelerations would likely improve the results of this comparison. Comparing the h-advection from KR07 and the centrifugal acceleration from Figure 4.6 results in generally good agreement (southward at 142 km).

Campaign	(MLT)	M-ADV (campaign)	H-ADV (KR07)
JOULE II	01:31	westward (0.05 ms^{-2})	southeastward (0.005 ms^{-2})
HEX II	22:22	northwestward (0.01 ms^{-2})	southwestward (0.018 ms^{-2})
MIST	22:10	northwestward (0.13 ms^{-2})	southwestward (0.018 ms^{-2})
Auroral Jets	18:40	northwestward (0.1 ms^{-2})	southwestward (0.008 ms^{-2})
MK81B (H-ADV) N	17:30	southeastward (0.03 ms^{-2})	southwestward (0.004 ms^{-2})
MK81B (H-ADV) S	17:30	southeastward (0.05 ms^{-2})	southwestward (0.004 ms^{-2})

Table 4.3: Launch time, peak meridional advective acceleration (M-ADV) direction and magnitude for JOULE II, HEX II, MIST (first launch), Auroral Jets, and modeled horizontal advection (H-ADV) for both northern (MK81B N) and southern (MK81B S) profiles of Mikkelsen et al. (1981) compared with Kwak and Richmond (2007) (KR07) for the corresponding MLT at 142 km between 60 and 70 degrees latitude (Figure 13 of that study). Our campaigns are displayed in order of geomagnetic activity from lowest (JOULE II) to highest (Auroral Jets).

In Table 4.3, we see differences between our observed advective acceleration and the directions and magnitudes of MK81B h-advection in the pre-magnetic midnight sector. Our data showed northwestward advective acceleration profiles with maximum magnitude at $\sim$0.13 ms^{-2} for MIST 1. By contrast, the MK81B model predicted h-advection profiles in the southeast direction with an estimated magnitude of <0.05 ms^{-2}, approximately half of our observed result. Our directional results agree with the h-advection simulation of KR07 in the zonal direction (westward). In the meridional direction our results (north) differ from those of KR07 (south). However, they explain that the advection is primarily the centrifugal acceleration, which is potentially the reason for this difference. The KR07 model predicted h-advection magnitude between 0.004 and 0.018 ms^{-2}. These values are comparable to the advective acceleration measured during HEX II, but are generally smaller compared with our other launches and the MK81B model.

The nonlinear advective acceleration becomes progressively more important with increasing geomagnetic activity, as shown in Table 4.4. The measured peak in advection for moderate activity (JOULE II and HEX II) is <0.05 ms^{-2}, while for strong activity (MIST and Auroral Jets) it is $\sim$0.1 ms^{-2}. The advection increases quadratically with the winds that are enhanced in stronger

Campaign	Category	*Ro* (altitude)	M-ADV (altitude)
JOULE II	Moderate	0.5 (122.5 km)	0.05 ms^{-2} (122.5 km)
HEX II	Moderate	0.5 (112.5 km)	0.02 ms^{-2} (112.5 km)
MIST	Strong	1.05 (127.5 km)	0.13 ms^{-2} (127.5 km)
Auroral Jets	Strong	1.4 (127.5 km)	0.1 ms^{-2} (132.5 km)
MK81B (H-ADV) N	Strong	1.34 (131 km)	0.03 ms^{-2} (131 km)
MK81B (H-ADV) S	Strong	1.13 (140 km)	0.05 ms^{-2} (140 km)

Table 4.4: Maximum Rossby number (*Ro*) and peak meridional advective acceleration with corresponding altitudes in km. The horizontal advection (H-ADV) was extracted from MK81B. Winds to calculate *Ro* for MK81B were extracted from Mikkelsen et al. (1981). MIST values correspond to the first launch (MIST 1).

geomagnetic activity. The altitude in which both the meridional advective acceleration and *Ro* peaked are the same, with the exception of Auroral Jets (off by ∼5 km).

Organizing the categories by *Ro* in Table 4.4 shows that the strong geomagnetic activity category is more nonlinear than the moderate category. MIST 1 and Auroral Jets (strong) have *Ro* of 1.05 and 1.4, and are the most nonlinear examples with advective accelerations ∼0.1 ms^{-2}. The geomagnetic conditions and resulting wind profiles for Auroral Jets were similar to the northern profile of Mikkelsen et al. (1981). Using equation 4.5 and the peak winds in Mikkelsen et al. (1981) (Figures 1 and 3 of that study) produces a *Ro* of 1.34, which is similar to the *Ro* of 1.4 for Auroral Jets. However, the h-advection in the MK81B model was significantly smaller than the meridional advective acceleration of Auroral Jets. While the wind profiles in the moderate geomagnetic activity category (JOULE II and HEX II) are less nonlinear than those in the strong category, the *Ro* condition for neglecting the advection ($Ro \ll 1$) was not met. For JOULE II, the *Ro* was 0.5 and advection of the zonal wind was 0.05 ms^{-1} just above 120 km. Winds measured by Cai et al. (2019) (∼125 ms $^{-1}$) and Tsuda et al. (2009) (∼225 ms $^{-1}$) result in *Ro* of 0.4 and 0.8. Neither study estimated the advective acceleration. The total acceleration measured by Cai et al. (2019) is on the same order of magnitude as the advective acceleration for MIST and Auroral Jets (∼0.1 ms^{-2}).

The relative direction between advection and ion drag is one of the differences between our results and the KR07 model. In the KR07 study, the advection rarely points in the same direction as the ion drag. This is different from our results (Figure 4.6), which show that the advection is often in the same direction as the Lorentz acceleration, though with different profiles. This behavior is consistent with that modeled by MK81B.

4.4.4 Wind comparison and balance of forces

We use the winds presented in Figure 4.5 to compare our observations with Figures 1 and 3 of Mikkelsen et al. (1981) and Figure 12 of KR07. The winds measured by Mikkelsen et al. (1981) agree with our observations in the pre-magnetic midnight sector (HEX II, MIST and Auroral Jets) and show winds mainly in the northwest direction at both 111 and 142 km. In the pre-magnetic midnight sector, KR07 predicted a change in direction of the wind vector from southeastward to westward at 111 km between 60 and 70 degrees latitude. At 142 km, the model generated predominantly westward winds in the same MLT sector. In the post-magnetic midnight sector, KR07 predicted winds predominantly northeastward at 111 km and southeastward at 142 km. By contrast, we observed westward winds at ∼111 km and southwest winds at ∼142 km for JOULE II (1:31 MLT). Mikkelsen et al. (1981) and MK81B do not include post-magnetic midnight measurements or simulations.

The balance of forcing terms modeled by KR07 and MK81B can be compared to the accelerations in our study. KR07 estimated that below 123 km, winds would be sustained by the balance among divergent (or convergent) accelerations: pressure gradient, Coriolis force, and Hall ion drag. We cannot estimate the pressure gradient with the available data in our study. However, we measured the Coriolis and Lorentz accelerations. Unlike KR07, we found that the meridional components of these forcing terms do not balance below 123 km (Figure 4.6). Above 123 km, KR07 predicted that winds would be sustained by a balance among divergent (or convergent) accelerations: pressure gradient, Coriolis force, and horizontal advection (mainly centrifugal). This is similar to the prediction of MK81B above ∼120 km (Figures 3 and 5 of that study). Our measurements differ from both KR07 and MK81B in this altitude range. We found that the meridional advective and Coriolis accelerations are predominantly complementary in the meridional direction. KR07 mentioned that their advection is mainly the centrifugal acceleration. We measured advective and centrifugal accelerations separately and found that they are mostly in opposite directions. However, the relative behavior between Coriolis and advection (assuming that it is the centrifugal acceleration) from KR07 is similar to ours in the meridional direction.

4.5 Conclusions

The purpose of this study is to investigate the terms in the E-region neutral momentum equation during different geomagnetic activity levels, with an emphasis on the meridional advective acceleration. We used sounding rocket observations to estimate neutral wind forcing in the E-region, including the meridional advection, at different geomagnetic activity levels. We used PFISR data to calculate the one-hour averaged instantaneous Lorentz forcing, and used the GPS rocket trajectory to calculate the advective, Coriolis, and centrifugal accelerations for each launch. We analyzed the impact of various geomagnetic activity levels on the forcing terms by separating them into three different categories (quiet, moderate, and strong) based on the Kp index.

We conclude that the meridional advection is an important, and at times can be the dominant, force during strong geomagnetic activity. We found that the meridional advection can be large above 120 km, depending on the geomagnetic conditions, and is mostly in the same direction as the Lorentz forcing but with a different vertical profile. We also found that the meridional advection increases in magnitude as geomagnetic activity increases.

We also conclude the following:

1. Our analysis of the modified Coriolis parameter Ψ showed that the interplay among Coriolis, centrifugal, and Hall accelerations caused an air parcel to either remain in the acceleration channel (120-125 km for Auroral Jets) or to turn equatorward (117.5 km for MIST 1 and 120-130 km for MIST 2) given the westward winds measured in strong geomagnetic activity. The near-zero modified Coriolis parameter causes an air parcel to remain in the acceleration channel for an extended period of time, therefore larger winds, such as those measured during the MIST and Auroral Jets campaigns, are possible due to the Pedersen Lorentz force.

2. The nonlinear centrifugal acceleration does not increase quadratically with the winds. This suggests that larger winds tend to increase the centrifugal radius, which decreases the acceleration, as discussed by KR07. This conclusion is also supported by the modified Coriolis parameter findings above.

3. We find wind measurements for both MIST and Auroral Jets are consistently in the same direction as the observations by Mikkelsen et al. (1981), which occurred in similar geomagnetic conditions in the pre-magnetic midnight sector. Although the instantaneous Lorentz forcing

for Auroral Jets and MIST was larger than that modeled by MK81B (1.5-2 times larger), the directions of the forces agree.

4.6 Acknowledgments

The wind data were obtained by Clemson in each case, but the overall principal investigators for the rocket launches discussed in this chapter were/are Dr. Irfan Azeem (Super Soaker), Dr. Miguel Larsen (MIST and JOULE II), Dr. Robert Pfaff (Auroral Jets), Dr. John Craven, and Dr. Mark Conde (HEX II).

4.7 Appendix: Error analysis

We can assume that each of the measurements presented in this paper have their associated error. These errors are defined as

1. $\sigma_{u_j^{XX}}$: Sounding rocket wind measurement errors with subscript $j = N$ or E in meridional and zonal directions. The superscript XX refers to either UP or DO, which mean before and after apogee, or upleg and downleg. The error estimation comes from the covariance of the linear fitting of latitude and longitude versus time. The resulting error is associated with the fitting procedure and the distance of closest approach as described by Larsen et al. (1998) and in section 4.2.2 of this paper;

2. σ_{v_j}: PFISR F-region plasma velocity measurement errors. The estimation of these errors is described by Heinselman and Nicolls (2008); and

3. σ_{σ_i}: PFISR-derived conductivities. The subscript $i = P$ or H for Pedersen and Hall conductivities. The error estimation for these parameters is associated with the plasma density measurement errors, which is inversely proportional to the signal-to-noise ratio of the measurements. The error is directly proportional to the plasma density N_e, assuming that in first order, the main source of error is the plasma density error.

For the advective accelerations, which are defined by equations 4.3 and 4.4, and using the rules for error propagation discussed in Bevington and Robinson (2003), the uncertainties can be be written as

$$\sigma_{AD}^{j} = \left\{ AD_j^2 \left[\left(\frac{\sigma_{u_N^{DO}}}{u_N^{DO}/R} \right)^2 + \sigma_j^2 \right] \right\}^{1/2}, \tag{4.7}$$

$$\sigma_j^2 = \frac{\sigma_{u_j^{DO}}^2 + \sigma_{u_i^{\mathrm{UP}}}^2}{A_j}, \tag{4.8}$$

and

$$A_j = \left(\frac{u_j^{DO} - u_j^{\mathrm{UP}}}{\theta_{DO} - \theta_{UP}} \right), \tag{4.9}$$

where $j = N$ or E.

Here we define the Pedersen and Hall conductivities as

$$\sigma_P = e^2 N_e \left[\frac{\nu_{in}}{m_i\left(\nu_{in}^2 + \Omega_i^2\right)} + \frac{\nu_{en}}{m_e\left(\nu_{en}^2 + \Omega_e^2\right)} \right] \tag{4.10}$$

and

$$\sigma_H = e^2 N_e \left[\frac{\Omega_i}{m_i\left(\nu_{in}^2 + \Omega_i^2\right)} - \frac{\Omega_e}{m_e\left(\nu_{en}^2 + \Omega_e^2\right)} \right]. \tag{4.11}$$

as given by Paschmann et al. (2012), where e is the electron charge, and N_e is the electron number density measured by the ISR.

Also, with s being the species for electrons or ions, we have that m_s is the species mass, ν_{sn} is the *species*-neutral collision frequencies, and Ω_s is the cyclotron frequency for the species. We used NRLMSISE-00 Atmosphere Model to determine the neutral atmospheric parameters necessary to calculate the values for equations 4.10 and 4.11, although this neutral mass density model presents a potential source of error. For simplicity we ignore this potential error. A significant source of uncertainty in the estimation of the conductivities is the measurement error associated with N_e; and we can calculate

$$\sigma_{\sigma_i} = \sigma_i \frac{\sigma_{N_e}}{N_e} \tag{4.12}$$

where the subscript $i = P$ or H, for Pedersen or Hall conductivities.

Using these results we can estimate the instantaneous Lorentz acceleration error. For the sake of simplicity, we rewrite equation 4.1 as

$$LF_E = \alpha v_E + \beta v_N \tag{4.13}$$

and

$$LF_N = \alpha v_N - \beta v_E, \tag{4.14}$$

where $\alpha = \sigma_P B^2/\rho$ and $\beta = \sigma_H B^2/\rho$.

The error for each of conductivity terms can be written as

$$\sigma_k = \frac{\sigma_{\sigma_i B^2}}{\rho}, \tag{4.15}$$

where $k = \alpha$ or β, which are related to Pedersen or Hall conductivities following the definitions stated above.

We can then write the instantaneous Lorentz acceleration error in both zonal and meridional directions as

$$\sigma_{LF_\phi} = \left\{ \alpha^2 v_E^2 \left[\left(\frac{\sigma_\alpha}{\alpha} \right)^2 + \left(\frac{\sigma_{v_E}}{v_E} \right)^2 \right] + \beta^2 v_N^2 \left[\left(\frac{\sigma_\beta}{\beta} \right)^2 + \left(\frac{\sigma_{v_N}}{v_N} \right)^2 \right] \right\}^{1/2}, \tag{4.16}$$

and

$$\sigma_{LF_\theta} = \left\{ \alpha^2 v_N^2 \left[\left(\frac{\sigma_\alpha}{\alpha} \right)^2 + \left(\frac{\sigma_{v_N}}{v_N} \right)^2 \right] + \beta^2 v_E^2 \left[\left(\frac{\sigma_\beta}{\beta} \right)^2 + \left(\frac{\sigma_{v_E}}{v_E} \right)^2 \right] \right\}^{1/2}. \tag{4.17}$$

Chapter 5

Summary and Future Work

The following subsections summarize the contributions of each of the papers included in this dissertation and suggest possible future work in each area. As these phenomena are widely different in nature, detailed conclusions and future work discussions are presented for each chapter separately.

This dissertation addresses thermospheric phenomena that impact the overall dynamics and energy transfer in Earth's atmosphere. The specific purpose of each study is to address the following scientific questions:

1. What are the characteristics of the mid-latitude midnight temperature maximum (MTM)?
2. What is the triggering mechanism of the Kelvin-Helmholtz instability (KHI) in statically stable regions and how does it evolve?
3. How does geomagnetic activity affect the vertical distribution of forces (including advection) and the modified Coriolis parameter in the E-region?

5.1 Chapter 2

Chapter 2 identified the occurrence of the MTM in mid-latitude thermosphere, farther north than previously observed, and confirmed modeling results. Both MTM peaks were observed as far north as 44.4° N. This indicates that the MTM peaks penetrate further in latitude than previously observed. The climatology of the mid-latitude MTM showed that while it was more often observed during the summer months, the secondary peak was more prominent during the winter months.

Future work should investigate whether the secondary MTM peak occurs more often in the winter months because of the nature of the constructive interference between the tidal components or because winter nights are longer and allow enough time after the evening twilight to observe the secondary peak.

Plans to relocate the NATION network further west were discussed in the past but were not implemented. This move would provide better quality data year-round due to the clear skies found in the drier western region. Further work could be done on this data set to address the characteristics of the MTM peak and its correlation with tidal modes through an investigation using whole atmospheric models. This study should aim to address the day-to-day variability of the MTM as well as the timing of the feature.

5.2 Chapter 3

Chapter 3 detailed observations of the KHI in the low thermosphere, a statically stable region. This proves that the KHI in this region is triggered by a different mechanism than in the mesosphere. In the thermosphere, where the temperature increases with altitude, large and long-lasting shears are necessary to generate a KHI; while in the mesosphere, where the temperature decreases with altitude, the shears can be more modest and short-lived. The Super Soaker observations, which took place in Alaska during quiet geomagnetic conditions, characterized the KHI features between 100 and 105 km in more detail than previously reported. The KHI and subsequent turbulent dispersion of the TMA occurred above the turbopause, estimated to be at ~99 km altitude.

The observation of the KHI breakdown agrees with the previous DNS analysis, with the feature breaking down into turbulence from the edges inward. Observation of the KHI in this altitude range represents a plausible explanation for the vertical transport of atomic oxygen between the mesosphere and thermosphere, which has been observed but previously was attributed to the propagation of gravity waves through the medium.

Future work should aim to investigate other wind profiles such as those presented in Figure 1.4 and those produced by the Michelson Interferometer for Global High-resolution Thermospheric Imaging (MIGHTI) instrument, which is on the Ionospheric Connection Explorer (ICON) satellite. An investigation of the Richardson number should give an indication on how often the low thermosphere becomes favorable to the production of KHIs. While the KHI observed during the Super Soaker campaign was only visible in the region where the TMA was deployed, the true horizontal extent of the KHI could be larger. Therefore a different investigation should make use of the direct number simulations technique, similar to the work of Hecht et al. (2021) and Fritts et al. (2021), to provide further insight into the development and coverage of the KHI observed during the Super Soaker campaign as well other thermospheric KHI observations, such as those done by Larsen et al. (2005) and Hysell et al. (2012).

5.3 Chapter 4

Chapter 4 illustrates the behavior of the Coriolis, centrifugal, Lorentz, and advective accelerations in different geomagnetic activity levels. While previous studies modeled the advective acceleration, the calculation of this term from sounding rocket observations showed that it can be dominant in strong geomagnetic activity above 120 km. The analysis of the modified Coriolis parameter (Ψ) reveals that in strong geomagnetic activity, an air parcel tends to stay in the acceleration channel (auroral oval) for long periods of time in the pre-magnetic midnight sector. This explains why winds can be large in periods of enhanced geomagnetic activity in the pre-magnetic midnight sector.

Observations of the advection are different from the Kwak and Richmond (2007) model but similar to the Mikkelsen et al. (1981) model. The calculated instantaneous Lorentz force results in Chapter 4 agree with that of Mikkelsen et al. (1981). Centrifugal and Coriolis forces approximately balance in the low thermosphere during strong geomagnetic activity, similar to the Mikkelsen et al. (1981) model.

The calculation of the advective acceleration should become a standard procedure in the triangulation of future TMA releases. It should also be applied to the database of rocket campaigns whenever the original images are available. These images could be used to produce TMA positions and winds to calculate the advection. The GPS rocket tracks are not necessary to estimate this acceleration, but could increase the precision of the calculation when available. The images from the AZURE campaign, which took place in Norway in April 2019, should also be used to calculate the three-dimensional winds and the full advective acceleration in the low thermosphere. The releases from that campaign were separated enough that the vertical winds could be estimated. The TMA release configuration was such that the winds could be estimated in different locations along the same latitude and longitude.

In-situ measurements of the winds should also be used to calculate the advection. The deployment of THz limb sounders (TLS) similar to what was discussed by Wu et al. (2016) also shows a promising source of advective acceleration estimation in the E-region.

Using models to interpret observations is not new, but further model comparison should also be done. The models by Mikkelsen and Larsen (1993) and Kwak and Richmond (2007) should be run to the specific conditions of the campaigns discussed in Chapter 4. Driving the TIE-GCM with Weimer model (Weimer, 1996) using IMF measurements for the campaigns or the Super Dual Auroral Radar Network (Greenwald et al., 1995, SuperDARN by) convection patterns could produce a better comparison.

Bibliography

Akmaev, R. A. (2011). Whole atmosphere modeling: Connecting terrestrial and space weather. *Rev. Geophys.*, 49(4). RG4004.

Akmaev, R. A., Wu, F., Fuller-Rowell, T. J., and Wang, H. (2009). Midnight temperature maximum (mtm) in whole atmosphere model (wam) simulations. *Geophys. Res. Lett.*, 36(7). L07108.

Anderson, C., Conde, M., and McHarg, M. G. (2012). Neutral thermospheric dynamics observed with two scanning Doppler imagers: 3. Horizontal wind gradients. *Journal of Geophysical Research: Space Physics*, 117(A5):n/a–n/a.

Ångström, A. J. (1869). *Recherches sur le spectre solaire*. Schultz.

Appleton, E. V. and Green, A. L. (1930). On some short-wave equivalent height measurements of the ionized regions of the upper atmosphere. *Proceedings of the Royal Society of London. Series A, Containing Papers of a Mathematical and Physical Character*, 128(807):159–178.

Arduini, C., Broglio, L., and Ponzi, U. (1993). Drag balance measurements in the san marco d/l mission. *Advances in Space Research*, 13(1):185 – 200.

Arduini, C., Laneve, G., and Herrero, F. A. (1997). Local time and altitude variation of equatorial thermosphere midnight density maximum (MDM): San Marco drag balance measurements. *Geophys. Res. Lett.*, 24(4):377–380.

Arduini, C., Ponzi, U., Agneni, A., Laneve, G., and Mortari, D. (1992). San marco v utafiti drag balance instrument data processing and accuracy assessment. *CRA Internal Document*, (502).

Aruliah, A. L. and Griffin, E. (2001). Evidence of meso-scale structure in the high-latitude thermosphere. *Annales Geophysicae*, 19(1):37–46.

Azeem, S. I., Crowley, G., Noto, J., Kerr, R. B., Kapali, S., Riccobono, J., and Migliozzi, M. (2012). Midnight Temperature Maximum Observations Over Millstone Hill. *AGU Fall Meeting Abstracts*.

Bamgboye, D. K. and McClure, J. P. (1982). Seasonal variation in the occurrence time of the equatorial midnight temperature bulge. *Geophysical Research Letters*, 9(4):457–460.

Barbulescu, M. and Erdélyi, R. (2018). Magnetoacoustic waves and the kelvin–helmholtz instability in a steady asymmetric slab. *Solar Physics*, 293(6):86.

Bates, D. R. (1950). A suggestion regarding the use of rockets to vary the amount of atmospheric sodium. *Journal of Geophysical Research*, 55(3):347–349.

Baumgarten, G. and Fritts, D. C. (2014). Quantifying Kelvin-Helmholtz instability dynamics observed in noctilucent clouds: 1. Methods and observations. *Journal of Geophysical Research: Atmospheres*, 119(15):9324–9337.

Behnke, R. A. and Harper, R. M. (1973). Vector measurements of F region ion transport at Arecibo. *J. Geophys. Res.*, 78(34):8222–8234.

Bevington, P. R. and Robinson, D. K. (2003). *Data reduction and error analysis for the physical sciences; 3rd ed.* McGraw-Hill, New York, NY.

Bilitza, D. (2018). Iri the international standard for the ionosphere. *Advances in Radio Science*, 16:1–11.

Billett, D. D., McWilliams, K. A., and Conde, M. G. (2020). Colocated Observations of the E and F Region Thermosphere During a Substorm. *Journal of Geophysical Research: Space Physics*, 125(11).

Bishop, R. L., Larsen, M. F., Hecht, J. H., Liu, A. Z., and Gardner, C. S. (2004). TOMEX: Mesospheric and lower thermospheric diffusivities and instability layers. *J. Geophys. Res.*, 109(D2):–.

Brekke, A., Doupnik, J. R., and Banks, P. M. (1973). A preliminary study of the neutral wind in the auroral E region . *Journal of Geophysical Research*, 78(34):8235–8250.

Brekke, A., Nozawa, S., and Sparr, T. (1994). Studies of the E region neutral wind in the quiet auroral ionosphere. *Journal of Geophysical Research*, 99(A5):8801.

Burchill, J. K., Clemmons, J. H., Knudsen, D. J., Larsen, M., Nicolls, M. J., Pfaff, R. F., Rowland, D., and Sangalli, L. (2012). High-latitudeeregion ionosphere-thermosphere coupling: A comparative study using in situ and incoherent scatter radar observations. *Journal of Geophysical Research: Space Physics*, 117(A2).

Cai, L., Oyama, S., Aikio, A., Vanhamäki, H., and Virtanen, I. (2019). Fabry-perot interferometer observations of thermospheric horizontal winds during magnetospheric substorms. *Journal of Geophysical Research: Space Physics*, 124(5):3709–3728.

Chapman, S. (1950). Upper atmospheric nomenclature. *Journal of Geophysical Research (1896-1977)*, 55(4):395–399.

Chau, J. L., Urco, J. M., Avsarkisov, V., Vierinen, J. P., Latteck, R., Hall, C. M., and Tsutsumi, M. (2020). Four-Dimensional Quantification of Kelvin-Helmholtz Instabilities in the Polar Summer Mesosphere Using Volumetric Radar Imaging. *Geophysical Research Letters*, 47(1).

Colerico, M. and Mendillo, M. (2002). The current state of investigations regarding the thermospheric midnight temperature maximum (MTM). *J. Atmos. Sol-Terr. Phy.*, 64(12):1361–1369.

Colerico, M. J., Mendillo, M., Fesen, C. G., and Meriwether, J. (2006). Comparative investigations of equatorial electrodynamics and low-to-mid latitude coupling of the thermosphere-ionosphere system. *Annales Geophysicae*, 24(2):503–513.

Collins, R. L., Stevens, M. H., Azeem, I., Taylor, M. J., Larsen, M. F., Williams, B. P., Li, J., Alspach, J. H., Pautet, P., Zhao, Y., and Zhu, X. (2021). Cloud Formation from a Localized Water Release in the Upper Mesosphere: Indication of Rapid Cooling. *Journal of Geophysical Research: Space Physics*, pages 1–21.

Conde, M., Craven, J. D., Immel, T., Hoch, E., Stenbaek-Nielsen, H., Hallinan, T., Smith, R. W., Olson, J., Sun, W., Frank, L. A., and Sigwarth, J. (2001). Assimilated observations of thermospheric winds, the aurora, and ionospheric currents over Alaska. *Journal of Geophysical Research: Space Physics*, 106(A6):10493–10508.

Cushman-Roisin, B. and Beckers, J.-M. (2011). *Introduction to geophysical fluid dynamics: physical and numerical aspects.* Academic press.

Davis, T. N. and Sugiura, M. (1966). Auroral electrojet activity index ae and its universal time variations. *Journal of Geophysical Research*, 71(3):785–801.

Drob, D. P., Emmert, J. T., Meriwether, J. W., Makela, J. J., Doornbos, E., Conde, M., Hernandez, G., Noto, J., Zawdie, K. A., McDonald, S. E., Huba, J. D., and Klenzing, J. H. (2015). An update to the Horizontal Wind Model (HWM): The quiet time thermosphere. *Earth and Space Science*, 2(7):301–319.

Faivre, M., Meriwether, J., Fesen, C., and Biondi, M. (2006). Climatology of the midnight temperature maximum phenomenon at arequipa, peru. *J. Geophys. Res.: Space Physics*, 111(A6).

Figueiredo, C. A. O. B., Buriti, R. A., Paulino, I., Meriwether, J. W., Makela, J. J., Batista, I. S., Barros, D., and Medeiros, A. F. (2017). Effects of the midnight temperature maximum observed in the thermosphere–ionosphere over the northeast of brazil. *Annales Geophysicae*, 35(4):953–963.

Fisher, D. (2013). *Three-dimensional wind measurements and modeling using a bi-static Fabry-Perot interferometer system in Brazil.* Master thesis, University of Illinois at Urbana-Champaign.

Forbes, J. M. (1995). Tidal and planetary waves. *Geophysical Monograph Series*, 87:67–87.

Fritts, D. C., Baumgarten, G., Wan, K., Werne, J., and Lund, T. (2014). Quantifying Kelvin-Helmholtz instability dynamics observed in noctilucent clouds: 2. Modeling and interpretation of observations. *Journal of Geophysical Research: Atmospheres*, 119(15):9359–9375.

Fritts, D. C., Wieland, S. A., Lund, T. S., Thorpe, S. A., and Hecht, J. H. (2021). Kelvin-Helmholtz Billow Interactions and Instabilities in the Mesosphere Over the Andes Lidar Observatory: 2. Modeling and Interpretation. *Journal of Geophysical Research: Atmospheres*, 126(1).

Fuller-Rowell, T. J. (2013). Physical characteristics and modeling of earth's thermosphere. *Geophysical Monograph Series*, 201:13–27.

Fuller-Rowell, T. J. and Rees, D. (1984). Interpretation of an anticipated long-lived vortex in the lower thermosphere following simulation of an isolated substorm. *Planetary and Space Science*, 32(1):69–85.

Gong, Y., Zhou, Q., Zhang, S., Aponte, N., and Sulzer, M. (2016). An incoherent scatter radar study of the midnight temperature maximum that occurred at Arecibo during a sudden stratospheric warming event in January 2010. *J. Geophys. Res. - Space*, 121(6):5571–5578. 2016JA022439.

Greenspan, J. (1966). Synoptic description of the 6300 Å nightglow near 78 west longitude. *J. Atmos Terr. Phys.*, 28(8):739–745.

Greenwald, R., Baker, K., Dudeney, J., Pinnock, M., Jones, T., Thomas, E., Villain, J.-P., Cerisier, J.-C., Senior, C., Hanuise, C., et al. (1995). Darn/superdarn. *Space Science Reviews*, 71(1-4):761–796.

Harding, B. J. (2017). *Midlatitude thermospheric wind and temperature: networked Fabry-Perot interferometer observations and radiative transfer modeling.* PhD dissertation, University of Illinois at Urbana-Champaign.

Harding, B. J., Gehrels, T. W., and Makela, J. J. (2014). Nonlinear regression method for estimating neutral wind and temperature from fabry–perot interferometer data. *Appl. Opt.*, 53(4):666–673.

Harding, B. J., Makela, J. J., and Meriwether, J. W. (2015). Estimation of mesoscale thermospheric wind structure using a network of interferometers. *Journal of Geophysical Research: Space Physics*, 120(5):3928–3940.

Harding, B. J., Makela, J. J., Qin, J., Fisher, D. J., Martinis, C. R., Noto, J., and Wrasse, C. M. (2017). Atmospheric scattering effects on ground-based measurements of thermospheric vertical wind, horizontal wind, and temperature. *Journal of Geophysical Research: Space Physics*, 122(7):7654–7669.

Hays, P. B., Carignan, G., Kennedy, B. C., Shepherd, G. G., and Walker, J. C. G. (1973). The visible-airglow experiment on atmosphere explorer. *Radio Science*, 8(4):369–377.

Hecht, J. H. (2005). Maui Mesosphere and Lower Thermosphere (Maui MALT) observations of the evolution of Kelvin-Helmholtz billows formed near 86 km altitude. *Journal of Geophysical Research*, 110(D9):D09S10.

Hecht, J. H., Fritts, D. C., Gelinas, L. J., Rudy, R. J., Walterscheid, R. L., and Liu, A. Z. (2021). Kelvin-Helmholtz Billow Interactions and Instabilities in the Mesosphere Over the Andes Lidar Observatory: 1. Observations. *Journal of Geophysical Research: Atmospheres*, 126(1).

Heinselman, C. J. and Nicolls, M. J. (2008). A Bayesian approach to electric field and E -region neutral wind estimation with the Poker Flat Advanced Modular Incoherent Scatter Radar . *Radio Science*, 43(5):n/a–n/a.

Hernandez, G. and Roble, R. (1976). Direct measurements of nighttime thermospheric winds and temperatures, 1. seasonal variations during geomagnetic quiet periods. *Journal of Geophysical Research*, 81(13):2065–2074.

Herrero, F., Mayr, H., Spencer, N., Hedin, A., and Fejer, B. G. (1985). Interaction of zonal winds with the equatorial midnight pressure bulge in the earth's thermosphere: Empirical check of momentum balance. *Geophysical research letters*, 12(8):491–494.

Herrero, F. and Spencer, N. (1982). On the horizontal distribution of the equatorial thermospheric midnight temperature maximum and its seasonal variation. *Geophys. Res. Lett.*, 9(10):1179–1182.

Hickey, D. A., Martinis, C. R., Erickson, P. J., Goncharenko, L. P., Meriwether, J. W., Mesquita, R., Oliver, W. L., and Wright, A. (2014). New radar observations of temporal and spatial dynamics of the midnight temperature maximum at low latitude and midlatitude. *J. Geophys. Res. - Space*, 119(12):10,499–10,506. 2014JA020719.

Hurd, L., Larsen, M. F., and Liu, A. Z. (2009). Overturning instability in the mesosphere and lower thermosphere: Analysis of instability conditions in lidar data. *Annales Geophysicae*, 27(7):2937–2945.

Hysell, D. L., Nossa, E., Larsen, M. F., Munro, J., Smith, S., Sulzer, M. P., and González, S. A. (2012). Dynamic instability in the lower thermosphere inferred from irregular sporadic E layers. *Journal of Geophysical Research: Space Physics*, 117(A8):n/a–n/a.

Ingersoll, J. (2008). A Regularization Technique for the Analysis of Photographic Data Used in Chemical Release Wind Measurements. Master's thesis, Clemson University.

Johnson, R. (1990). Lower-thermospheric neutral winds at high latitude determined from incoherent scatter measurements: a review of techniques and observations. *Advances in Space Research*, 10(6):261–275.

Johnson, R., Luhmann, J., Wickwar, V., and Roble, R. (1987). Lower-Thermospheric Winds at High Latitude. *Lower-Thermospheric Winds at High Latitude*, 5A(6):383–404.

Kázmér, M. and Timár, G. (2016). The first scientific description of aurora borealis: the 10 September 1580 event in Transylvania, recorded by Marcello Squarcialupi. *Geoscience Letters*, 3(1).

Kelley, M. C. (2009). *The Earth's ionosphere: plasma physics and electrodynamics*. Academic press.

Kelly, J. D. and Heinselman, C. J. (2009a). Initial results from Poker Flat Incoherent Scatter Radar (PFISR). *Journal of Atmospheric and Solar-Terrestrial Physics*, 71(6-7):635.

Kelly, J. D. and Heinselman, C. J. (2009b). Initial results from Poker Flat Incoherent Scatter Radar (PFISR). *Journal of Atmospheric and Solar-Terrestrial Physics*, 71(6-7):635.

Killeen, T. L. and Roble, R. G. (1984). An analysis of the high-latitude thermospheric wind pattern calculated by a thermospheric general circulation model: 1. Momentum forcing. *Journal of Geophysical Research: Space Physics*, 89(A9):7509–7522.

Kwak, Y. S. and Richmond, A. D. (2007). An analysis of the momentum forcing in the high-latitude lower thermosphere. *Journal of Geophysical Research: Space Physics*, 112(1):1–15.

Larsen, M. F. (2000a). A shear instability seeding mechanism for quasiperiodic radar echoes. *Journal of Geophysical Research*, 105:24931.

Larsen, M. F. (2000b). Coqui 2: Mesospheric and lower thermospheric wind observations over Puerto Rico. *Geophysical Research Letters*, 27(4):445–448.

Larsen, M. F. (2002). Winds and shears in the mesosphere and lower thermosphere: Results from four decades of chemical release wind measurements. *Journal of Geophysical Research: Space Physics*, 107(A8).

Larsen, M. F. (2004). Observations of overturning in the upper mesosphere and lower thermosphere. *Journal of Geophysical Research*, 109(D2):D02S04.

Larsen, M. F. (2013). Wind measurements: Trimethyl aluminum (TMA) chemical release technique. *An Introduction to Space Instrumentation*, pages 47–51.

Larsen, M. F., Christensen, A., and Odom, C. (1997). Observations of unstable atmospheric shear layers in the lower e region in the post-midnight auroral oval. *Geophysical research letters*, 24(15):1915–1918.

Larsen, M. F. and Fesen, C. G. (2009). Accuracy issues of the existing thermospheric wind models: can we rely on them in seeking solutions to wind-driven problems? *Annales Geophysicae*, 27(6):2277–2284.

Larsen, M. F., Fukao, S., Yamamoto, M., Tsunoda, R., Igarashi, K., and Ono, T. (1998). The SEEK Chemical Release Experiment: Observed neutral wind profile in a region of sporadic E. *Geophysical Research Letters*, 25(11):1789–1792.

Larsen, M. F., Liu, A. Z., Bishop, R. L., and Hecht, J. H. (2003). TOMEX: A comparison of lidar and sounding rocket chemical tracer wind measurements. *Geophysical Research Letters*, 30(7):3–6.

Larsen, M. F., Marshall, T. R., Mikkelsen, I. S., Emery, B. A., Christensen, A., Kayser, D., Hecht, J., Lyons, L., and Walterscheid, R. (1995). Atmospheric Response in Aurora experiment: Observations of E and F region neutral winds in a region of postmidnight diffuse aurora. *Journal of Geophysical Research*, 100(A9):17299.

Larsen, M. F. and Meriwether, J. W. (2012). Vertical winds in the thermosphere. *Journal of Geophysical Research: Space Physics*, 117(A9).

Larsen, M. F. and Mikkelsen, I. S. (1983). The dynamic response of the high-latitude thermosphere and geostrophic adjustment. *Journal of Geophysical Research: Space Physics*, 88(A4):3158–3168.

Larsen, M. F. and Walterscheid, R. L. (1995). Modified geostrophy in the thermosphere. *Journal of Geophysical Research*, 100(A9):17321.

Larsen, M. F., Yamamoto, M., Fukao, S., Tsunoda, R. T., and Saito, A. (2005). Observations of neutral winds, wind shears, and wave structure during a sporadic-E/QP event. *Annales Geophysicae*, 23(7):2369–2375.

Lehmacher, G., Guo, L., Kudeki, E., Reyes, P., Akgiray, A., and Chau, J. (2007). High-resolution observations of mesospheric layers with the Jicamarca VHF radar. *Advances in Space Research*, 40(6):734–743.

Lehmacher, G. A., Larsen, M. F., Collins, R. L., Barjatya, A., and Strelnikov, B. (2018). On the short-term variability of turbulence and temperature in the winter mesosphere. *Annales Geophysicae*, 36(4):1099–1116.

Lindzen, R. S. (1981). Turbulence and stress owing to gravity wave and tidal breakdown. *Journal of Geophysical Research*, 86(C10):9707.

Liu, A. Z., Roble, R. G., Hecht, J. H., Larsen, M. F., and Gardner, C. S. (2004). Unstable layers in the mesopause region observed with Na lidar during the Turbulent Oxygen Mixing Experiment (TOMEX) campaign. *Journal of Geophysical Research*, 109:1–17.

Liu, H. L. (2007). On the large wind shear and fast meridional transport above the mesopause. *Geophysical Research Letters*, 34(8).

Liu, H. L. (2017). Large wind shears and their implications for diffusion in regions with enhanced static stability: The mesopause and the tropopause. *Journal of Geophysical Research: Atmospheres*, 122(18):9579–9590.

Lühr, H., Rother, M., Häusler, K., Alken, P., and Maus, S. (2008). The influence of nonmigrating tides on the longitudinal variation of the equatorial electrojet. *Journal of Geophysical Research: Space Physics*, 113(A8).

Maeda, S., Fujiwara, H., and Nozawa, S. (1999). Momentum balance of dayside E region neutral winds during geomagnetically quiet summer days . *Journal of Geophysical Research: Space Physics*, 104(A9):19871–19879.

Makela, J. J., Harding, B. J., Meriwether, J. W., Mesquita, R., Sanders, S., Ridley, A. J., Castellez, M. W., Ciocca, M., Earle, G. D., Frissell, N. A., et al. (2014). Storm time response of the midlatitude thermosphere: Observations from a network of fabry-perot interferometers. *J. Geophys. Res. - Space*, 119(8):6758–6773.

Makela, J. J., Meriwether, J. W., Ridley, A. J., Ciocca, M., and Castellez, M. W. (2012). Large-Scale Measurements of Thermospheric Dynamics with a Multisite Fabry-Perot Interferometer Network: Overview of Plans and Results from Midlatitude Measurements. *International Journal of Geophysics*, 2012(3):1–10.

Martinis, C., Hickey, D., Oliver, W., Aponte, N., Brum, C., Akmaev, R., Wright, A., and Miller, C. (2013). The midnight temperature maximum from Arecibo incoherent scatter radar ion temperature measurements. *J. Atmos. Sol-Terr. Phy.*, 103:129–137.

Mayr, H., Harris, I., Spencer, N., Hedin, A., Wharton, L., Porter, H., Walker, J., and Carlson, H. (1979). Tides and the midnight temperature anomaly in the thermosphere. *Geophys. Res. Lett.*, 6(6):447–450.

Meriwether, J., Faivre, M., Fesen, C., Sherwood, P., and Veliz, O. (2008). New results on equatorial thermospheric winds and the midnight temperature maximum. *Ann. Geophys.*, 26(3):447–466.

Meriwether, J. W., Makela, J. J., Huang, Y., Fisher, D. J., Buriti, R. a., Medeiros, a. F., and Takahashi, H. (2011). Climatology of the nighttime equatorial thermospheric winds and temperatures over Brazil near solar minimum. *J. Geophys. Res.*, 116(A4):A04322.

Mesquita, R. (2015). *The Fabry-Perot Interferometer Manual.* Clemson University, https://doi.org/10.5281/zenodo.4536246.

Mesquita, R., Meriwether, J., Makela, J., Fisher, D., Harding, B., Sanders, S., Tesema, F., and Ridley, A. (2018). New results on the mid-latitude midnight temperature maximum. *Annales Geophysicae*, 36(2).

Mesquita, R. L. A., Larsen, M. F., Azeem, I., Stevens, M. H., Williams, B. P., Collins, R. L., and Li, J. (2020). In situ observations of neutral shear instability in the statically stable high-latitude mesosphere and lower thermosphere during quiet geomagnetic conditions. *Journal of Geophysical Research: Space Physics*, 125(8):e2020JA027972. e2020JA027972 10.1029/2020JA027972.

Mikkelsen, I. S., Jørgensen, T. S., Kelley, M. C., Larsen, M. F., and Pereira, E. (1981). Neutral winds and electric fields in the dusk auroral oval 2. theory and model. *Journal of Geophysical Research: Space Physics*, 86(A3):1525–1536.

Mikkelsen, I. S., Jørgensen, T. S., Kelley, M. C., Larsen, M. F., Pereira, E., and Vickrey, J. (1981). Neutral winds and electric fields in the dusk auroral oval 1. measurements. *Journal of Geophysical Research: Space Physics*, 86(A3):1513–1524.

Mikkelsen, I. S. and Larsen, M. F. (1983). An analytic solution for the response of the neutral atmosphere to the high-latitude convection pattern. *Journal of Geophysical Research*, 88(A10):8073.

Mikkelsen, I. S. and Larsen, M. F. (1991). A numerical modeling study of the interaction between the tides and the circulation forced by high-latitude plasma convection. *Journal of Geophysical Research: Space Physics*, 96(A2):1203–1213.

Mikkelsen, I. S. and Larsen, M. F. (1993). Comparisons of spectral thermospheric general circulation model simulations and E and F region chemical release wind observations. *Journal of Geophysical Research: Space Physics*, 98(A3):3693–3709.

Mondal, S., Sarkhel, S., Agarwal, J., Chakrabarty, D., Sekar, R., Yuan, T., Cai, X., Liu, A. Z., Nozawa, S., Saito, N., Kawahara, T. D., Mlynczak, M. G., and Russell III, J. M. (2019). On the long lasting "c-type" structures in the sodium lidargram: The lifetime of kelvin-helmholtz billows in the mesosphere and lower thermosphere region. *Journal of Geophysical Research: Space Physics*, 0(ja).

Nelson, G. and Cogger, L. (1971). Dynamical behaviour of the nighttime ionosphere at Arecibo. *J. Atmos Terr. Phys.*, 33(11):1711–1726.

Nozawa, S. and Brekke, A. (1995). Studies of the E region neutral wind in the disturbed auroral ionosphere. *Journal of Geophysical Research*, 100(A8):14717.

Nozawa, S. and Brekke, A. (1999a). Studies of the auroral E region neutral wind through a solar cycle: Quiet days . *Journal of Geophysical Research: Space Physics*, 104(A1):45–66.

Nozawa, S. and Brekke, A. (1999b). Seasonal variation of the auroral E-region neutral wind for different solar activities. *Journal of Atmospheric and Solar-Terrestrial Physics*, 61(8):585–605.

Nozawa, S., Brekke, A., Maeda, S., Aso, T., Hall, C. M., Ogawa, Y., Buchert, S. C., Röttger, J., Richmond, A. D., Roble, R., and Fujii, R. (2005). Mean winds, tides, and quasi-2 day wave in the polar lower thermosphere observed in European Incoherent Scatter (EISCAT) 8 day run data in November 2003. *Journal of Geophysical Research: Space Physics*, 110(A12):1–14.

Paschmann, G., Haaland, S., and Treumann, R. (2012). *Auroral plasma physics*, volume 15. Springer Science & Business Media.

Pfrommer, T., Hickson, P., and She, C. Y. (2009). A large-aperture sodium fluorescence lidar with very high resolution for mesopause dynamics and adaptive optics studies. *Geophysical Research Letters*, 36(15):2–6.

Picone, J. M., Hedin, A. E., Drob, D. P., and Aikin, A. C. (2002). NRLMSISE-00 empirical model of the atmosphere: Statistical comparisons and scientific issues. *Journal of Geophysical Research: Space Physics*, 107(A12):SIA—-15.

Pouquet, A., Rosenberg, D., and Marino, R. (2019). Linking dissipation, anisotropy, and intermittency in rotating stratified turbulence at the threshold of linear shear instabilities. *Physics of Fluids*, 31(10).

Rishbeth, H. and Garriott, O. K. (1969). *Introduction to ionospheric physics*, volume 14. Academic Press New York.

Rosenberg, N. W., Golomb, D., and Allen, E. F. (1963). Chemiluminescence of trimethyl aluminum released into the upper atmosphere. *Journal of Geophysical Research*, 68(20):5895–5898.

Ruan, H., Lei, J., Dou, X., Zhang, S.-R., Noto, J., and Kapali, S. (2013). Enhancements of nighttime neutral and ion temperatures in the f region over millstone hill. *Journal of Geophysical Research: Space Physics*, 118(4):1768–1776.

Sangalli, L., Knudsen, D. J., Larsen, M. F., Zhan, T., Pfaff, R. F., and Rowland, D. (2009). Rocket-based measurements of ion velocity, neutral wind, and electric field in the collisional transition region of the auroral ionosphere. *Journal of Geophysical Research: Space Physics*, 114(4):1–10.

Sastri, J. H., Ranganath Rao, H. N., Somayajulu, V. V., and Chandra, H. (1994). Thermospheric meridional neutral winds associated with equatorial midnight temperature maximum (mtm). *Geophys. Res. Lett.*, 21(9):825–828.

Scorer, R. S. (1997). *Dynamics of meteorology and climate*. John Wiley & Sons.

Scott, T. (2009). *Analysis of the Neutral Wind Profiles from the HEX II Experiment*. Master thesis, Clemson University.

Sobral, J., Carlson, H., Farley, D., and Swartz, W. (1978). Nighttime dynamics of the F region near Arecibo as mapped by airglow features. *J. Geophys. Res. - Space*, 83(A6):2561–2566.

Spencer, N., Carignan, G., Mayr, H., Niemann, H., Theis, R., and Wharton, L. (1979). The midnight temperature maximum in the Earth's equatorial thermosphere. *Geophys. Res. Lett.*, 6(6):444–446.

Tanskanen, E. I. (2009). A comprehensive high-throughput analysis of substorms observed by IMAGE magnetometer network: Years 1993-2003 examined. *Journal of Geophysical Research: Space Physics*, 114(5):1–11.

Thompson, M. (2005). Boltwood cloud sensor. *Cloudynights. com, Nov*, 25:6.

Tsuda, T. T., Nozawa, S., Oyama, S., Motoba, T., Ogawa, Y., Shinagawa, H., Nishitani, N., Hosokawa, K., Sato, N., Lester, M., and Fujii, R. (2009). Acceleration mechanism of high-speed neutral wind observed in the polar lower thermosphere. *Journal of Geophysical Research: Space Physics*, 114(4):1–10.

U.S. Standard Atmosphere (1976). *U.S. Standard Atmosphere*. National Oceanic and Atmospheric Administration, 1st edition.

Weimer, D. R. (1996). A flexible, IMF dependent model of high-latitude electric potentials having "space weather" applications. *Geophysical Research Letters*, 23(18):2549–2552.

Weimer, D. R. (2001). An improved model of ionospheric electric potentials including substorm perturbations and application to the geospace environment modeling november 24, 1996, event. *Journal of Geophysical Research: Space Physics*, 106(A1):407–416.

Weygand, J. M., Zesta, E., and Troshichev, O. (2014). Auroral electrojet indices in the northern and southern hemispheres: A statistical comparison. *Journal of Geophysical Research: Space Physics*, 119(6):4819–4840.

Wu, D. L., Yee, J.-H., Schlecht, E., Mehdi, I., Siles, J., and Drouin, B. J. (2016). THz limb sounder (TLS) for lower thermospheric wind, oxygen density, and temperature. *Journal of Geophysical Research: Space Physics*, 121(7):7301–7315.

Zhang, Y. and Paxton, L. J. (2008). An empirical Kp-dependent global auroral model based on TIMED/GUVI FUV data. *Journal of Atmospheric and Solar-Terrestrial Physics*, 70(8-9):1231–1242.

Zou, Y., Lyons, L., Conde, M., Varney, R., Angelopoulos, V., and Mende, S. (2021). Effects of Substorms on High-Latitude Upper Thermospheric Winds. *Journal of Geophysical Research: Space Physics*, 126(1):1–22.